

The Ice-water Interface and its Interactions with Colloidal Monolayers

Siyu Chen

St. Cross College
University of Oxford

Supervisors: Professor Dirk G. A. L. Aarts
and Professor Roel P. A. Dullens

A thesis submitted for the degree of
Doctor of Philosophy

Hilary Term 2019

Abstract

We investigate the interaction of colloidal particles with the ice-water interface using a combination of a directional solidification stage, a light microscope and thin sample cells. Firstly, we focus on separating the contributions of colloids from that of salt in inducing the Mullins-Sekerka instability of the ice-water interface. We show that while the instabilities more quickly develop at higher freezing velocities, the presence of the particles enhances the development of the perturbations. Consequently, we observe fully developed instabilities as 'ice-fingers' only when particles are present and at high freezing velocities. Secondly, we study the structures formed by the colloidal particles accumulating in front of the ice-water interface during the unidirectional freezing. By using different image analysis methods, we find that despite the slow freezing velocity, the increase of the particle concentration in front of the interface is still too quick for the formation of a crystal structure. However, once the particles have been entrapped by the ice, they form linear or zig-zag structures between the ice fingers. Thirdly, we look at the event of 'thermal regelation', specifically the movement of single particles in ice towards the ice-water interface. This is possible due to the presence of a premelted liquid film, surrounding the particle. Particle movement is measured by using tracking algorithms, and fitted to theoretical predictions, which capture a thermomolecular and a viscous force to describe the motion. From this we are able to determine that non-retarded van der Waals interactions dominate this premelting for our particle-ice system. In the last chapter, we study the 3D shape of the interface, and show how it is curved between the two walls. An earlier theory describing the typical curvature is shown not to work, and by varying material properties, we show that thermal conductivities of the different materials likely need to be accounted for. We finish the thesis with a conclusion and outlook.

Declaration

This thesis is submitted for the degree of Doctor of Philosophy in Physical and Theoretical Chemistry at the University of Oxford. No part of this thesis has been accepted or is currently being submitted for any degree, diploma, certificate or other qualification in this University or elsewhere. This thesis is wholly my own work, except where indicated.

Contents

Abstract **i**

Declaration **iii**

1 General Introduction **1**

1.1 Motivation 1

1.2 Colloids 3

1.3 Scope of the thesis 3

2 Theoretical Background and Experimental Methods **5**

2.1 Theoretical background 6

2.1.1 Ice nucleation 6

2.1.2 Premelting 7

2.1.3 Forces on a particle at the ice-water interface 13

2.2 Experimental Methods 14

2.2.1 Freezing set-up 15

2.2.2 Optical microscopy 16

2.2.3 Confocal microscopy 17

2.2.4 Colloidal model systems 19

2.2.5 Sample cells 20

2.2.6 Image analysis: particle detection 24

3 The Role of Particles in the Ice-Water Interface Instability 27

3.1 Introduction 28

3.2 Theory 29

3.2.1 The Mullins-Sekerka Instability 29

3.2.2 Supercooling 32

3.2.3 The effects of particles in supercooling 34

3.3 Experimental methods 35

3.4 Results 36

3.4.1 Influence of velocity on instability 36

3.4.2 Estimation of instability kinetics 38

3.4.3 The role of particles in interface instabilities 40

3.4.4 Instability wavelength and the freezing velocity 42

3.5 Conclusions and outlook 43

4 Pattern Formation in Freezing Colloidal Monolayers in Ice 45

4.1 Introduction 46

4.2 Theory 47

4.2.1 The Chernov approach to the critical velocity 47

4.2.2 Osmotic pressure 50

4.2.3 Impurity induced premelting 51

4.3 Experimental methods 51

4.3.1 Experimental set-up 51

4.3.2 Image analysis 52

4.4 Results 55

4.4.1 Solidification velocity 56

4.4.2 Radial distribution function 59

4.4.3 Voronoi areas and local density analysis 60

4.4.4 Bond-orientational order analysis 62
4.5 Conclusion and outlook 65

5 Thermal Regelation of a Single Particle 67

5.1 Introduction 68
5.2 Theory 69
5.2.1 Premelting 69
5.2.2 Thermal regelation of particles in ice 72
5.3 Experimental methods 74
5.3.1 Particle engulfment 74
5.3.2 Image analysis 76
5.4 Results and discussion 77
5.4.1 Qualitative observations of regelation 78
5.4.2 Motion of particles relative to the ice-water interface 79
5.4.3 Quantitative analysis of regelation 80
5.4.4 The premelted layer and the related physical parameters 82
5.5 Conclusions and outlook 84

6 The Ice-Water Interface in the Vicinity of a Wall 87

6.1 Introduction 88
6.2 Theory 89
6.2.1 Thermal capillary length 89
6.2.2 Shape of the interface 91
6.3 Experimental 92
6.3.1 Materials and equipments 92
6.3.2 Experimental methods 93
6.3.3 Reconstruction of the ice-water interface 94
6.4 Results and discussion 96

6.4.1 Fluorescent dye concentration 96
6.4.2 Higher salt concentration 98
6.4.3 Cell thickness 99
6.4.4 Temperature gradient 100
6.4.5 Organic solvent 100
6.4.6 Thermal conductivity 101
6.5 Conclusions and outlook 103

Summary **105**

List of publications **119**

Acknowledgments **121**

Chapter 1

General Introduction

1.1 Motivation

Ice is one of the most common substances in the world. The majority of the globe is covered by seawater, which transforms into ice under certain conditions. Pure systems consisting of only ice and water are rarely observed in nature, as such, investigating the interactions between the ice-water interface and microscopic particles can give insights into many everyday phenomena on varying length- and time-scales. For example, ice plays a critical role in the climate system, as it reduces heat exchange between the atmosphere and the earth's surface beneath the ice [1]. The reduction of the sea ice thickness, in turn, can be used as an indicator on the extent of anthropogenic global warming [2].

Another important role of surface ice includes providing information about the past history of the planet. This is made possible because gas bubbles [3], particles of mineral dust [4–7], organic molecules [8], species of micro-organisms [9] and other dissolved impurities [10] are trapped in layers of ice. As new layers of ice form above over time, the depth of the ice is related to a given time in the past. As a result, by drilling ice cores several kilometres deep, we can assess the preserved air bubbles and dust, which provides climate and geographical information of the corresponding period. Scientists have reconstructed the climate record from $\sim$ 130,000 years ago by analysing a 2,540-m-long ice core drilled in Greenland [11].

This interaction between the ice and the particles also give rise to interesting daily phenomenon including the formation of potholes [12,13]. Potholes are formed via the process called 'frostheave',

caused by the suction of water along a temperature gradient, from warm to cold [13,14] reference added. In countries with very cold winter weather, a layer of ice will form on top of the road surface. This surface layer serves as the coldest region, and underneath is the warmer region of liquid water present in soil. Therefore we have a net flow of water from below, and this cryosuction results in mechanical stress, which damages soils, rocks and roads [12].

Material scientists and biologists are also interested in studying how ice crystals grow and interact with foreign materials. In industry, material scientists use a process called 'freeze casting', where controlled unidirectional freezing of slurry is applied to produce porous materials including ceramics [15]. By tuning the processing and physical parameters, such as the freezing velocity, solvent and powder particle size, we can achieve products with different roughness, structures and morphologies [16].

For biologists, controlling ice growth is very important as it relates to the survival rate of samples in cryopreservation [17], the process of preserving the biological structure and/or function of living systems by freezing to and storage at ultralow temperatures. It is the only current technology that maintains ex-vivo biological function and provides long-term product storage [18]. During this process, there are multiple ways of causing injury to the sample ('cryoinjuries'), including the formation of needle-shaped ice crystals and the subsequent penetration of cell membranes, which damages the sample mechanically [19]. In recent years, new cryoprotectant mixtures and treatment procedures have been developed to create a more controlled ice growth to minimise the damage caused to samples [20].

In this thesis we will briefly introduce nucleation and growth of ice, but focus specifically on the ice-water interface and its interaction with particles. We will study the behaviour using colloidal particles suspended in water and ice, held at a temperature close to the melting point, as a model system for real life systems. Firstly, we are interested in how an advancing ice front is affected by its growing conditions, namely the freezing velocity and the presence of salts and particles. We are also interested the structures formed by the particles in front of and inside the ice during this unidirectional freezing. Secondly, we are interested in how trapped particles behave after ice growth; for example, the migration of particles in ice with a temperature gradient [21], a process known as 'thermal regelation'. Finally, we are also interested in the shapes formed by the ice-water interface under different experimental settings in an unidirectional freezing set-up, both theoretically and experimentally. This allows us to better understand the interactions between a single layer of particles and an advancing interface.

1.2 Colloids

Colloidal particles provide an ideal model system to study natural microscopic objects, in a well defined, controlled manner. The term colloid describes systems that are composed of objects on the length scale of a few nanometres to a few micrometres, dispersed in a continuous phase [22]. They experience Brownian motion, which causes particles to carry out a 'random walk' as they diffuse [23]. This allows the particles to explore phase space, much like an atomic or molecular system, making them a powerful model for such systems [24], but at experimentally convenient timescales (*seconds*) and lengthscales (μm) instead [25].

The size of the colloidal particles makes them conveniently resolvable in real time using optical microscopy [26]. Furthermore the resolution ensures we can observe and track individual particles and their behaviour as they are approached by the ice-water interface and when they are engulfed by the ice [27]. In this thesis, particles are synthesised in the laboratory, to be used as a model system for microscopic particles that exist in nature, interacting with the ice. The size of the particles we use in this thesis is more comparable to natural systems than many previous experiments, in which particles of much larger sizes were used [28–30].

The interactions between colloidal particles can be finely tuned by changing their surface chemistry [31–33], changing the materials they are made of [34–37], or by varying the solvent they are dispersed in [38]. Colloidal particles can also be designed and synthesised in many different shapes, ranging from rods [39] to polyhedra [40]. This is beyond the scope of this thesis, but experiments with these particles are interesting as they may provide exceptional insights on natural systems, since very few particles are spherical in nature.

1.3 Scope of the thesis

In Chapter 2 we present the theoretical background and experimental methods used in this work. We start with discussing how ice is formed and how it grows. Premelting is then discussed in detail with regards to different possible origins. We also present the different approaches re-

searchers have taken to analyse the forces existing on a particle in the system. Regarding the experimental set-up, we first describe the cooling stage and the microscopes used to achieve and observe the freezing process in a controlled way. Then we describe the colloidal particle system used in our experiments and the preparation of the sample cell, capable of confining the particles in 2D for better observation. We finish this chapter with the particle detection algorithms used throughout the thesis.

In Chapter 3 we focus on the instability of the ice-water system. Firstly, the Mullins-Sekerka instability is introduced and discussed in detail. We also elaborate on the causes and effects of supercooling before we describe the experimental results. Here we examine the experimentally observed dependence of the perturbation and instability wavelength on the freezing velocity. We also introduce the particle into the same salt system and see how the presence of the particle affects the growth of instabilities.

In Chapter 4 we continue examining the interface instability with the presence of particles, but focusing on the rearrangement and pattern formed by the particles in front of the interface. We first discuss the theories behind the particle rearrangements. Specifically, the forces involved in the situation are discussed in more detail. Then we present the experimental data of the freezing of the colloidal solution at different freezing speed. This is followed by various analyses, regarding the structure of the particle clusters formed during the process.

In Chapter 5, we fall back to the simplest model system where a single particle interacts with ice close to the melting temperature. We start with describing 'thermal regelation', the movement of particles towards a static ice-water interface, and then present our experimental observations. Analysis is then conducted to calculate the particle velocities and the premelted layer thickness between the particle in the ice for different particle diameters.

In Chapter 6, we study the ice-water interface in 3D using confocal laser scanning microscopy. Fluorescent dye is used, which is insoluble in the ice phase and allows for distinction between the water (dye rich region) and ice (dye poor region) phases. These confocal images are then analysed to extract the geometric information of the interface in 3D. We also theorise an explanation for the 3D shape using an analogue to a gas-liquid interface under gravity, which will guide the direction of future theoretical development.

Finally, we conclude the thesis with a summary of our findings from each of the chapters. We also suggest several ideas for future work.

Chapter 2

Theoretical Background and Experimental Methods

ABSTRACT

In this thesis, the dynamics of ice and colloidal particles is investigated. In this chapter we first introduce the basic concepts and experimental methods common to all subsequent chapters. It starts with the basics about ice nucleation and growth, then introduces the important terms including premelting and the description of the forces that act on a particle in the freezing system. Finally, the experimental set-up used is presented in detail. This includes the freezing stage, the microscopes, the colloidal model systems and the sample cells.

2.1 Theoretical background

In this chapter, the underlying theories behind the physical behaviour involved in freezing colloidal suspensions are explained. We start in Section 2.1.1 by describing the nucleation of ice and the phenomenon of supercooling. Then in Section 2.1.2 we introduce the term 'premelting', an important concept describing that water persists in the liquid phase at lower temperatures than expected from the normal phase diagram. Finally in Section 2.1.3, we present a brief history of the development of the models around the forces on a particle close to the ice-water interface.

2.1.1 Ice nucleation

The formation of an interface is associated with an energy cost. Therefore, when pure water is cooled just below the bulk melting temperature T_m, the nucleation and growth of ice does not occur spontaneously, instead, the water is first supercooled into a metastable liquid [41]. This supercooling can occur at as low as $-42\,^{\circ}\mathrm{C}$ for small, pure water droplets.
One way of ice formation is called homogeneous nucleation [42]. This occurs when the water becomes sufficiently supercooled below the bulk melting temperature that a sufficient number of relatively long-lived hydrogen bonds develop spontaneously at the same location, so that an initial nucleus is formed. The critical cluster size can be calculated from classical nucleation theory, which balances the free energy loss from forming a new ice-water interface and the free energy gain upon bulk phase change below T_m. The resulting expression for the critical radius, r_c, is given by

$$r_c = \frac{2\gamma_{iw} T_m}{\rho_i L_m \Delta T}, \tag{2.1}$$

where γ_{iw} is the surface free energy of the ice-water interface, ρ_i is the density of the ice, L_m is the latent heat of melting per unit mass and ΔT is the undercooling for a system at temperature T, $\Delta T = T_m - T$. The r_c only need to be a few molecular radii for the nucleation to be highly likely [43]. The barrier to spontaneous nucleation is overcome when a cluster of radius $r > r_c$ forms, and this will be followed by a spontaneous phase change of the surrounding water and the growth of the ice crystal. Equation 2.1 also predicts that as the undercooling ΔT increases,

the critical cluster size decreases and ice nucleation becomes more probable.
Ice can also be formed via heterogeneous nucleation. In fact, in nature or in bulk samples, ice is also almost always formed heterogeneously. Heterogeneous nucleation occurs when an external surface is present in the system (the wall of the container or the presence of microscopic particles such as dust), that the arrangement of water molecules into the ice structure can be aided [42]. This aided rearrangement significantly lowers the free energy barrier to nucleation, therefore the ice nucleation will occur at smaller undercooling relative to homogeneous nucleation.
Given either mechanism of ice nucleation, the water needs to be in the metastable supercooled phase first. There exists the condition where, beside the interface, the temperature for the ice is below the local liquidus temperature. Consequently, this initial ice growth is rapid and unstable. This is called constitutional supercooling. Shibkov *et al.* measured solidification rates up to $100\,\mathrm{mm\,s^{-1}}$ for nucleation temperatures around $T = -16\,^{\circ}\mathrm{C}$ [44]. When growing at such high rates, the ice interface loses its planarity and becomes morphologically unstable. The surface breaks down into cellular (columnar) structures (at low freezing velocity) and dendritic (branched) structures (at high freezing velocity). There are three major factors contributing to this morphological instability when the liquid is constitutionally supercooled [45], which will be discussed in more detail in Chapter 3.

2.1.2 Premelting

The phrase 'premelting' describes the presence of a thermodynamically stable thin layer of liquid film on the surface of a solid substrate engulfed by ice, at temperatures close to, but below the bulk melting temperature [46]. This phenomenon has been supported by experimental evidence [47–49] and has been shown to be related to a diverse range of phenomena, such as the formation of snowflakes, electrification of thunderclouds [50] and the mobility of particles in solid materials.
We schematically represent the three forms of premelting in Figure 2.1:

(i) The Gibbs-Thomson effect, or curvature induced premelting. This occurs when the ice is confined in a pore space, such as between closely packed colloids. The driving force for melting is a reduction of interfacial energy between the particles and the matrix due to the presence of the curvature.

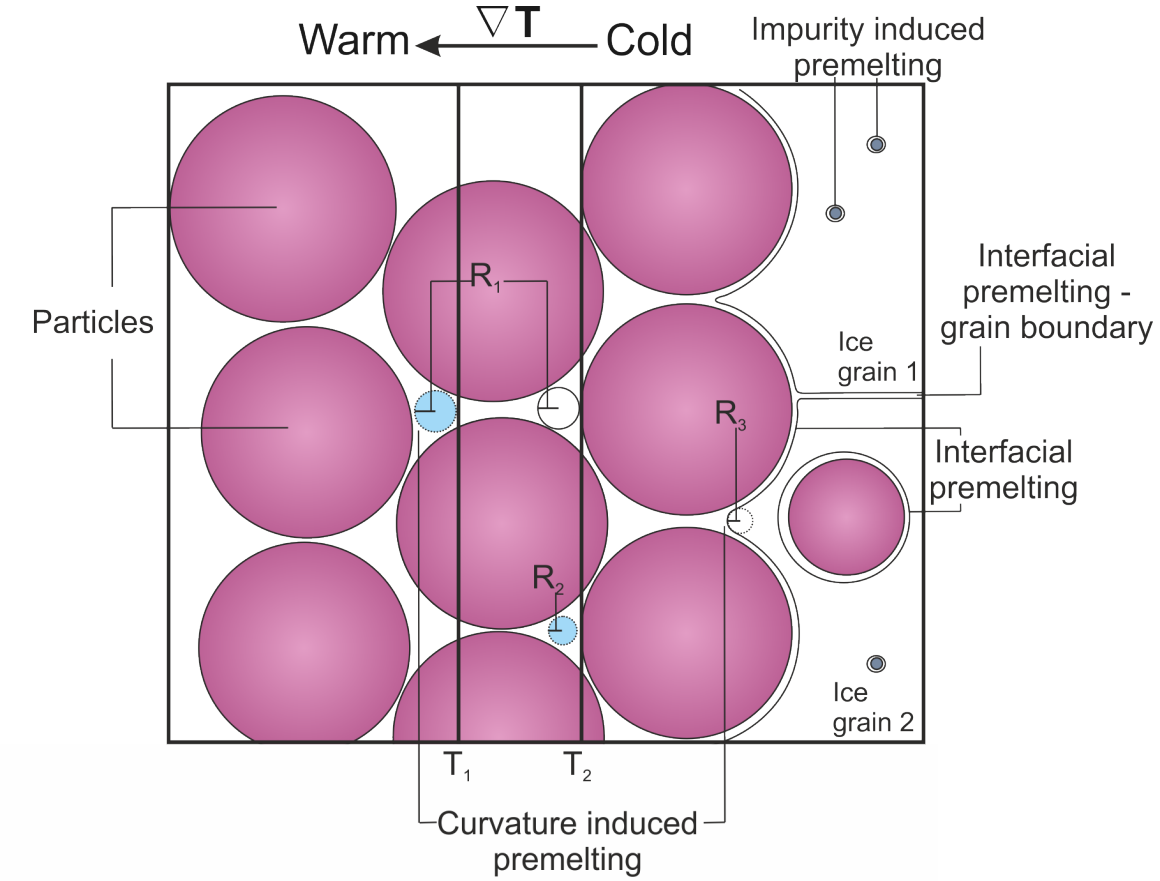


Figure 2.1: Schematic diagram showing the different forms of premelting when a temperature gradient, ΔT, is applied to a sample of colloidal suspension (not-to-scale). Pores that are filled with ice are depicted not coloured in and those filled with water are depicted as blue circles. The Gibbs-Thomson effect is shown as at T_2, where pores of radius R_1 contains ice but pores of radius $R_2 \leq R_1$ are filled with water. Interfacial premelting is shown for the surface of colloidal particle and a different ice grain. Impurity induced premelting is shown for small gaseous impurities trapped in ice. In reality, impurities also includes salt ions, which cannot be seen.

(ii) Interfacial premelting, which occurs due to the repulsive intermolecular interactions between the ice and the surface of a third phase. For example, between ice and a colloidal particle, a glass wall, or a different ice crystal orientation.

(iii) Impurity induced premelting. The presence of a component in our system that is not water, ice or the colloidal particles is defined as an impurity. Impurities such as dissolved ionic or gases are trapped in the ice. These impurities cause freezing point depression. This greatly enhance the premelting according to their concentration.

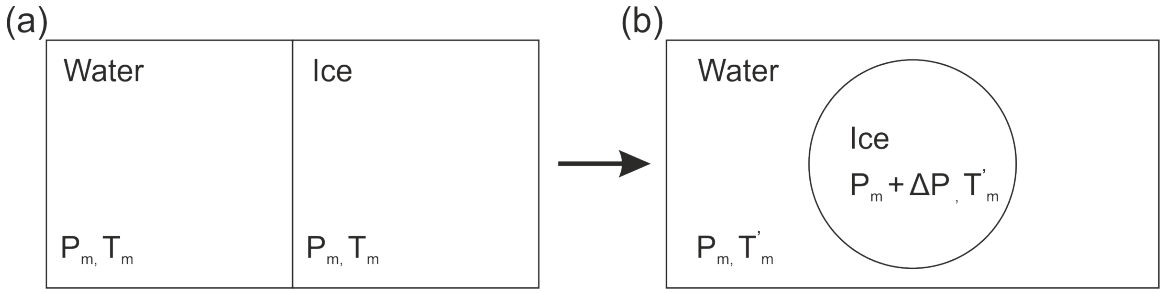


Figure 2.2: Schematic diagram showing (a) the reference state and (b) the equilibrium system with a curved ice surface.

Curvature induced premelting: the Gibbs-Thomson effect

We follow the treatment by Schollick to derive the Gibbs-Thomson equation [51]. First, we consider a reference system with a flat interface (Figure 2.2 (a)), where ice at chemical potential μ_i, is in equilibrium with water at chemical potential μ_w. Both phases are at the melting temperature and pressure, T_m and P_m, giving

$$\mu_i(P_m, T_m) = \mu_w(P_m, T_m) \tag{2.2}$$

Now consider a new equilibrium system where the ice-water interface is curved, shown in Figure 2.2 (b). The pressure inside the ice is increased by ΔP due to the Laplace pressure, which can be calculated from the ice-water interfacial free energy, γ_{iw}, and the curvature, κ, by the equation

$$\Delta P = \gamma_{iw}\kappa. \tag{2.3}$$

Assuming the pressure of the water remains at P_m, the new equilibrium condition becomes

$$\mu_i(P_m + \Delta P, T'_m) = \mu_w(P_m, T'_m), \tag{2.4}$$

where $T'_m < T_m$ is the new temperature of the system. This expression is related to the reference point (Equation 2.2.) by

$$\mu_i(P_m + \Delta P, T'_m) = \mu_i(P_m, T_m) + \int_{T_m}^{T'_m} \left(\frac{\partial \mu_i}{\partial T}\right)_P dT + \int_{P_m}^{P_m+\Delta P} \left(\frac{\partial \mu_i}{\partial P}\right)_T dP \tag{2.5}$$

and

$$\mu_w(P_m, T'_m) = \mu_w(P_m, T_m) + \int_{T_m}^{T'_m} \left(\frac{\partial \mu_w}{\partial T}\right)_P dT. \tag{2.6}$$

We then apply the Gibbs-Duhem equation, $Nd\mu = -SdT + VdP$ to Equations 2.5 and Equations 2.6, assuming that the molar entropy $S_m = S/N$ and molar volume $V_m = V/N$ are constant over the integral range. This gives

$$-S^i_m(T'_m - T_m) + V^i_m(P_m + \Delta P - P_m) = -S^w_m(T'_m - T_m). \tag{2.7}$$

Using $\Delta S = S^w_m - S^i_m$ and the latent heat of solidification per unit mass of water, $L_m = T_m \Delta S/M$, where M is the molar mass, we obtain the equation for undercooling due to the Gibbs-Thomson effect,

$$\Delta T_{GT} = T_m - T'_m = \frac{T_m}{L_m M} V^i_m \Delta P. \tag{2.8}$$

Using ΔP from Equation 2.3 and the density of ice, $\rho_i = M/V^i_m$, we have the Gibbs-Thomson equation:

$$\Delta T_{GT} = \frac{T_m}{L_m \rho_i} \gamma_{iw} \kappa. \tag{2.9}$$

This equation predicts the allowed degree of undercooling for ice in a pore of radius R (curvature $\kappa = 2/R$). This means for a porous material (such as a colloidal suspension) with pores of radius R, the water in the pores can remain supercooled below T_m, down to the temperature T'_m. Any further cooling will cause ice to nucleate into the pores.

Interfacial premelting

Interfacial premelting occurs due to repulsive intermolecular interactions between the ice and a third phase. This third surface can be water vapour, causing surface premelting, or another grain of ice with a different orientation, causing grain boundary premelting [52]. It is of key interest when the foreign phase is the surface of another solid, such as glass, metals, graphite, polystyrene, and silica [50]. Here in our system the third phase is either the walls of the sample cell or the colloidal particles.

The expression for interfacial undercooling can be found by using a similar derivation as Equation 2.9. We again start by considering a reference point where ice is equilibrium with water. When a foreign phase is introduced into the system, instead of considering the Laplace pressure, a disjoining pressure P_T, that shifts the equilibrium condition by the field energy per molecule due to the intermolecular forces present, was considered. The new equilibrium condition for a system containing a foreign phase is thus [53]:

$$\mu_f(T, P_m, d) = \mu_w(T, P_m) + U'(d) = \mu_i(T, P_m), \tag{2.10}$$

where μ_f, μ_w, μ_i is the chemical potential of the premelted film, water and ice. $U'(d)$ is the derivative of the underlying effective interfacial free energy per molecule with respect to the film thickness, d. The disjoining presure depends on the type of intermolecular forces and the film thickness [54]. Here we will just present the results and the detailed calculation will be given in Chapter 5. We have the expression for the premelted layer thickness:

$$d = \lambda \left(\frac{T_m - T}{T_m} \right)^{-\frac{1}{3}}, \tag{2.11}$$

and the deviation of premelted film from T_m, ΔT_{Int} is given by:

$$T_m - T = \Delta T_{Int} = \frac{T_m}{L_m \rho_i} P_T(d). \tag{2.12}$$

This shows that the competition between freezing and the repulsive forces determines the thickness of the premelted layer of water that exists below T_m [55]. The film thickness decreases with T as represented schematically in Figure 2.3, where $d_3 > d_2 > d_1$.

During directional solidification, particles can be 'rejected' from the advancing ice front, leaving a build-up of particles near the interface; or they can be 'engulfed' or 'entrapped', where they end up trapped within the ice or between ice grains. The premelted layer acts as a lubricant during the engulfment or entrapment events. This has significant impact when considering the particle distribution and behaviour within the ice.

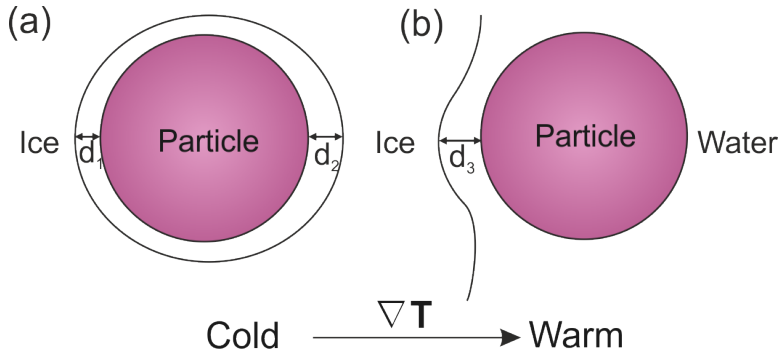


Figure 2.3: A schematic diagram representing interfacial premelting due to (a) a particle trapped in ice with a premelted film around it and (b) a particle separated from the ice front by a premelted film; $d_3 > d_2 > d_1$ (not to scale).

Impurity induced premelting

An example of the impurities present in our system is the salt left from the synthesis of the colloidal sample. It causes a colligative effect that lowers the equilibrium melting temperature known as 'freezing point depression'. A colligative effect is a bulk phenomenon in dilute solution and depends only on the number of solute particles present, not their identity [56].

Here the effect is shown schematically for a simple 2-component mixture, or binary melt, in the case of salt and water (Figure 2.4) [55]. The equilibrium state of a given mixture of salt and water at temperature T and composition C (the concentration of NaCl salt), at constant pressure is represented on this diagram by the point (T_E, C_E). The phase diagram is divided into regions of different phase. There are two solid phases and a liquid phase (that is the solution of the two end members). Note that it is a simple model as other materials have more complicated solid phases and necessarily more complicated phase diagrams. The curved line in Figure 2.4 is the liquidus line, representing the temperature at which a binary melt of a given composition C can exist in equilibrium in both the liquid and solid phase. For 0% salt concentration, the liquidus temperature is simply the melting point of ice (0 °C), while for 100% salt it is 801 °C. When we contaminate pure water at 0 °C with a small amount of salt, the equilibrium freezing temperature is lowered. Equivalently, one could start with pure molten salt at 801 °C and contaminate it with a small amount of water to lower the melting point. The point where the two liquidus curves meet (T_E, C_E) is also called the eutectic: this is the minimum temperature at which solid and liquid salt water can coexist in thermodynamic equilibrium.

For an ideal case with no interfacial forces, the freezing point depression can be predicted by

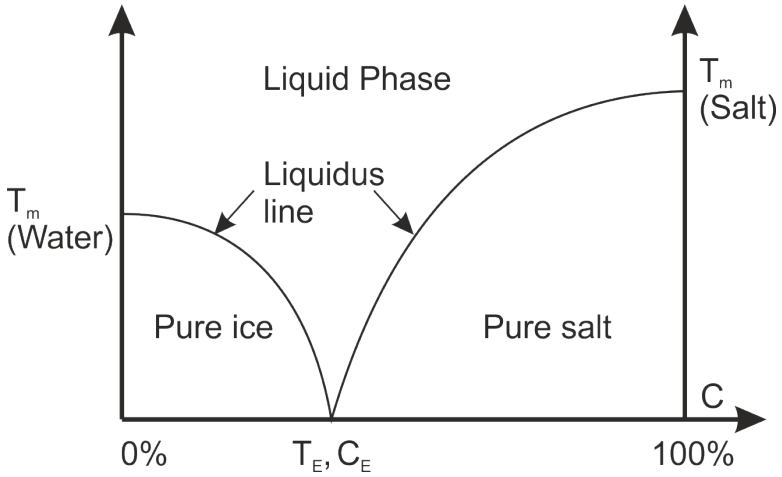


Figure 2.4: Equilibrium phase diagram for a solution of salt and water.

the equation [56]

$$\Delta T = \frac{RT_m^2 c}{L_m \rho_i}, \tag{2.13}$$

where c is the molar concentration of the impurity and R is the gas constant.

The effect of impurities on premelting is complex when colloidal particles are present. Firstly, the particles are impurity by definition, so naturally their concentration will affect the level of impurity induced premelting. Secondly, the particles introduce curvatures to the system. The higher the concentration, the more likely there will be small pores formed among the particles, giving birth to the curvature induced premelting. We also need to consider the interaction between the surface of the particles and ice, which will cause the interfacial premelting. The solubility of impurities in ice is measured by the segregation coefficient, k, which is the ratio of impurity concentrations in ice and water. The ice contribution to k is close to 0 if we establish the freezing carefully, which allows us to treat the impurities in the system as being homogenously distributed in the premelted layer [57, 58].

2.1.3 Forces on a particle at the ice-water interface

Since the 1960s numerous studies have focused on the forces acting on particles near a solid-liquid interface using the model system where a single smooth spherical particle lies ahead of a planar solidification front. In these models, the primary force that promotes particle engulfment

is a viscous drag force, F_η, that exists in the premelted layer that separates the particle from the phase boundary [59]. At larger film thickness, the viscous component around the bulk of the particle is more important, while if the film thickness is small, the drag is dominated by the lubrication force that accompanies fluid flow within the thin film [60].

On the contrary, for the force responsible for the pushing of the particles ahead of the interface, there are two major approaches. One approach is the 'macroscopic approach', first developed by Uhlmann *et al.* [61] where they have proposed that the interfacial energy is the main force. This has later been improved by Bolling and Cisse [62] to include effect of the interface shape, and by Omenyi and Neumann [63] to include thermodynamic arguments. Stefanescu and Shangguan *et al.* [64] have further refined the interface shape by incorporating the thermal conductivity difference between the particle and the melt.

The other approach is the 'microscopic approach', first by Chernov *et al.* [65, 66], where they introduced the idea of a positive disjoining pressure in the liquid film caused by the change in the chemical potential of the thin liquid film in the particle-interface gap, separating the particle from the solidification interface which results in a repulsive interfacial force. The presence of a positive disjoining pressure leads to particle repulsion while a negative pressure would lead to entrapment. This intermolecular interaction can be treated as a van der Waals force between two spheres, as shown by Potschke and Rogge [67].

Sen *et al.* [68] have compared the critical velocities calculated using the two approaches to the experimentally measured critical velocities for a biphenyl/glass system, where they concluded that the microscopic approach agreed reasonably well with the experimental results while the macroscopic approach underestimated the critical velocity. Therefore within this thesis, we will follow the microscopic Chernov approach. The detailed mathematical formulation will be shown in the relevant chapters.

2.2 Experimental Methods

To achieve controlled freezing we use a set-up consisting of a directional freezing apparatus that allows the temperatures and the solidification rates to be adjusted individually with precision. Both bright-field and confocal laser scanning microscopy were used to observe the interaction between the ice-water interface and colloidal particles as well as the interface structure itself.

2.2.1 Freezing set-up

We have employed a Linkam GS350 stage, in which a fixed temperature gradient can be established and the sample can be translated at prescribed rates using the Linksys32 software. This is a similar system as has been used previously in our group [51]. A photograph and schematic diagram of the set-up used is shown in Figure 2.5. In contrast to freezing from a cold boundary held at a fixed temperature (fixed chill), we use directional solidification which allows independent control of the freezing rate and temperature gradient. This configuration also has the advantages of similarity to industrial solidification techniques [69]. The stage provides a temperature range of -196 ℃ (limited by the boiling temperature of nitrogen) to 350 ℃, with an accuracy of 0.1 ℃. Cooling was achieved by the use of a pump, which sucked liquid nitrogen from a dewar, through the plates, where it condensed and evaporated and nitrogen gas was released to the surroundings. Also, the air inside the box could be replaced by nitrogen via the purge tubing in order to remove water vapour, which could condense on the sample. Heating was achieved by the use of electrical resistance heaters embedded within the plates. The motor is a stepper motor that could move at rates between $1\,\mu m\,s^{-1}$, and $2000\,\mu m\,s^{-1}$ with a minimum step of $1\,\mu m$, which was controlled by the same software.

In a typical experiment, the sample is placed on top of the Peltier plates, thermal insulation is achieved by covering the sample with the metal lid. An observation window was made in the middle to let the light path come through. The desired temperature gradient ∇T is established by setting the temperatures of Peltier elements and the sample is then put in motion by the motor. The theoretical temperature gradient across the gap can be calculated by $\nabla T_{Theory} = (T_H - T_C)/x_{gap}$, where T_C and T_H are the set temperatures of the cold and hot plates, and x_{gap} is the distance between the two plates, which is 2 mm here.

When performing an experiment, the cold plate was cooled until ice nucleated, while the hot plate was left at room temperature, thus the precise ice nucleation temperature was not generally noted. After nucleation of the ice was confirmed, the desired temperature gradient was set and the sample was left to stabilise. A fixed rate of cooling was maintained by controlling the motor to move the sample into the cold plate at a constant speed.

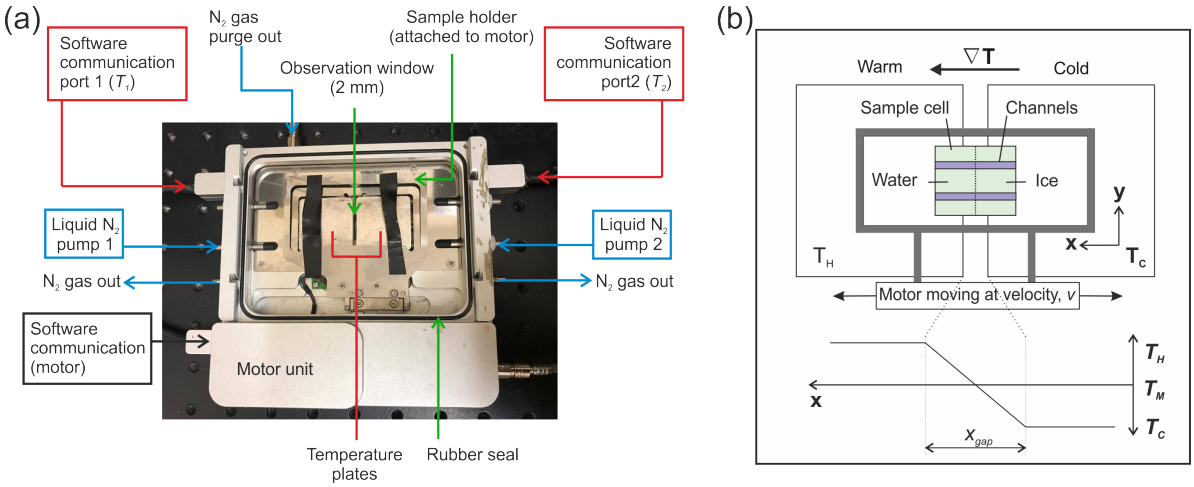


Figure 2.5: (a) A labelled photograph of the Linkam GS350 freezing stage. The nitrogen input/outputs and the pumps are shown schematically. Three software communication wires connect to the computer are present for the independent control of temperature and motor; (b) A schematic picture of the plates and motor, which is attached to a sample cell by two strips (thick black lines). These represent the tape which holds the sample cell firmly against the plates. The sample cell contains both ice and water, as the temperature of the plates which they are in contact with are controlled separately, one above (T_H) and the other one below (T_C) the melting point of water, T_m. The theoretical temperature profile is shown below, with temperature vs x, where the dotted lines connect the plate edges to their equivalent positions along x.

2.2.2 Optical microscopy

An upright bright-field microscope was constructed from component parts, purchased mainly from Thorlabs. The components were contained within a cage system and external light was blocked by using black tubes. The diagram in Figure 2.6 shows the schematic of the microscope, and Table 2.1 lists the parts. The sample is illuminated with a LED light source, magnified with a 20× or 50× Olympus Long Working Distance M-Plan Fluorite objective according to the experiment, and the gray-scale images are recorded using a Ximea MQ013MG-E2 CMOS camera at desired capturing rate. We chose the long working distance objectives because in our set-up the imaging objective must have a working distance of at least 4.6 mm, which is the distance from the sample (Peltier plates) to the top of the Linkam GS350 stage (lid). The microscope stage can be manually translated in x, y, z directions to achieve a good field of view and sharp focusing using travel stage components.

Name	Type	Details
LEDs	Cold white LED	Viewing angle of 140°
L1	Plano convex lens	Frosted for blurring the matrix of LEDs at the source
L2	Achromatic lens	Small focal length to reduce the depth of field
L3	Achromatic lens	
L4	Tube lens	Imaging sample onto camera
P1	Pinhole	Controls the field of view
P2	Pinhole	Controls the depth of field
Motion in x, y	Manual Linear Translation Stages x 2	Placed on top of, and perpendicular to, each other for motion in 2D
z motion	Edmund Optics vertical translation stage	Controls the depth of field
Homebuilt mount		Mount the freezing set-up onto the translation stage

Table 2.1: Building components for the microscope set-up and the sample stage. All components are purchased from Thorlabs unless otherwise stated.

2.2.3 Confocal microscopy

Confocal Laser Scanning Microscopy (CLSM) is another type of optical microscopy, which typically uses laser light sources with wavelengths in the visible light region. Confocal microscopy uses two pinholes, one at the light source and one at the receiving detector, to suppress the out-of-focus light in dense samples thus improving the signal-to-noise ratio of the images. The scattered light from out of focus planes is further suppressed by illuminating the sample sequentially (point-by-point) with the excitation wavelength for the fluorescent labelled sample, so that only the fluorescent signal from the illuminated point is collected. Altogether, these make precise 3D imaging possible.

The confocal images were taken using a custom Thorlab confocal set-up. A Thorlabs confocal scan head was coupled with an Olympus IX73 microscope, with the Olympus Long Working Distance M-Plan Fluorite 50× objective. A schematic diagram of a typical confocal laser scanning microscope is shown in Figure 2.7. The first pinhole is placed immediately after the excitation laser source, and the other is placed before the Photo-Multiplier Tube (PMT) detector. The excitation light travels in from the laser source, narrowed by the first pinhole, then passes through the dichroic mirror. The collimated light is then directed onto the specified point of the sample by the two scanning mirrors. In our set-up, the confocal scans in the x-direction is controlled by a resonance mirror, operating at around 8 kHz. The scan in the y-direction is controlled by a galvanometer mirror, which operates at a lower frequency. The excited fluorophores emit

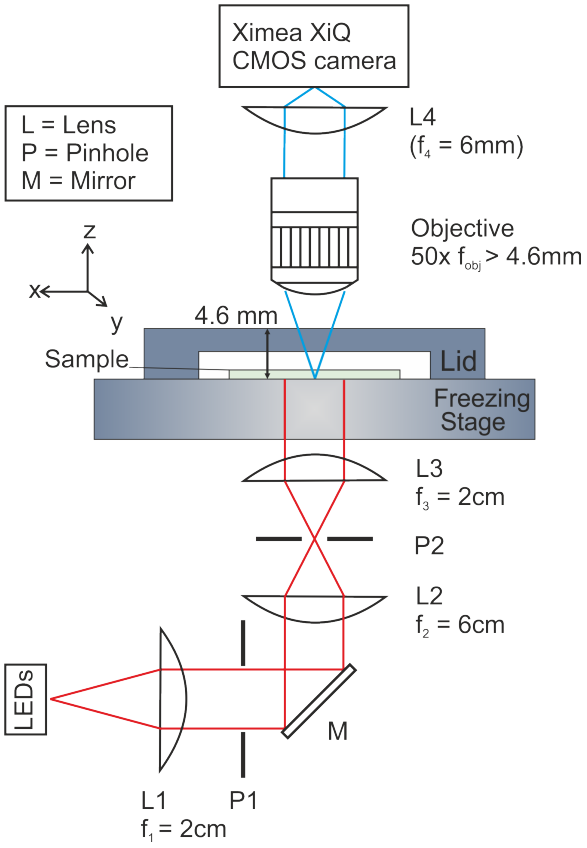


Figure 2.6: Diagram of the microscope set-up. Köhler lens set-up (L1 - 3) was placed below the sample to provide a source of uniform illumination (red). An image of the sample is transmitted through the imaging objective, magnified and focused on to the camera by L4. The sample can be moved into focus by moving the stage in z, and different areas of the sample can be viewed by moving the stage in the x and y directions.

light and came back via the same path. The dichroic mirror is chosen according to $\lambda_{emission}$ and $\lambda_{excitation}$ so that the emitted light is reflected by the dichroic mirror instead. A multi-channel fibre coupled laser source was used to provide excitation wavelengths at 488 nm and 532 nm. The dichroic cube with 495 nm longpass dichroic filter or 538 nm longpass dichroic filter was used accordingly. The emitted light then passes through the second pinhole and reaches the PMT. The PMT collects the signal point-by-point, which is used for computer reconstruction of the entire image. Multiple PMTs can also be attached for multi-channel detection. Here in our set-up, the dichroic cube is placed so that there is a channel dedicated for the backscattering channel, which is useful when it comes to detecting the position of the glass boundaries. Because the refractive index of glass and water is different, this change in the refractive index caused the scattering of the applied laser light, which can be recorded as long as this scattered light does not go through the filter.

Typically the resolution for a confocal microscopy is $\sim$ 200 nm in (x, y), and $\sim$ 500 nm in z due

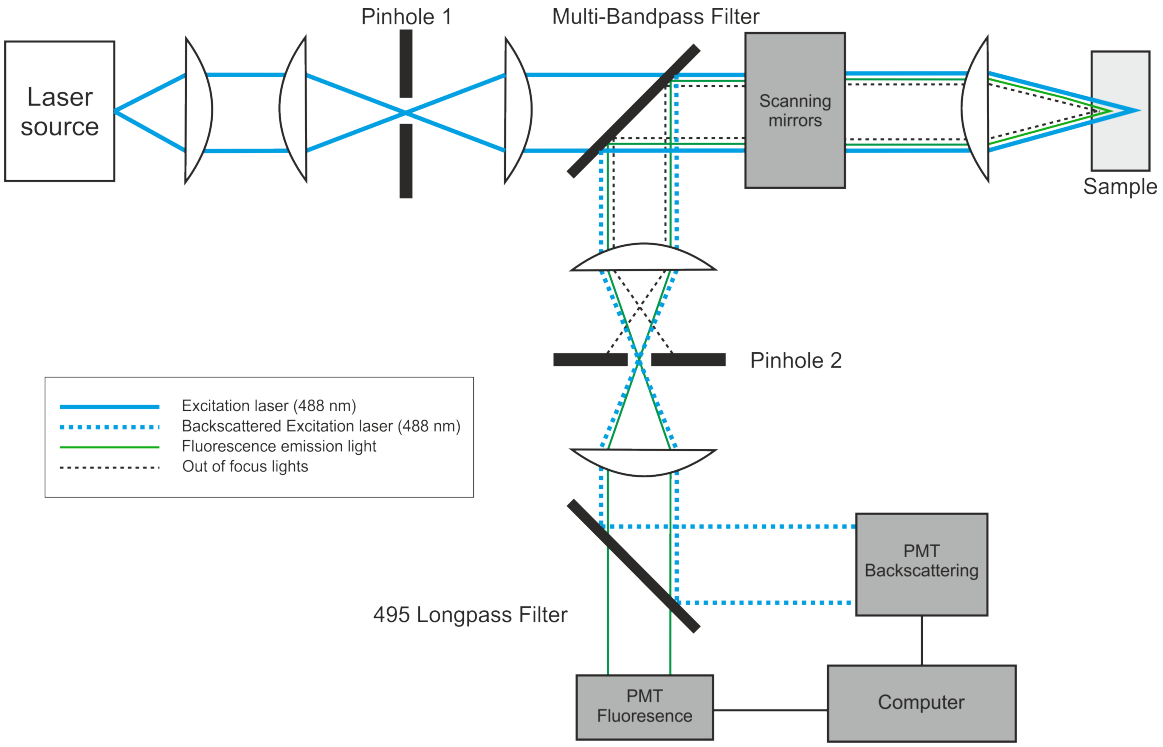


Figure 2.7: Schematic of a typical laser scanning confocal microscope.

to the point spread function [31]. The speed of obtaining a 3D z-stack depends on the exact set-up of the microscope. In our set-up, a Thorlab Stepper was used. This provides a set of 2D confocal images which can then be reconstructed for a full 3D volume image of the sample. All images were taken using the ThorImages^{TM} software.

2.2.4 Colloidal model systems

In this thesis, we focus on a quasi-2D colloidal system, consisting of a monolayer of particles confined within our sample cells. The colloidal particles are 3-(trimethoxysilyl)propyl methacrylate (TPM) particles with mass density $1.30\,\mathrm{g\,cm^{-3}}$, refractive index of 1.517. Here we chose TPM as our model particle for its higher-than-water density, and its simple synthesis procedures. Particles were synthesised according to the recipe [70, 71], and Pluronic® F108 surfactant was added to the surface to reduce polydispersity and sterically stabilise the particles in solution [72]. Here the polydispersity is the ratio of the standard deviation over the arithmetic mean. We have prepared highly monodisperse particles of three different sizes: $1.8\,\mu\mathrm{m}$, $2.5\,\mu\mathrm{m}$, $3.2\,\mu\mathrm{m}$, with polydispersities smaller than 5%. The sizes and polydispersity were confirmed by using SEM.

The particles are washed carefully with (Type I) deionized water with a resistivity of 18.2 Ω, which means that a very low number of ions are dissolved, to wash out the residual salt and minimise the salt concentration in the final solution. It is then redispersed in deionized water to form a suspension at required mass fraction. When dispersed in deionised water, fully crosslinked TPM particles have a fairly large anionic surface potential, zeta potential was measured using Malvern Nano Z to be −34 mV. This leads to a short range repulsion between the particles, and between the particles and the wall of the cell, which strengthens the stability against aggregation and suppresses the tendency of particles to stick to the wall of the sample cell.

2.2.5 Sample cells

In our system, the Peltier plates beneath the sample cell act as a heat sink. All of the sample cells used are very thin to make sure that the sample inside reaches the temperature set by the Peltier plates very quickly, by transferring the heat through the bottom glass slide. Heat transfer through the top of the cell is negligible as heat transfer to the outside air by convection is much slower compared to the heat transfer through the bottom glass slide by conduction. Note that during freezing the system releases latent heat of solidification, but the effect on the temperature of the system is minimal; heat transfer through the bottom part of the cell is faster than through out the sample. Therefore it can be assumed that the temperature of the cell is equal to the temperature of the plate, and the temperature distribution along the gap between the plates is determined by convection through the cell bottom, which is a linear temperature gradient. Previously in our group, the temperature gradient has been measured using thermocouples, it has been found that at the low freezing velocity we use here, the temperature gradient is linear, with 0 °C measured between the plates, in agreement with the theoretical gradient [51].
Different types of sample cells were made and used in this thesis. In Chapter 3 to Chapter 5, the quasi-2D cell with a internal height of 4 µm, which corresponds to single particle diameter of our model system, was made from UV glue and glass substrates, using a negative polydimethylsiloxane (PDMS) mould. In Chapter 6, we started with conventional glass walled sample cells with a internal height of 0.12 mm, later the internal height and the materials of the sample cell were varied systematically. Figure 2.8 shows a schematic of the protocols for making each of the cells, which we describe below.

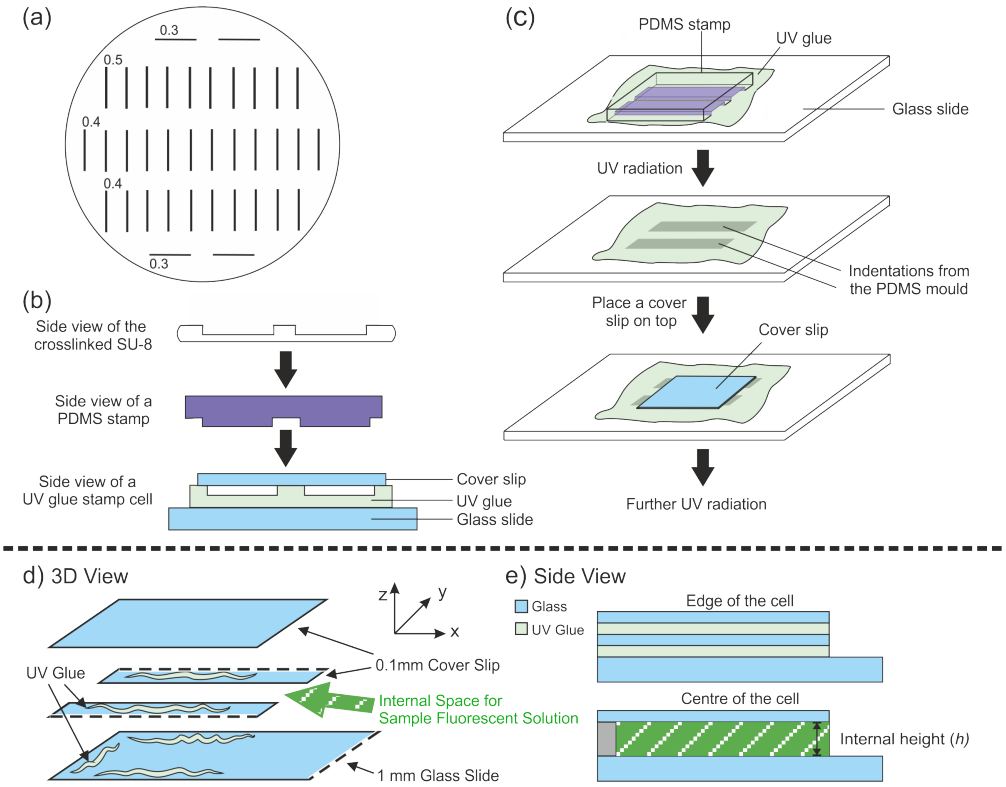


Figure 2.8: Diagram of the methods for making sample cells, (a), (b), (c) for making the 2D sample cells made from UV glue and (d), (e) for making the Hele-Shaw glass sample cells. (a) The design of a photomask, the black strips prevents the UV light shine through thus prevents crosslinking of the SU-8 beneath, leaving indents in the SU-8 coating on the wafer; (b) Top: Side view of the corsslinked SU-8; Middle: Side view of the PDMS stamp made from the SU-8; Bottom: Side view of the resulted sample cell; (c) Steps taken for making the sample cell. A PDMS mould stamping onto the UV glue, UV light was switched on to leave the channels indented but before the PDMS firmly bind with the UV glue. The PDMS stamp is then removed and a cover slip is quickly place over it. The device is then fully polymerised with UV radiation and the cover slip is firmly attached; (d) Components used for the glass cell, the dashed lines represent cut glass edges; (e) The side view of the glass cell, at the cell edge and the cell centre. The internal height is determined by the height of cover slip spacer and the UV glue heights.

UV glue sample cells

The SU-8 is a photosensitive polymer purchased from Chestech. Its formulation contains an epoxy oligomer with eight reactive acid-labile epoxy groups, which give a high degree of cross-linking under intense UV light [73]. This provides a way to create various designs. Here a photomask was designed in CorelDraw and printed onto a sheet of acetate using a high resolution printer provided by Micro Lithography Services Ltd., this mask creates regions that are exposed to the UV light and regions that are not, thus we can selectively choose the regions for crosslinking. The defined height of our quasi-2D cell is achieved using the properties of SU-8

photoresist, as it can be spin-coated at a well defined thickness onto a blank silicon wafer. The thickness of SU-8 is controlled by spin-rate, baking times and temperatures, which is listed in the official MicroChem Processing Guidelines [74]. To achieve a internal height of 4 µm, the SU-8 was treated as follows. Note that all the steps are carried out at room temperature unless otherwise stated.

1. Centrifuge the SU-8 2005 photoresist polymer for 2 minutes at 2000 rpm to remove bubbles.
2. Preheat the wafer for 5 minutes at 65 °C to remove any unwanted moisture from the surface of the blank silicon wafer.
3. Spin-coat the wafer with 5 ml of SU-8 2005 for 30 seconds at 500 rpm with an acceleration of 100 rpm/s, followed by 65 seconds at 4000 rpm with an acceleration of 300 rpm/s.
4. Leave the SU-8 to settle for 10 minutes before soft baking at 65 °C for 2 minutes 30 seconds, then at 95 °C for 3 minutes 30 seconds.
5. Cover the wafer with the photomask (design in Figure 2.8 (a)) and a glass UV filter to minimise Fresnel diffraction which reduces resolution [75] hold down the glass filter and photomask to avoid unwanted diffraction caused by the presence of gaps.
6. The wafer was exposed under 2.7 Watts UV light for 30 seconds for the crosslinking of SU-8 to happen.
7. Photomask was removed and the wafer was baked at 65 °C for 2 minutes then at 95 °C for 3 minutes 30 seconds.
8. The wafer was washed in propylene glycol methyl ether acetate (developer) for 1 minute to dissolve any SU-8 that was not cross-linked. Any excess developer was then washed off by spraying with isopropanol for 10 seconds.
9. The isopropanol was dried off with nitrogen gas and the wafer is then hard baked at 150 °C for 40 minutes. This ensures the SU-8 is securely bound to the wafer.

This wafer now acts as a reusable template to produce the PDMS devices. The edge of the wafer was then taped up to a desired height for the PDMS to pour in from the above. PDMS was mixed with curing agents at the ratio of 10:1 so that the product has the desired flexibility. The

mixture was first centrifuged to remove air bubbles and then poured onto the taped wafer. The device was left under vacuum suction for 30 minutes to remove any air bubbles formed during pouring, and the PDMS was then polymerised at 85 °C overnight. The polymerised PDMS layer was then peeled off and cut into individual PDMS stamps. These stamps with the designed channels is used as a reusable stamps to produce UV glue sample cells.

For each UV glue sample cells, 100 µl of NOA 81 UV glue (Norland optical adhesive 81) from Norland Products was placed in the middle of a microscope slide. The PDMS stamp was pushed in firmly, before irradiation with UV light to partially polymerise the glue (2.7 W, 30 seconds). Then the PDMS stamp was replaced by a square cover slip of similar size (15 mm x 15 mm), followed by further exposure to UV radiation (2.7 W, 1 minute) to produce a single-use UV glue stamp cell. The channels in the sample cells are with the internal height predetermined by the SU-8. All glass components used in this step were rinsed with ethanol and plasma cleaned to minimise any contaminants from the surface of the cell.

Glass sample cells with parallel walls

In Chapter 6, glass sample cells were used to record and reconstruct a complete 3D structure of the ice-water interface with good resolution. We adapted our design from the conventional glass cells with parallel walls, using 76 mm × 26 mm × 1 mm thick microscope slides and 22 mm × 50 mm × 0.1 mm thick cover slips. The microscope slide was used as the bottom, the cover slips were cut and fitted at the side as stepper, and another cover slip was used to seal the top. All glass components in the cell were rinsed with ethanol and plasma cleaned to minimise any contaminants from the surface of the cell, and were glued and sealed together by NOA 81 UV glue. This leaves one opening for sample solution insertion. Fluorescent solution was inserted from the top/open end, which was left open and placed on the cold plate to reduce evaporation during the imaging process.

Internal height can be varied by choosing cover slips with different thickness or number of cover slip used. For some later experiments, the bottom glass microscope slides was replaced by other materials to achieve different thermal conductivity, while retaining the same overall cell structure. One of which was using a cover slip coated in 225 µm SU-8 2035 at the top instead of the regular glass cover slip. The coating method was similar to the one described above, with

changes in type of the SU-8 photoresist polymer and the corresponding change in spin-coat setting and baking time, as recommended by the official guidelines [74], as well as without the steps of photomask as we want a uniform coat of the SU-8 photoresist over the cover slip.

2.2.6 Image analysis: particle detection

A typical image taken with a 50× objective containing a mixed ice-water-particle phase looks like Figure 2.9 (a). The particles present in the images are composed of a bright spot in the centre and a dark ring around. This is due to the incident light rays near the top of the particle being refracted according to Snell's law and focused towards its centre, while the incident light rays on the edge of the particle have an angle of incidence beyond the critical value and are thus reflected away from the particle [76]. In a bulk of particles where they are close to each other, the dark rings merge and produce a dark background thus their contours cannot be clearly identified individually, consequently the position of the particles can only be detected by their bright centres. Extracting the position of the particles in each frame is the starting point for all further analysis throughout this thesis, the routine of which is illustrated in Figure 2.9.

All image analysis was conducted in Mathematica. Starting from the original image (Figure 2.9 (a)), a binary image was created by replacing all values above a globally determined threshold with 1 and others with 0 (Figure 2.9 (b)). This threshold for binarization is found manually with several images for a single experiment and then applied to the whole data set. Due to the build up of the particles, the bulk melting temperature will change, thus resulting in the position of the ice-water interface shifting to one side of the observation window. This causes off centre illumination, which leads to a uniform binarization parameter not removing all of the unwanted bright (particle-like) signals. When the particle concentration is high, as shown in this example figure, some interstitial area among the surrounding particles may be greyer than the background due to the accumulation of deflected light. This causes more false positives for the uniform parameter.

Therefore, a step was required to filter out the incorrectly identified particles. Here we select the signals according to their geometrical properties, mainly size and circularity. The extracted information consists of an array of coordinates x_i and y_i, where i is a particle index, produced for each frame, which is plotted in Figure 2.9 (c). Figure 2.9 (d) also uses this centroid data,

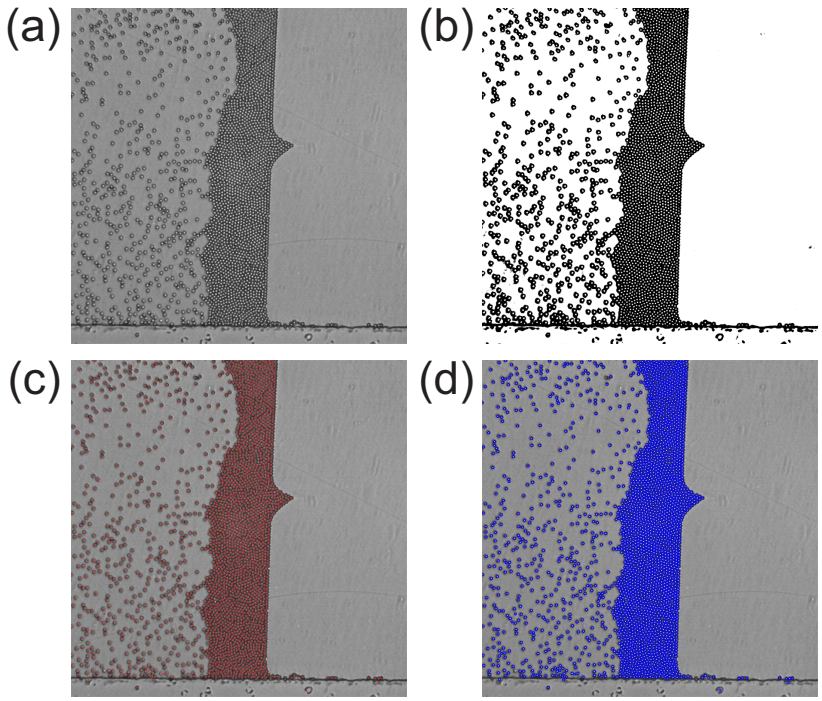


Figure 2.9: (a) Original image of a colloidal crystal; (b) The same image following the binarization procedure, here the binarization threshold is set to 0.5; (c) Extracted particle coordinates plotted back onto the original image, a total of 2720 particles were found in this frame; (d) Extracted particle peripheral plotted back onto the original image.

but uses a circle of the size of particle as the plot marker. This list of particle positions forms the basis for further analysis, which will be explained in the corresponding chapters.

Acknowledgments

Julia Schollick is thanked for help regarding the freezing set-up, glass sample cells with parallel walls (Hele-Shaw sample cells) and confocal microscopy. Arran Curran is thanked for helping to design and construct the optical microscope. The PTCL mechanical and electronic workshops are thanked for providing essential parts for the microscope. Jenny Kuo is thanked for testing the PDMS stamps. Louis Cortes is thanked for help regarding the micro-lithography.

Chapter 3

The Role of Particles in the Ice-Water Interface Instability

ABSTRACT

In this chapter we aim to separate the roles of salt and particles in causing the Mullins-Sekerka instability at the ice-water interface. It has been previously reported that the presence of salt ions is more important than the presence of the particles for the onset of supercooling in the system, but there have not been direct experimental comparison on their abilities to induce instabilities. We first describe the Mullins-Sekerka instability in a qualitative manner, and compare that to our observation of how freezing velocity has an impact on the pattern formation of a salt-water system. Then we introduce colloidal particles into the system and repeat the experiments in an identical salt environment to directly compare the resulting perturbations, which helps us to identify the role of the particles in the instability.

3.1 Introduction

Instability in unidirectional ice growth refers to the process where the ice-water interface deviates from a planar structure into a cellular (columnar) or a dendritic (branched) structure [16]. Everyday examples would be the beautiful patterns found in snowflakes [77], in industry as the underlying principle of freeze casting [16], and in laboratories where it is a crucial criterion in cryopreservation as the formation of sharp ice crystals affects the survival rates of the biological samples [18, 78]. This morphological instability is a nonequilibrium phenomenon that can also be found in other systems, such as the solidification of alloys, because the formation of the microstructures follows the same underlying mechanisms [77]. Consequently, these phenomena have been studied mostly by metallurgists who must deal with it in a very practical way in the design of materials [77, 79].

The final structure resulting from the instability is very sensitive to the growth environment. For example, because there is no internal control mechanism which coordinates the growth of the branches of a snowflake, the patterns in snowflakes respond sensitively to the external growth conditions [77]. The growth at any instant is governed by the external conditions, including the temperature, the humidity and the concentrations of various air pollutants, encountered as the developing crystal is carried through different regions of the atmosphere. Due to the high variability in these conditions, no two snowflakes are the same.

The instabilities go hand in hand with supercooling, the process where the temperature of the melt directly in front of the freezing interface is below its equilibrium freezing temperature [80, 81]. Supercooling is caused by the building up of solutes ahead of the interface during the growth of ice crystals [82]. Although it is known experimentally that colloidal suspensions can profoundly affect the nature of the instability [83], it has not been clear how to separate the effect of colloids from that of salt.

In this chapter we focus on identifying the individual roles of salt ions and colloidal particles in the ice-water interface instability. We will start with discussing the relative theories on instability and supercooling (Section 3.2), then we present the experimental apparatus (Section 3.3), before we present the results (Section 3.4). We finish the chapter with a conclusion (Section 3.5).

3.2 Theory

In this section we start by presenting the Mullins and Sekerka instability in Section 3.2.1, i.e. the underlying mechanisms for the pattern-formation processes in solidification. Then we move on to discussing the causes and effects of supercooling in a colloidal suspension in Section 3.2.2. We finish the section by discussing the roles of particle and salt in supercooling in Section 3.2.3.

3.2.1 The Mullins-Sekerka Instability

The instability can grow favourably under certain conditions. Consider a sinusoidal perturbation of an infinitesimal initial amplitude that is introduced to the planar solidification front. There are associated stabilizing and destabilizing factors that compete to determine whether the instability grows or decays. Mullins and Sekerka developed a model for the amplification rate of an arbitrary perturbation that can be used to determine the primary periodicity of the resulting structure. The resulting equation predicts that the amplification rate follows the dispersion relation below [84–86]:

$$\frac{\dot{\delta}}{\delta} = \frac{Vq\left\{-2T_m\Gamma q^2\left[q^* - \frac{V}{D}(1-k)\right] - 2\nabla T\left[q^* - \frac{V}{D}(1-k)\right] + 2mG_c\left[q^* - \frac{V}{D}\right]\right\}}{2\nabla T\left(\frac{k_i - k_w}{k_i + k_w}\right)\left[q^* - \frac{V}{D}(1-k)\right] + 2qmG_c}. \tag{3.1}$$

Here

$$q^* = \frac{V}{2D} + \left[\left(\frac{V}{2D}\right)^2 + q^2\right]^{\frac{1}{2}}, \tag{3.2}$$

and δ is the amplitude of the perturbation with a growth rate of $\dot{\delta}$, V is the growth velocity (corresponding to the speed of the motor in our system), q is the wavevector, T_m is the bulk melting temperature, Γ is the ratio of the surface tension γ_{iw} and L_m, the latent heat of fusion per unit volume, i.e. $\Gamma{=}\gamma_{iw}/L_m$, D is the diffusion coefficient, k is the segregation coefficient, ∇T is the temperature gradient, m is the slope of the liquidus, G_c is the concentration gradient at the interface and k_i and k_w are the thermal conductivities of ice and water. A positive value on the right hand side of Equation 3.1 implies the environment favours the growth of the instability and allows parts of the ice front to grow further into the liquid. A negative value thus implies the instability at this wavelength will decay instead.

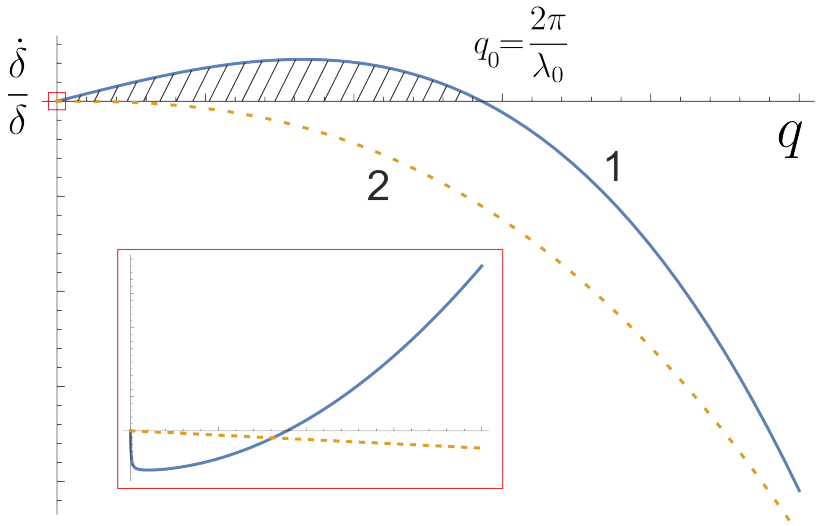


Figure 3.1: $\dot{\delta}/\delta$ as a function of frequency for two cases: unstable (curve 1), stable (curve 2) [84]. Inset showing the stability we have at very long wavelength.

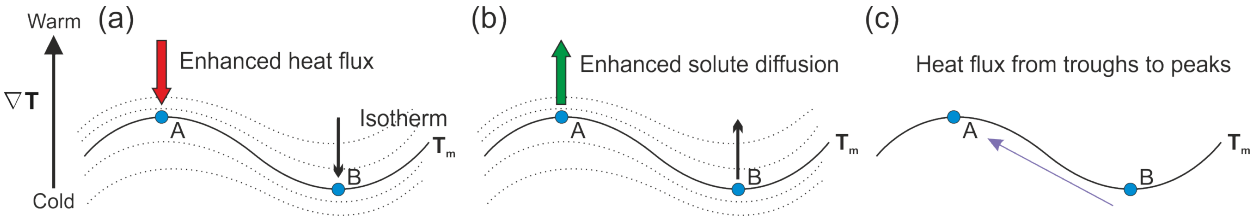


Figure 3.2: Schematic diagrams shows (a) a stabilising thermal field, (b) a destabilizing compositional field, and (c) a stabilizing surface energy.

Equation 3.1 is effectively composed of three competing terms: surface energy cost when a sine wave is introduced (first term), thermal field (second term) and the effect of solute on equilibrium melting temperature (last term). These opposing factors lead to a dispersion relation with a critical wavelength, λ_0, above which (i.e. $q < q_0$) a perturbation will grow, and below which the perturbation decays (Figure 3.1). At very long λ (very small q), the interface is again stable.

Now let us focus on the three components separately. Firstly (i), we look at the stabilising thermal field (Figure 3.2 (a)). Heat is always transferred from hot to cold, and with a larger temperature gradient the rate of heat transfer is faster. Here we use an arrow representing the direction and their size to represent the magnitude of the heat transfer. In the diagram, isotherms are drawn as dotted lines close to the interface. When we introduce a perturbation to the interface, the isotherms are deformed in response to the new boundary conditions: they are compressed near peaks in the interface, enhancing the heat flux at those points, and expanded near the troughs, suppressing the heat flux [55]. As a result, at the peaks, the temperature gradient is large and there will be enhanced heat transport from liquid to solid relative to that

for the planar system. Similarly, less heat will be transported to the troughs and the rate of solidification is locally increased. This leads to the inhibition of the growth of ice at the peaks, while reinforcing it at the troughs, stabilizing the overall interface by leaving out any deviations from a planar interface.

Secondly (ii), we look at a destabilizing compositional field (Figure 3.2 (b)). Analogous to thermal isotherms, surfaces of constant concentration are also compressed near peaks in the presence of a perturbation, enhancing the flux of solute away from the interface. We know that the presence of solutes inhibits the growth of ice via freezing point depression. Therefore at the maxima, ice grows more quickly due to an increase in flux of solutes diffusing away, leading to an instability. Conversely at the minima, solutes diffuse away more slowly, and the resultant build up of solutes over time limits the ice growth in the troughs.

Thirdly (iii), we look at a stabilising surface energy. We first consider the effect of surface tension on interface stability. The free energy cost is associated with the creation of additional interfacial area when perturbations are introduced, thus limiting the growth of instability. This energetic penalty increases with decreasing wavelength. There is also a change in local temperature gradient when the interface becomes curved. Mullins and Sekerka concluded that the change in melting temperature is related to the curvature via the following equation [84]:

$$T'_m = T_m + T_m \Gamma \kappa, \tag{3.3}$$

with κ the curvature at a point of the interface. Here, κ is defined as positive when concave towards the liquid (point B in Figure 3.2 (c)). This give rise to a heat flux from B to A, which stabilizes the interface and restores the planarity of the interface.

Note that these three mechanisms operate on three different lengthscales. In decreasing order they are: the thermal diffusion lengthscale, the compositional diffusion lengthscale, and the capillary lengthscale. This explains Figure 3.1: at short wavelengths, the stabilising surface energy dominates, thus perturbations with small λ are unable to survive due to the Gibbs-Thomson effect. At long wavelengths, the thermal field dominates, meaning the perturbations with large λ are unable to survive. At intermediate wavelengths, the instability will grow, with an optimum wavelength which gives the fastest instability growing speed. This corresponds to the apex of the peak in the Figure 3.1.

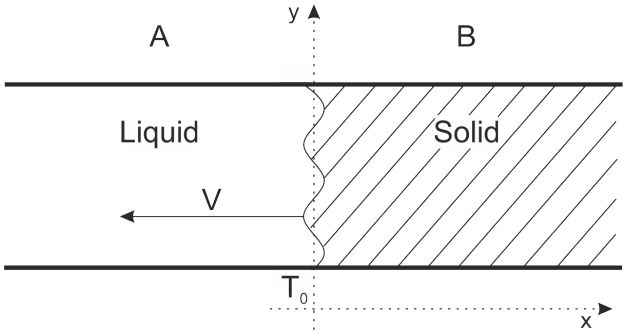


Figure 3.3: Schematic representation of a directional-solidification experiment.

3.2.2 Supercooling

For our unidirectional freezing set-up (Figure 3.3), we assume the thermal conductivities are the same in both liquid and solid phases, so that the temperature throughout the region (A-B) can be written as

$$T = T_0 + \nabla T x. \tag{3.4}$$

Here, x is the position coordinate as shown in Figure 3.3, T_0 is the reference temperature at the position of the interface, and ∇T is the temperature gradient. When freezing an aqueous solution with an initial bulk salt concentration C_0 at slow freezing velocity, the solute molecules are excluded from the ice crystal due to the very low solubility in ice. This gives rise to an increased solute concentration ahead of the advancing interface, $C_{Int} = C_0/k$, where k is the segregation coefficient, defined as the ratio of concentrations in ice and water. The segregation coefficient is very small here as the solubility of solute in ice is very low, thus $C_{Int} > C_0$, and this gives rise to a concentration gradient in front of the ice-water interface [87]. This is systematically represented in Figure 3.4 (a), where the T axis is equivalent to the x axis in Figure 3.3 according to Equation 3.4, but in the opposite direction, and the composition profile C_L is drawn as the dashed green line. The two solid lines are the solidus line and the liquidus line of the system. Therefore the intersection of the vertical line, $C = C_0'$, with the solidus line determines the bulk freezing temperature T_0, and hence the position of the interface [77]. The concentration ahead of the interface is determined by the following two processes [88]:

1. The diffusion of solute in the liquid, governed by the diffusion coefficient D.

2. The process of freezing that provides a continuous supply of solute particle at the ice-water

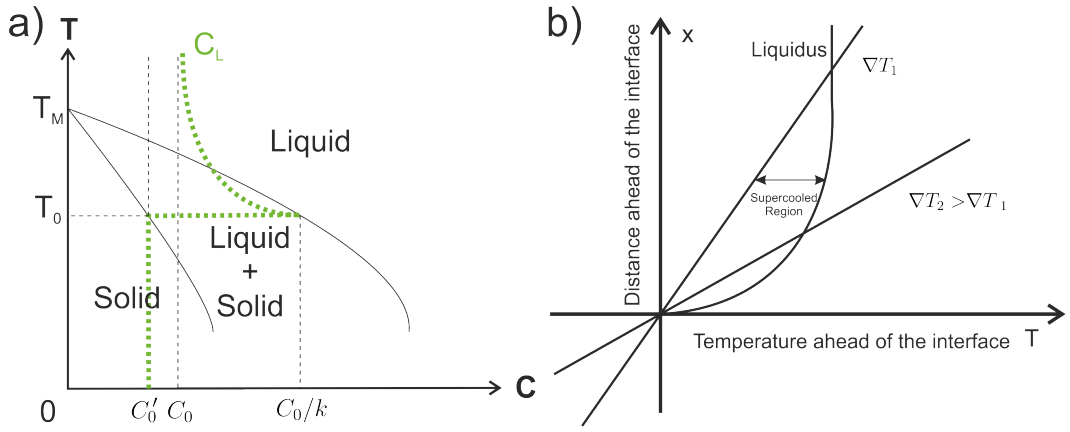


Figure 3.4: (a) Part of a temperature-composition phase diagram for a binary solution. The dashed green line shows the distribution of solutes in the neighbourhood of a flat ice-water interface for a system undergoing directional solidification. (b) Schematic graph plotting the effect of constitutional supercooling on the liquidus temperature as a function of x. The liquidus line is inversely proportional to the compositional distribution of solute that builds up at the interface. The supercooled zone (area enclosed by the temperature gradient imposed and the liquidus line) for ∇T_1 is bigger than that of ∇T_2, and thus the degree of supercooling is bigger at lower temperature gradient.

interface. This is determined by the freezing velocity, V.

Here the concentration gradient increases as the freezing velocity increases, this in turn causes greater freezing point depression which shifts the concentration profile further into the two-phase region, leads to an unstable interface.

The accumulation of solutes in front of the interface causes freezing point depression, giving rise to the formation of a constitutional supercooling zone, in which the temperature of the melt directly in front of the freezing interface is below its equilibrium freezing temperature [86, 89]. This is shown schematically in Figure 3.4 (b). Here the curved line shows the liquidus temperature, which is directly determined by the solute distribution, as every point in the liquid ahead of the interface has a definite solute concentration that lowers T [88]. The straight lines are the systematic temperatures determined by the two different external temperature gradients. The point of intersection of the curved and straight lines ($x \neq 0$) gives the width of the supercooled zone [88]. We can clearly see that there is a larger supercooled region with the smaller temperature gradient.

This supercooling causes a local inversion of the temperature gradient at the interface, which reverses the role of the stabilising thermal field in the instability, making it favourable for the instability to grow instead. In Figure 3.5 we again illustrate the effect of the thermal field on

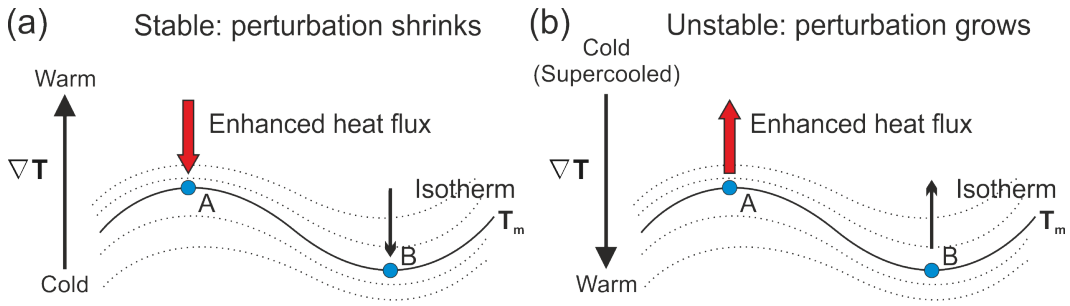


Figure 3.5: Heat transfer response to a perturbation in a ice-water interface under different conditions. (a) Without supercooling, the heat transfer occurs in the direction so that the perturbation shrinks; (b) With the supercooling, the heat transfer occurs in the direction preferring the growth of the perturbation.

an interface perturbation, under both the normal temperature gradient and the locally reversed temperature gradient. When ice grows into supercooled water, it experiences the reversed temperature gradient. This is because the temperature of the nucleated ice is determined by the liquidus temperature, while the region ahead of it is still supercooled. Consequently the direction of the heat transfer is reversed as heat transfer is always from warm to cold, while the magnitude of the heat transfer remains the same, as it is determined only by the isotherms. This indicates that the stabilising thermal field term in the normal situation becomes a destabilising term when supercooling is present, as it encourages the growth of the peaks.

3.2.3 The effects of particles in supercooling

The system we are interested in is a colloidal suspension, where both colloidal particles and salt ions exist. During unidirectional freezing at a small velocity, both the particles and salt will build up in front of the ice-water interface, and subsequently have their own contribution to the supercooling and the instability. It is important to determine their individual contributions to the instability during the solidification of colloidal suspensions, not only for improving the fundamental understanding of the pattern formation process, but also for a better control of the final structure. For example in freeze casting, if the effect of the particles is dominant, then the final structure (resulted from the freezing pattern) can be modulated by changing the particles (surface chemistry, size, shape, etc.). Otherwise, we can tune the structure by changing the salt concentration in the system.

The roles of particle and salts in solution have not yet been clearly separated, especially if the particle concentration is high, as most theoretical and experimental studies have focused

on the interaction between an isolated colloidal particle and the solid-liquid interface [61, 90]. Peppin *et al.* have found that the colloidal suspension can become unstable in the absence of electrolytes, however the effect of salt ions on concentrated colloidal suspensions remains to be determined [91]. Recently, You *et al.* [92] carefully designed an experiment to directly compare the freezing process of a particle suspension and its supernatant. Their results indicated that interfacial undercooling mainly comes from the additives in the solvent instead of the particle themselves. This was the first report on the quantitative measurements of interfacial undercooling during the solidification of colloidal suspensions. From their results and based on our understanding of the relationship between supercooling and instability, one would expect a stronger supercooling would cause the instability to grow faster, and therefore salt would be a more dominant factor in the final structure formed by the instability. However, as the diffusion constant of particles is smaller than that of the salt, one might also suspect that the particles would have a greater influence on the compositional field term in Equation 3.1. This is because a larger diffusion constant indicates the salts diffuse out faster than the particles, thus we have a greater concentration of particles in front of the interface, contributing to the supercooling. Here we will focus on studying this pattern formation experimentally, to elucidate the role of particles in the system.

3.3 Experimental methods

The colloidal system used in this chapter was the 2.5 µm monodisperse TPM system described in Section 2.2.4. Because inevitably there will be some salt carried over from synthesis even after repeated washing of the particles with deionised water, we use it to our advantage by taking the supernatant from the same sample as the control group to ensure it has the same salt concentration as the sample with the particles. UV glue sample cells with a height of approximately single particle diameter, and a width of 400 µm were prepared as described in Section 2.2.5. The sample cells were placed on to the freezing stage under the bright-field microscopy set-up described in Section 2.2.2. With our freezing stage, we can independently vary the solidification velocity (adjusted by the stepper motor) and the temperature gradient (established by the Peltier modules) with high precision. The temperature of the cold plate was first set to $-40\,^{\circ}\mathrm{C}$ to initiate the formation of the ice phase. It was then adjusted to $-10\,^{\circ}\mathrm{C}$ for the cold plate and $10\,^{\circ}\mathrm{C}$ for the hot plate to achieve the desired temperature gradient. The system was equilibrated

at a set temperature gradient, ∇T, of $10\,\mathrm{K\,mm^{-1}}$ for 30 min, after which, the sample cell was moved at prescribed speed through the steady temperature gradient controlled by the Linksys32 software, and data was recorded at 1 fps until we have reached the end of the sample cell, to ensure that the whole freezing process is captured.

The 20× Olympus Long Working Distance M-Plan Fluorite objective was used in the experiments to capture the overview of the structure formation. This provides a field of view of approximately $683\,\mu\mathrm{m}\times683\,\mu\mathrm{m}$. But as the channel is only $400\,\mu\mathrm{m}$ wide, we crop the image to $683\,\mu\mathrm{m}\times400\,\mu\mathrm{m}$ to present in the results section.

3.4 Results

3.4.1 Influence of velocity on instability

We start by exploring how the freezing velocity affects the interface instability. Typical microscopy images capturing the interface instability at different times are shown in Figure 3.6. The hot and cold plates are located on the left and right hand side, outside the field of view, so the liquid is on the left side and the ice is on the right hand side. Although they look identical as their refractive index are very similar, the difference in refractive index is still large enough to create a mismatch at the interface, which has been highlighted with the red line. There are also a trace amount of particles in the frame, which helps to identify the position of the interface. As the experimental channels are of the same length, experiments at different velocities will take different times to reach the other side of the channel, thus here we present the timing as t/t_{total} instead of the absolute timing.

For a freezing velocity of $1\,\mu\mathrm{m\,s^{-1}}$, the interface remains stable and planar throughout the whole experiment. This means that the accumulation of the salts in the experiment is not large enough to cause sufficient undercooling at this translational velocity. There are several instances where we find a small perturbation (for example Figure 3.6 (a, i)), but these perturbations quickly decay away and/or translates themselves to the edge of the cells, disappearing at the edges (Figure 3.6 (a, ii)).

For a freezing velocity of $2\,\mu\mathrm{m\,s^{-1}}$, initially the results are not found to be too different from that of the lower velocity, but towards the end of the experiment, we found that instead of decaying away quickly, the perturbations became long lived (some perturbations appeared at $t/t_{tot} \sim 85\%$

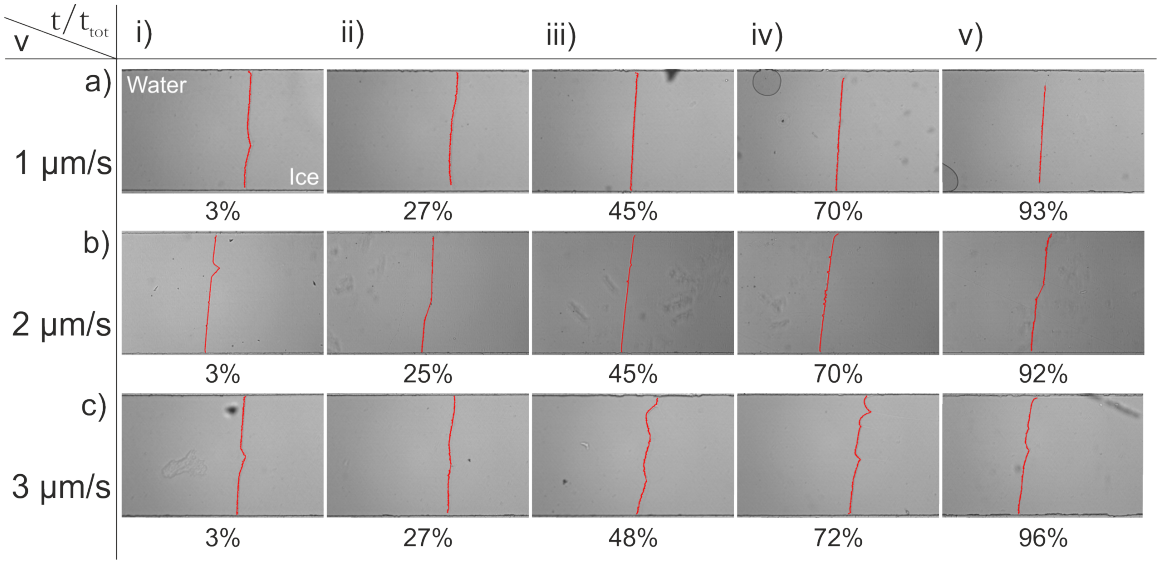


Figure 3.6: Snapshots from the freezing of supernatant at different freezing velocity under a temperature gradient of $10\,\mathrm{K\,mm^{-1}}$. Here the solution is on the left side and the solidified ice is on the right side.

and remained until we reached the end of the channel). However these perturbations do not have the chance to fully develop into an instability.

For a freezing velocity of $3\,\mu\mathrm{m\,s^{-1}}$, we observed that the perturbations were able to remain in the system at a much earlier time (from Figure 3.6 (c, ii)). Note that as the sample cells were identical, the volume of solution used in the experiment was identical, thus the initial salt concentration and the total amount of salt present in the system were identical. Therefore the difference here must come from the different freezing velocities.

Overall, we have observed the trend where a higher freezing velocity gives rise to a more unstable ice-water interface. With a higher freezing velocity, there is a higher concentration gradient formed in front of the interface as there is less time for the salt to diffuse away. This strengthens the destabilizing compositional field term in the Mullins-Sekerka instability (Equation 3.1) and leads to the occurrence of the perturbations. As such, with the continuation of the experiment, more salt accumulates in front of the interface and the salt gradient increases further. This leads to the growth of the perturbation in terms of wavelength, as shown in Figure 3.6 (c, iii to v) and will be discussed in more detail in the following section. Note that the sample reached the other side of the channel before a fully developed instability can appear.

Table 3.1: Constants used for evaluation of the model

Constant	Value
m	$-103.4\,\mathrm{K}$
C_0	$7.5\,\mathrm{mM} = 0.0135\,\%$
D	$10^{-10}\,\mathrm{m^2\,s^{-1}}$
T_m	$273\,\mathrm{K}$
Γ	$= \gamma_{iw}/L_m$=$8.74 \times 10^{-11}\,\mathrm{m}$
∇T	$10\,\mathrm{K\,mm^{-1}}$

3.4.2 Estimation of instability kinetics

The theory developed by Mullins-Sekerka describes the interface's tendency to become unstable through the dispersion relation Equation 3.1 [84]. Kurz and Fisher used a simplified version of the dispersion relation for a planar solid-liquid interface assuming equal thermal conductivities in solid and liquid [93, 94]. This simplifies Equation 3.1 to:

$$\frac{\dot{\delta}}{\delta} = \frac{V}{mG_c}\left(-T_m\Gamma q^2\left[q^* - \frac{V(1-k)}{D}\right] - \nabla T\left[q^* - \frac{V(1-k)}{D}\right] + mG_c\left[q^* - \frac{V}{D}\right]\right). \tag{3.5}$$

Next, by assuming k, the segregation coefficient, to be very small ($k \approx 0$), they obtained:

$$\frac{\dot{\delta}}{\delta} = \frac{V}{mG_c}\left(q^* - \frac{V}{D}\right)\left(-T_m\Gamma q^2 - \nabla T + mG_c\right), \tag{3.6}$$

Here, we use Equation 3.6 to predict the dominant perturbation wavelength in our system, and we will compare it to our observations. The numbers in Table 3.1 were used in the calculation. The slope of the liquidus line m was calculated using $-RT^2/L_m$. To calculate G_c, we use the following equation in terms of the wavelength λ, $\lambda = 2\pi/q$, suggested by Kurz and Fisher [93]:

$$G_c = \frac{C_0}{\frac{\lambda}{2} - \frac{D}{V(1-k)}}. \tag{3.7}$$

Note that C_0 is the salt concentration in the supernatant expressed as mole fraction. We obtain C_0 by comparing the level of undercooling in the system through a 'standpipe experiment' [95], where we have two side-by-side channels on a single sample cell, filled with the supernatant or with NaCl solution with known concentrations (1 mM or 10 mM). The sample was brought to freezing under a uniform temperature gradient of $10\,\mathrm{K\,mm^{-1}}$ and stabilised for an hour. The

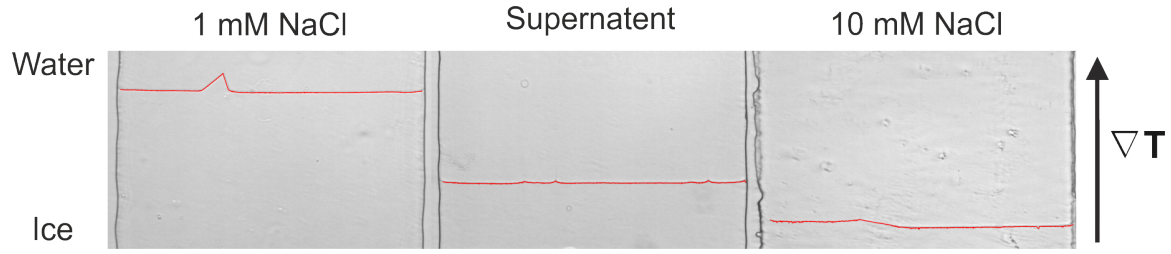


Figure 3.7: Images comparing the position of the interface for 1 mM and the supernatant of the TPM solution.

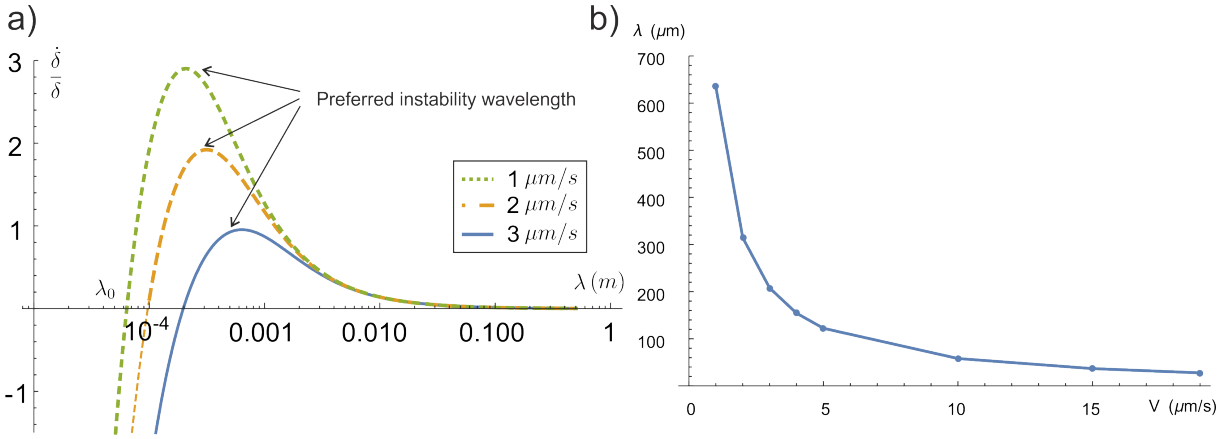


Figure 3.8: (a) Growth rate of perturbation, $\dot{\delta}/\delta$, on planar solid liquid interface at the limit of stability, as a function of wavelength, λ. (b) The preferred instability wavelength for different freezing velocities.

resulting interfaces are shown in Figure 3.7. As the interface for the supernatant lies at about 75% between the interfaces for 1 mM and 10 mM NaCl, we estimate the salt concentration in the supernatant is 7.5 mM thus a mole fraction of 0.0135%.

For the other terms, q^* was used as defined in Equation 3.2, and Γ was defined as the ratio of the surface tension γ_{iw} and L_m (numerical value taken from [96]). As the identity of the ions present in the supernatant is unknown, the diffusion constant D was estimated from literature for a range of solutes, to the nearest power of 10 [86, 97]. The resultant plot for different freezing velocities is shown in Figure 3.8 (a). As in Figure 3.1, we have also indicated the critical wavelength. Note here we can see that the stability at long wavelengths disappears compared to Figure 3.1 ($\dot{\delta}/\delta$ goes to zero instead of negative), this is due to the simplification of the thermal conductivity terms.

Therefore from Figure 3.8 (a), we can deduce the preferred instability wavelength for each freezing velocity, which corresponding to the highest peak of the relative variation in amplitude. This relation is shown in Figure 3.8 (b) for a range of velocities. For the actual velocities used in our

experiment, a maximum was found at around 635 µm for the freezing velocity of $1\,\mu m\,s^{-1}$, for $2\,\mu m\,s^{-1}$ around 315 µm and for $3\,\mu m\,s^{-1}$ around 200 µm. In our experiments, for $V = 1\,\mu m\,s^{-1}$ we did not observe any stable perturbations, for $V = 2$ and $3\,\mu m\,s^{-1}$ we reached the end of the channel before a metastable instability was obtained. Nevertheless, we can clearly see the growth of the perturbations at the velocity of $3\,\mu m\,s^{-1}$ in Figure 3.6 (c, iii - v), from a smaller wavelength to a longer wavelength that is closer to the preferred instability wavelength, justifying what we expect from the theory. We believe if our sample channels were sufficiently long, the perturbations might be able to fully develop into an instability, with the wavelengths corresponding to our calculations.

3.4.3 The role of particles in interface instabilities

We now repeat the above experiment using the colloidal suspension as our sample. Typical microscopy images capturing the interface instability at different times are shown in Figure 3.9. Similarly to Figure 3.6, each image has clear sections of liquid, particles and ice from left to the right. As the salt concentration is the same as for the sample of supernatant, any differences in the results can be attributed to the presence of the particles.

Again, we first examine the freezing velocity of $1\,\mu m\,s^{-1}$. Overall the interface remains stable and planar throughout the whole experiment, similar to what we have seen in the case without particles. This again means the accumulation of the solutes in front of the interface is not large enough to cause sufficient undercooling at this translational velocity. However, if we zoom in at each frame (Figure 3.9 (d)), we can see that the interface is more active with small perturbations constantly appearing and decaying away. This suggests we are close to the onset of a long living perturbation or even an instability.

However, for the freezing velocity of $2\,\mu m\,s^{-1}$, we see a clear difference compared to that of the supernatant only sample, throughout the whole experiment. The perturbations are long lived from early on in the experiment, resembling what we observed at the very end in the experiment without the particles. Furthermore, as we approach 60% of the experimental time, we start seeing the perturbations evolving to instabilities, and resulting in the formation of ice-fingers. Here we see a clear difference compared to the case without the particles, purely due to the presence of the particles.

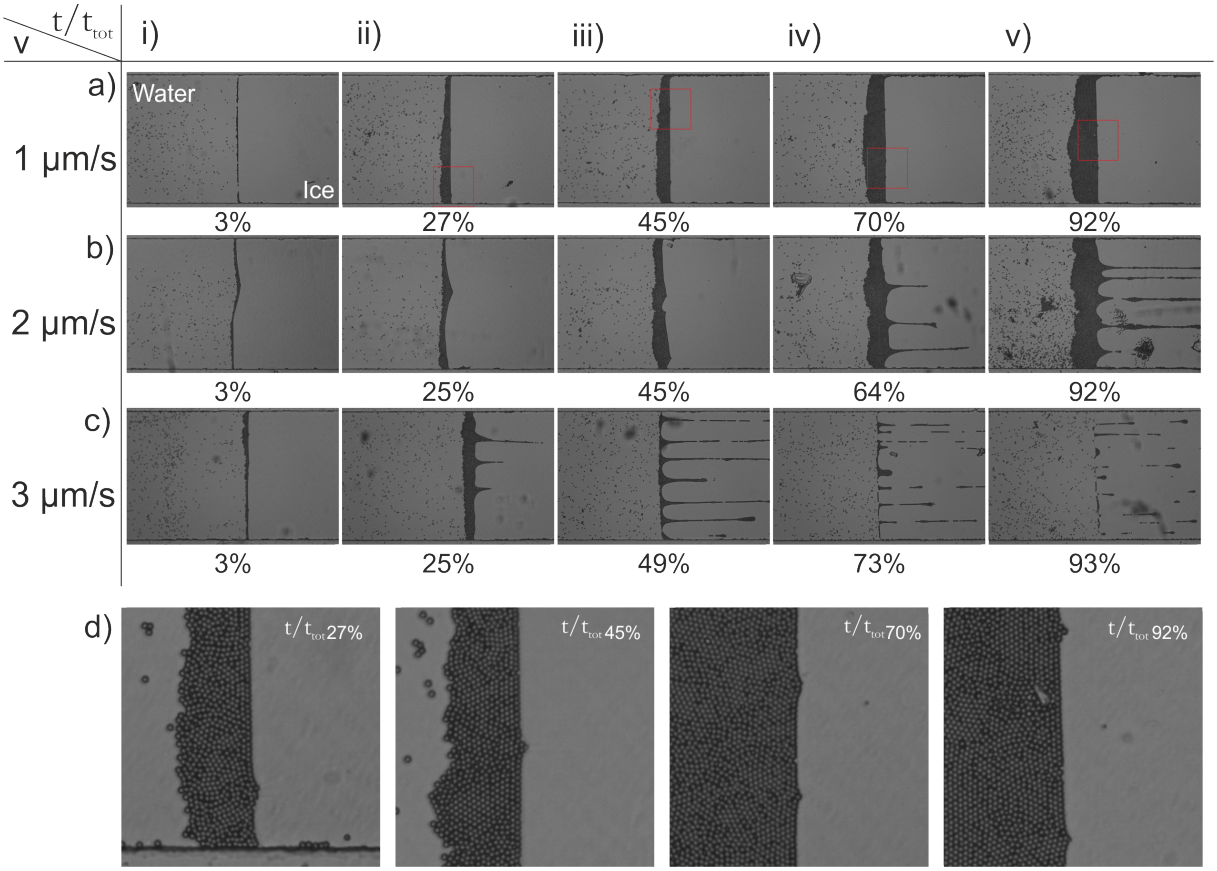


Figure 3.9: Snapshots from the freezing of the colloidal suspension at different freezing velocity ((a) $1\,\mu m\,s^{-1}$, (b) $2\,\mu m\,s^{-1}$, (c) $3\,\mu m\,s^{-1}$) under the temperature gradient of $10\,K\,mm^{-1}$. In each image, water is on the left side and ice is on the right side. Particles are accumulated in front of the ice-water interface in the solution, until being engulfed by the ice as the instabilities occur. (d) Corresponding zoom in sections of the perturbations in (a)(ii-v).

Next, we look at the results from freezing at $3\,\mu m\,s^{-1}$. At this freezing velocity, we are able to see the formation of the ice-fingers at a much earlier stage, around 25% through the experiment (Figure 3.9 (c,iii)), which is in line with the trend regarding the effect of the higher freezing velocities we have observed from the previous experiments. As the experiment continues, we can also see that the ice-fingers split and evolve into a finer structure, which we will discuss in more detail in Section 3.4.4.

Overall, with this set of experiments, we not only reconfirmed the effect of the velocity on instability, but also clearly showed the effect of the particles on instabilities. We speculate these differences come from the smaller diffusion constant of the particles compared to the salt ions. Previously, researchers have concluded that chemical diffusion is more important than thermal diffusion regarding the onset of interfacial instabilities [77]. This is because the diffusion of chemical species controls the motion of a solidification front in a manner exactly analogous to

the way the motion is governed by thermal diffusion for a pure substance. Therefore as thermal diffusion is always much faster than chemical diffusion, temperature deviations must relax in times much shorter than the time required for rearrangement of chemical species. Thus, solidification is effectively isothermal and chemical effects are dominant. Here in our system with both the particles and salt ions, the particles build up a concentration gradient in the same manner as the salts, but the difference in diffusion constant causes the particles to have a longer relaxation time, which makes it the more dominant factor in inducing the instability.

3.4.4 Instability wavelength and the freezing velocity

There has been extensive research on the formation of ice fingers, as it is a common feature of many solidification processes, for example in freeze casting. However, they use much smaller particles (usually $\sim$ 100 nm) compared to our experiments. It has been found that the faster the freezing rate (V), the finer the microstructure (indicated by the smaller wavelength λ), and the relationship can be described by a simple power law $\lambda \sim V^{-n}$ [87, 98]. The value of n depends on the size of the particles. When making porous alumina by controlled freezing of alumina particle slurries, if the particles are 400 nm in size, $n \approx 1$, but when the particle size is decreased to $\sim$ 100 nm, n $\approx 2/3$ [87].

In our experiment, as we only have data points from two different velocities, it is not suitable here to use the power law to describe the data. Nevertheless, we were able to observe the dynamic process of ice-fingers breaking down to the finer structures that are predicted by the power law at higher freezing velocities. For the freezing velocity of $2\,\mu m\,s^{-1}$ (Figure 3.10 (a)), we have a stable wavelength of the fingers at $\sim 90\,\mu m$. However, at the very end we see the beginning of the splitting events where the new instabilities appears at the interface and break the existing instabilities into approximate halves (Figure 3.10 (c)). For the freezing velocity of $3\,\mu m\,s^{-1}$ (Figure 3.10 (b), we initially have the instabilities at a wavelength of $\sim 70\,\mu m$ at t/t_{tot} = 27%, which evolves to finer structures at $\sim 60\,\mu m$ at t/t_{tot} = 49%, and in the end it starts to show the possibility of getting even finer structures (t/t_{tot} = 98% and Figure 3.10 (d)). Furthermore, we can see with the onset of instabilities, the particles are removed from the interface and get entrapped between ice fingers. This confinement gives the particles either a linear or zig-zag structure (Figure 3.10 (d)). In the next chapter we will focus more on these structures,

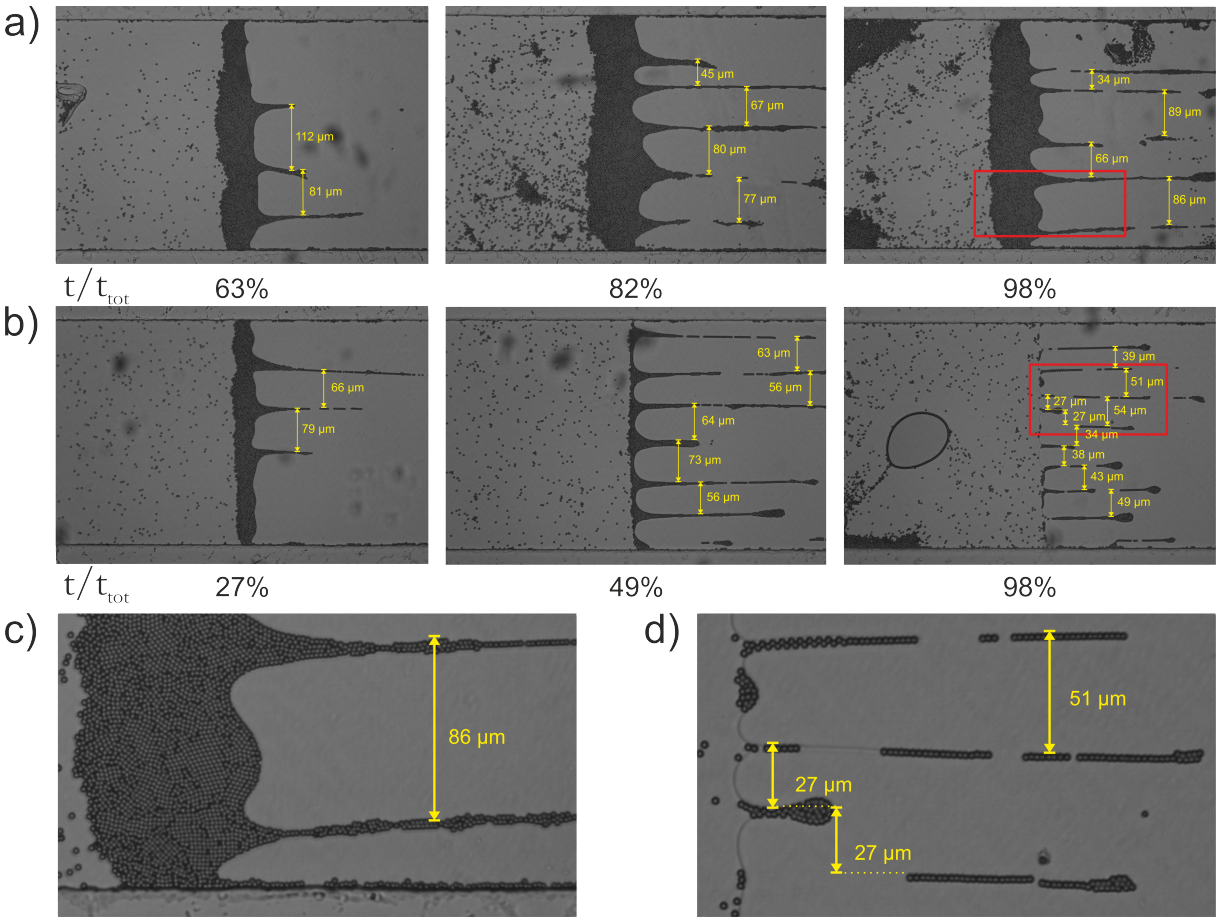


Figure 3.10: Representative snapshots chosen from the freezing of the colloidal suspension at (a) $2\,\mu m\,s^{-1}$, (b) $3\,\mu m\,s^{-1}$, with the measured wavelengths indicated on the figures. It is from the same experiment as Figure 3.9 but at different times. The enlarged view of the rectangular section in the last frame for the two freezing velocity is shown in (c) and (d) respectively.

both in front of the interface and in between the ice fingers.

3.5 Conclusions and outlook

In this chapter we tried to separate the roles of salt and particles in unidirectional freezing of colloidal suspensions and the formation of Mullins-Sekerka instability. We first described the salt induced instability by using the Mullins-Sekerka's dispersion relation. We then introduced the particles into our system while maintaining the salt concentration the same. Previously, researchers have found that the salt is more important for supercooling [92]. Although supercooling and instabilities are closely related, here we found that the particles are more important

in the formation of instabilities at the ice-water interface. We attribute this to the difference in diffusion constant, in an analogous argument to the diffusion of solute being more important than thermal diffusion, due to the difference in diffusion constant [77]. Further experiments can focus on bringing the experimental observations and the numerical predictions closer to each other, by re-designing longer microfluidics channels such that there would be more room for the instability to fully develop for the pure salt case. A repeat of the freezing of the colloidal solution in more velocity regimes would also be beneficial, to check the validity of the power law for the relation between the wavelength and freezing speed for large colloidal particles.

Acknowledgments

Jenny Kuo is thanked for preliminary experiments. Louis Cortes is thanked for discussions on making the UV stamp sample cells. Yanyan Liu and Taiki Yanagashima are thanked for discussions on synthesis of the TPM particles. Joe Hutchinson is thanked for proof reading.

Chapter 4

Pattern Formation in Freezing Colloidal Monolayers in Ice

ABSTRACT

We exploit the low segregation coefficient of ice, the ratio of impurities in the solid phase to that in the liquid phase, to concentrate the particles into a close-packed layer ahead of the ice-water interface. With the thickening of this layer, the osmotic pressure builds up, eventually causing breakthrough events whereby the particles are engulfed by the ice. To study this process, we fabricate single-particle thickness channels made from UV glue to minimise the 3D effects in the system and ensuring good optical resolution. The typical pattern in the close-packed particle layer consists of locally ordered clusters. We apply various image analysis methods to study the effect of freezing velocity on the patterns formed by the particles, and the crystallinity of the constantly rearranging particle clusters pushed by the moving ice-water interface.

4.1 Introduction

The interaction between colloidal particles and ice is not only of particular interest in many daily phenomena but also has great impact in the fields of climate science, materials, molten metals, food and biology [10,16,50,99,100]. In particular, colloidal systems display a fascinating variety of patterns upon freezing [101]. Researchers have focused on the structure resulting from the packing of colloidal particles between different ice fingers, as it forms the basis of the modern technology of freeze casting [102]. In particular, researchers want to understand the ordering, packing, and orientation of particles related to the growing ice crystals, to produce highly ordered structures, including honeycombs [103, 104].

In contrast, the structure formed by the accumulation of the particles in front of the ice-water interface is rarely studied. However, this is also very interesting as it causes a gradual increase of the particle concentration, that might share some properties with other phenomena such as the drying of colloidal suspensions [105, 106] and the jamming of suspensions flowed through constrictions [107]. In the past decade, researchers have tried to reveal the mechanism of dynamic particle packing triggered by a moving ice front using experiments [108, 109] and simulations [110], but currently no theory can fully predict the morphology or detailed characteristics of particle packing. Some claim that ordered particle packing can be achieved from careful unidirectional freezing [108], while others claim that although the particles are close-packed, the resulting structure does not possess long range structural order [109, 110]. Despite this, most of the experiments were in the high velocity regime, which leads to different behaviour compared to freezing at low velocity. For example, interesting phenomena such as crystals transversely spanning the entire freezing zone only occurs in the high velocity regime [111].

In this chapter, we aim to elucidate the complex behaviour in freezing colloidal suspensions, focusing on the pattern formed by the colloidal particles built up at the ice-water interface. This is achieved through in-situ observation of dynamic particle packing on the scale of individual particles, at relatively low velocities, such that particles can be rejected and pushed along. This chapter is organised as follows: we first discuss the forces in our system relating to particle engulfment and the theory of instabilities caused by solute effect in Section 4.2. The description of the experimental methods is given in Section 4.3, and the results follow in Section 4.4. Finally we conclude our findings in Section 4.5.

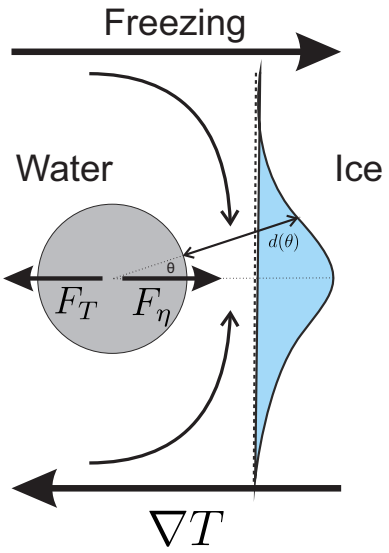


Figure 4.1: A definition sketch for a particle at the ice-water interface.

4.2 Theory

4.2.1 The Chernov approach to the critical velocity

Researchers have investigated intermolecular forces acting between the particle, the solid, and the liquid that are responsible for particle rejection since the 70s [112]. As shown in Figure 4.1, the most important intermolecular forces in our system are the thermomolecular disjoining pressure that acts to repel the particle from the interface, and the viscous forces, associated with liquid flow in the premelted film that forms between the particle and the deformed interface, which tend to promote particle encapsulation within the growing solid [60]. These combined give a prediction for the critical velocity where the engulfment of the single particle will occur.

Thermomolecular force

As mentioned in Section 2.1.2, the thermomolecular pressure, arising due to the Van der Waals repulsion between the ice and the particle, premelts the ice and forms a thin layer of water between the particle and the ice. Furthermore, curvature induced premelting, caused by the Gibbs-Thomson effect, is also present. The combined contribution to the difference in pressure

is defined as

$$\Delta P = \gamma_{iw}\kappa + P_T, \tag{4.1}$$

where γ_{iw} is the ice-water surface energy and κ is the curvature, which combine to give the Laplace pressure. The second term is the thermomolecular pressure, P_T, for a premelted film. When the premelted liquid film separating the particle from the ice surface is much smaller than the particle radius, that is, the particle is close to the ice-water interface, the thermomolecular pressure can be written as

$$P_T = -\frac{A_{iwp}}{6\pi d^3}, \tag{4.2}$$

where A is the effective Hamaker constant for interactions between the particle and the ice with a water film intermediate, and is defined as $A_{iwp} \equiv A_{ip} + A_{ww} - A_{iw} - A_{wp}$, where i denotes ice, p denotes particle, and w denotes water. A more detailed derivation of this thermomolecular pressure is given in Section 5.2.1. According to Worster and Wettlaufer, the thickness of the premelted film d can be calculated as [113]:

$$d \approx d_0 + \frac{\frac{1}{2}\theta^2 R}{1 + \frac{3l^4}{d_0^4}}. \tag{4.3}$$

Here, d_0 is the minimum thickness of the liquid film, θ is the angle according to the normal of the interface toward the centre of the particle, R is the radius of the particle and l is a length scale given by $l^4 = \lambda^3 T_m/\nabla T$, with ∇T the imposed temperature gradient and $\lambda^3 = -A_{iwp}/6\pi\rho_i L_m$, where λ is a lengthscale term determined by the type of interaction, ρ_i is the density of the ice and L_m is the latent heat of solidification per unit mass. Within this approximation for d, Worster and Wettlaufer gave the approximated expression for thermomolecular force from integrating P_T over the interfacial surface [113]:

$$F_T \approx -\frac{AR}{6d_0^2}\left(1 + \frac{3l^4}{d_0^4}\right). \tag{4.4}$$

Here, we only consider the situation where $\theta \ll 1$, because the thermomolecular pressure reaches its maximum where the premelted film is thinnest and the particle surface is nearly parallel to the interface. In other words, as the film thickness at θ is much greater than the film thickness

immediately next to the particle (where θ is the smallest), this region near the base of the particle provides the largest contribution to the thermomolecular force.

Lubrication force

During the unidirectional freezing, there is a viscous drag force due to the constant flow in the thin film. This is responsible for feeding water to the region of the freezing interface [61]. As the film thickness between the particle and the ice front is much smaller than the particle radius, the flow in the premelted liquid film can be analysed using lubrication theory, as shown by Wettlaufer *et al.* [54]. The lubrication force is then calculated following Worster and Wettlaufer [113] by integrating the film pressure (resulting from the flow in the thin film) over the deformed surface of the ice-liquid interface:

$$F_\eta \approx -\frac{6\pi\eta R^2 V}{d_0}\left(1+\frac{3l^4}{d_0^4}\right)^2. \tag{4.5}$$

Here η is the viscosity of the liquid film. Note that the lubrication force increases in strength as the particle approaches the ice with a reduction of the film thickness and the ice-liquid interface becoming increasingly deformed.

Critical velocity

The motion of a particle near the ice-water interface is thus determined by a balance between the thermomolecular disjoining pressure that separates the particle from the ice surface, and the viscous drag. This is approximated by the lubrication force associated with fluid flow into the intervening premelted liquid film between the particle and the ice front. At equilibrium, the forces are balanced, so that $F_\eta + F_T = 0$, and an expression for the freezing velocity, V, in terms of the minimum thickness of the premelted layer, d_0, can be derived:

$$V = -\frac{A}{36\pi\eta R}\frac{d_0^3}{d_0^4+3l^4}. \tag{4.6}$$

Substituting in $l^4 = \lambda^3 T_m/\nabla T$ and $\lambda^3 = -A_{iwp}/6\pi\rho_i L_m$, we reach the critical freezing velocity, V_c, by differentiating V with respect to d_0 and taking the positive solution thus maximizing V:

$$V_c = -\frac{\sqrt{3}}{144\pi}\frac{A}{\eta R l} = -\frac{\sqrt{3}}{144\pi}\frac{A_{iwp}}{\eta R}\left(-\frac{6\pi\rho_i L_m \nabla T}{A_{iwp} T_m}\right)^{1/4}. \tag{4.7}$$

When the unidirectional freezing velocity is greater than the critical velocity, the particle becomes engulfed as the increasing lubrication force can no longer be balanced out by the thermomolecular force. This is because the supply of liquid is increasingly impeded by viscous effects as the particle approaches the interface [60]. Therefore the particle velocity decreases until the particle is engulfed by ice. Here we study the packing of particles at the interface, hence we want to make sure that the unidirectional freezing velocity is less than this critical velocity. Normally the Hamaker constant will have a magnitude of 10^{-20}, thus using $A_{iwp} = -10^{-20}\,\mathrm{J}$, η (at T_m) $= 2 \times 10^{-3}\,\mathrm{Pa\,s}$, $L_m = 334\,\mathrm{kJ\,kg^{-1}}$ and $R = 2.5\,\mu\mathrm{m}$, we obtain a critical velocity of $1.24\,\mu\mathrm{m\,s^{-1}}$. At this regime, where the particle reaches an equilibrium separation from the interface, its velocity remains constant and equal to the freezing velocity.

4.2.2 Osmotic pressure

Under a unidirectional freezing velocity smaller than the critical velocity, particles are rejected from the ice as the ice-water interface advances, causing the particle concentration in the suspension to slowly increase adjacent to the interface. This build-up of particles exerts an additional osmotic pressure onto the interface. When there are enough particles accumulated in front of the interface, the osmotic pressure of the particles is comparable to the maximum force for which the interface is capable of exerting [61], and the particles reach the maximum possible concentration. Any further increase in concentration will lead to a breakthrough event where the ice front breaks past the particles into the interstitial space instead of simply pushing the particles. This breakthrough only happens when the particle concentration is high enough that the resulting osmotic force from the suspension counters the capillary drag force exerted by the ice-water interface [98].

The relationship between the osmotic pressure of the suspension and the volume fraction of particles in the suspension (ϕ) can be modelled for well-dispersed systems with a modified

Carnahan-Starling equation [114, 115]

$$\Pi(\phi) = n_p k_B T \frac{1 + \phi + \phi^2 - \phi^3}{(\phi_m - \phi)^3}, \tag{4.8}$$

where ϕ_m is the volume fraction of particles at maximum packing, k_B is Boltzmann's constant, n_p is the number of particles per unit volume in the suspension. A detailed calculation of the evolution of osmotic pressure in our system over time is possible, but is tangential to the scope of this chapter.

4.2.3 Impurity induced premelting

In Chapter 3 we used the term 'instability' to describe the formation of ice-fingers. This can be used interchangeably with the term 'breakthrough' that we have posed here. Thus the theory discussed in Chapter 3 also applies in our experiments here, with the most relevant and important section being the impurity induced premelting and its relationship with the freezing velocity. Specifically, as the freezing velocity increases, the particles accumulate in front of the interface faster, which give rise to a higher concentration gradient of the particles. This in turn causes greater freezing point depression, which favours the onset of an unstable interface.

4.3 Experimental methods

4.3.1 Experimental set-up

The colloidal system used in this chapter is the 2.5 µm monodisperse TPM system described in Section 2.2.4. This size was measured using SEM, in which the sample is under vacuum, and consequently results in an underestimation of the size of the particle. In this chapter knowing the hydrodynamic diameter of the particle is crucial, so we also measured the size using dynamic light scattering (DLS), from which we obtain a diameter of 2.7 µm.

In ice-templating for freeze casting, typically a particle concentration ϕ = 5 - 40 % is used [116]. Here, ϕ = 12 % (mass fraction= 16 %) TPM solution was used to achieve a suitably thick colloidal layer in front of the ice in the experimental time window. UV glue sample cells, with a height approximately the particle diameter, were prepared as described in Section 2.2.5. The

sample cell was placed upon the freezing stage under the bright-field microscopy set-up described in Section 2.2.2.

We can independently vary the solidification front velocity (adjusted by the stepper motor) and the temperature gradient (established by the Peltier modules). The temperature of the cold plate was first set to $-40\,^{\circ}\mathrm{C}$ to initiate the formation of the ice. It was then adjusted to $-10\,^{\circ}\mathrm{C}$ for the cold plate and $10\,^{\circ}\mathrm{C}$ for the hot plate to achieve the desired temperature gradient, ∇T, of $10\,\mathrm{K\,mm^{-1}}$. The system was equilibrated at this temperature gradient for 30 min, after which the sample cell was moved at a prescribed speed through the steady temperature gradient controlled by the Linksys32 software. Data was recorded at 1 fps until the sample cell reached the end of the freezing set-up to ensure that the whole freezing process is captured.

With the $50\times$ objective, a typical image of the system is shown in Figure 4.2 (a). Here, the field of view is approximately $256\,\mu\mathrm{m} \times 256\,\mu\mathrm{m}$, which provides good single particle resolution while also providing a good overview of the system.

The high mass density of the TPM particles relative to the solvent results in their rapid sedimentation to the base of the cell. The gravitational height of the particle can be calculated as $h_g = 6k_BT/\pi\sigma^3 g\Delta\rho$, where g is the acceleration due to gravity and $\Delta\rho$ is the difference in mass density between particle and solvent. The diameter of $2.7\,\mu\mathrm{m}$ is used for σ and the density of $1.3\,\mathrm{g\,cm^{-3}}$ is used [71]. The calculated gravitational length is $0.124\,\mu\mathrm{m}$, which is about 4.6% of the particle size, resulting in negligible out of the plane fluctuations. As such, the system is described as quasi-two-dimensional.

4.3.2 Image analysis

Particle detection was achieved following the general procedure described in Section 2.2.6. The raw data extracted contained an array of coordinates, $(x_i,\ y_i)$, where i is the particle index produced for each frame.

The radial distribution function

The radial distribution function, $g(r) \equiv \frac{\rho(r)}{\rho}$, is a pairwise correlation function of relative position that can be measured directly from experiments. It gives the probability of finding a particle at a distance r away from a given reference particle relative to total density [117]. It is the simplest characterisation of the structure of a system that provides detailed description of structural correlations [118].

Here, ρ is the total number density of the system and can be calculated by N/A where N is the total number of particles and A is the area, and $\rho(r)$ is the local number density at a distance r. Here it is calculated by choosing a reference particle, $r = 0$, and finding all pairwise distances at this time. The number of particles in a bin between r and $r + dr$ is counted, and a histogram is constructed. This is repeated for all particles in the same instantaneous snapshot and the histograms are averaged. The radial distribution function tends to unity at large r as $\rho(r) \to \rho$. In this chapter the radial distribution function is calculated for experiments at each freezing velocity. Here we only analyse the part of the image where the particles are most dense to eliminate the error caused by locally particle-empty areas. The function is then averaged over 2000 frames to reduce noise. The results for this are presented in Section 4.4.2.

Voronoi tessellation and local density

A Voronoi diagram is a diagram where the plane is divided into regions according to a distance criterion, where each particle p_i has an associated Voronoi cell containing all the points closer to p_i than any other point p_j for $j \neq i$, as shown in Figure 4.2 (b) [119]. After we have identified the local area of the corresponding Voronoi cells, the local density can then be calculated by:

$$\phi = \frac{A_p}{A_k}, \tag{4.9}$$

where ϕ is the local density, A_p is the particle area $A_p = \pi\sigma^2/4$ (σ being the particle diameter) and A_k is the area of the Voronoi cell k. We then colour the Voronoi cells according to their local packing fraction (Figure 4.2 (c)). The results for this are presented in Section 4.4.3.

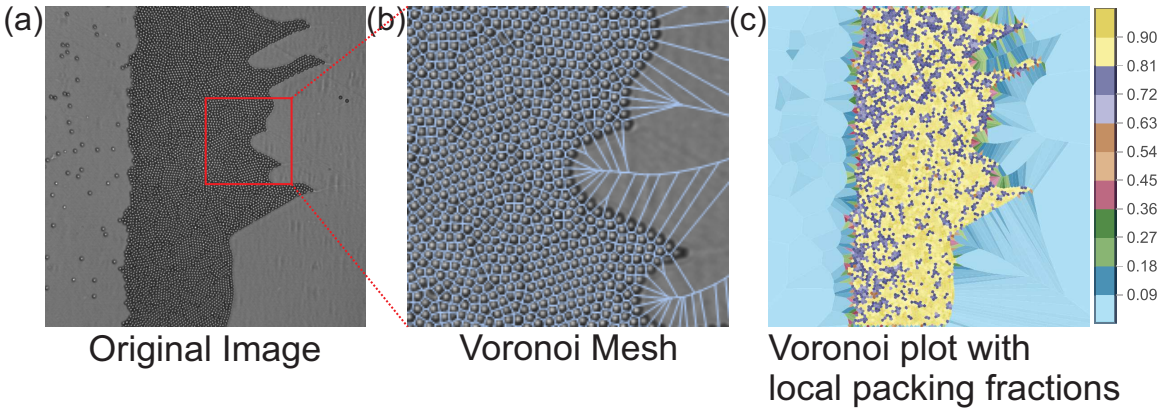


Figure 4.2: (a) The original microscopy image; (b) Overlay of the Voronoi mesh recreated from the extracted particle position and the original image; (c) Voronoi plot coloured by the value of particle area fraction within each Voronoi cells.

Local bond-orientational order analysis

To quantitatively analyse the crystallinity of the particles in front of the interface, the local bond-orientational order parameter, $\psi_6(\vec{r_j}, t)$, is calculated. For a particle j, located at $\vec{r_j}$ in two dimensions, $\psi_6(\vec{r_j}, t)$ can be calculated as:

$$\psi_6(\vec{r_j}, t) = \frac{1}{N_j(t)} \sum_{k=1}^{N_j(t)} e^{i6\Delta\theta_{jk}(t)}, \tag{4.10}$$

where $N_j(t)$ is the number of nearest neighbours, $\Delta\theta_{jk}$ is the angle between the vector connecting the central particle, j, with neighbouring particles, k, and a reference axis (here we use the x-direction) (figure 4.3(b)). The bond-orientational order quantifies the degree to which the neighbouring particles adopt a regular hexagonal position. We take the modulus of $\psi_6(\vec{r_j}, t)$ for each particle ($|\psi_6(\vec{r_j}, t)|$) to gain information about their local crystallinity. For perfect crystals, this modulus will be equal to 1, for a dense colloidal fluid it will around 0.4, and empirically it is defined that particles with modulus bigger than 0.7 is in a colloidal crystal [120, 121].
The local (bond) orientation of each particle j is then given by:

$$\theta_6(\vec{r_j}, t) = \frac{1}{6} arg(\psi_6(\vec{r_j}, t)), \tag{4.11}$$

and ranges from 0 to 60 degrees due to the hexagonal symmetry. The individual particles are then coloured according to their θ_6 value, as shown in Figure 4.3 (c). To remove noise at small distances for visualisation, the field θ_6 is smoothed by replacing $\theta_6(\vec{r_j}, t)$ with its average over the

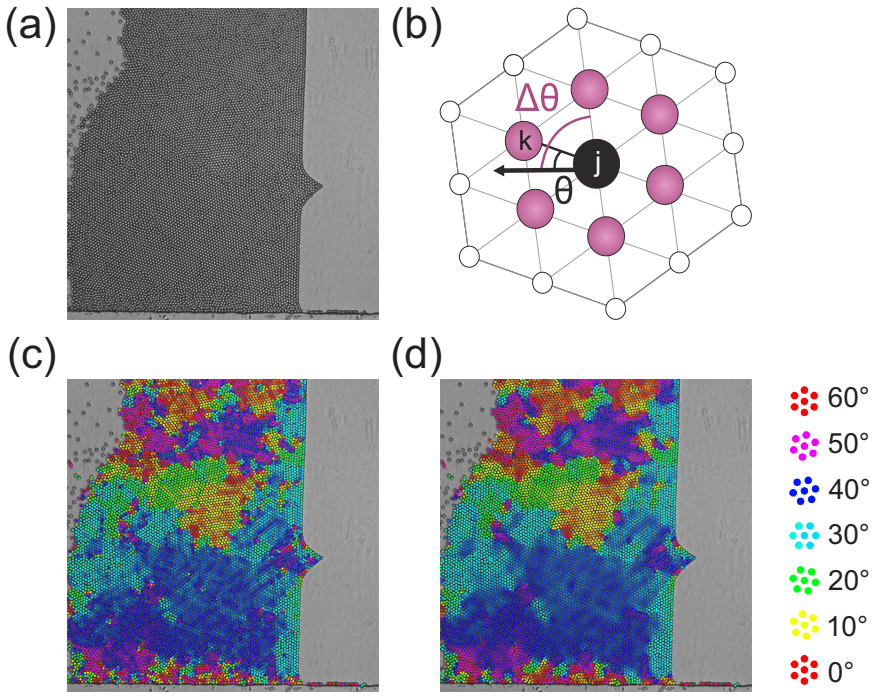


Figure 4.3: (a) An original microscopy image; (b) Delaunay triangulation showing a particle j (in black), with one of its nearest neighbours k. The angle between the bond vector joining the two and the x-axis is $\Delta\theta_{jk}$ and is used to calculate $\psi_6(\vec{r_j},t)$ and $\theta_6(\vec{r_j},t)$; (c) A plot of the raw orientation map $\theta_6(\vec{r_j},t)$ before smoothing, with all the particles coloured according to their $\theta_6(\vec{r_j},t)$ values; (d) Smoothing of the $\tilde{\theta_6}(\vec{r_j},t)$ field of each particle over two shells of nearest neighbours.

particles in the first two coordination shells (particles labelled in pink as well as in white circles in Figure 4.3 (b)). The smoothed local bond orientation is denoted as $\tilde{\theta_6}(\vec{r_j},t)$, see Figure 4.3 (d) for an illustration. Therefore by using this $\tilde{\theta_6}(\vec{r_j},t)$, we can easily visualise clusters with different orientations and the sharp transitions among the clusters.

We have also taken the average of the modulus of ψ_6 over all the particles present in the frame ($\langle|\psi_6(\vec{r_j},t)|\rangle$), to gain information about the overall crystallinity of the particle suspension. These results are discussed in Section 4.4.4.

4.4 Results

In this section we first present the results of the structure formed by the colloidal suspension under unidirectional freezing, at different freezing velocities (Section 4.4.1). Then we apply the various image analysis methods introduced in Section 4.3.1 in the following sections to study the resultant colloidal structures, to qualify the effect of the instabilities.

4.4.1 Solidification velocity

Previously we have looked at how different freezing velocities influence the ice-water interface instability. Here we look at the same experiment from a different angle. Figure 4.4 shows microscopy images capturing representative phenomena observed in the process of pulling the colloidal polycrystalline monolayer against the temperature gradient for evolution at different freezing velocities. The hot and cold plates are located on the left and right hand side respectively, outside the field of view, so the liquid is on the left hand side and the ice is on the right. The system is translated towards the cold side at the set pulling velocity to achieve controlled unidirectional freezing. The particles first build-up against the interface as in Figure 4.4 (i)s. The behaviour of the interface changes according to the freezing velocity.

At a solidification rate of V= $1\,\mu m\,s^{-1}$, a velocity lower than the single particle engulfment critical velocity, no breakthrough was observed and no long term perturbations could survive (Figure 4.4 (a)). Occasionally perturbations do occur (time (ii) in Figure 4.4 (a)), but they are translated towards the channel walls where they disappear. For this particular perturbation, it is translated towards the lower wall, as suggested by comparing Figure 4.4 (a, i and ii).

This constant unidirectional freezing leads to an increase in local particle density which consequently increases the osmotic pressure against the interface according to the Equation 4.8. By counting the number of particles present in each frame (Figure 4.5), we see that after 50 minutes of unidirectional translation (about 30% of the whole experiment) at $1\,\mu m\,s^{-1}$, the number of particles in front of the ice-water interface reaches a maximum of $\sim 10^4$ particles, which spans over about $200\,\mu m$ in the $x-$direction, corresponding to 75 layers of particles. This moment also corresponds to the highest pressure that an interface can endure. After this the system reduces the osmotic pressure by depositing particles along the side of the channel walls, a mechanism similar to the method by which perturbations disappear.

Figure 4.4 (b, c) shows the results when the system is translated at higher freezing velocities than the critical velocity (V = 2 - $3\,\mu m\,s^{-1}$). The experiments start with a stable and flat interface (Figure 4.4 (b, i & ii and c, i)), then with the building up of the particle layer, the interface became less stable with undulations forming (Figure 4.4 (b, iii & c, ii)), which then led to particle engulfments and instabilities (the rest of the snapshots in Figure 4.4 (b & c)).

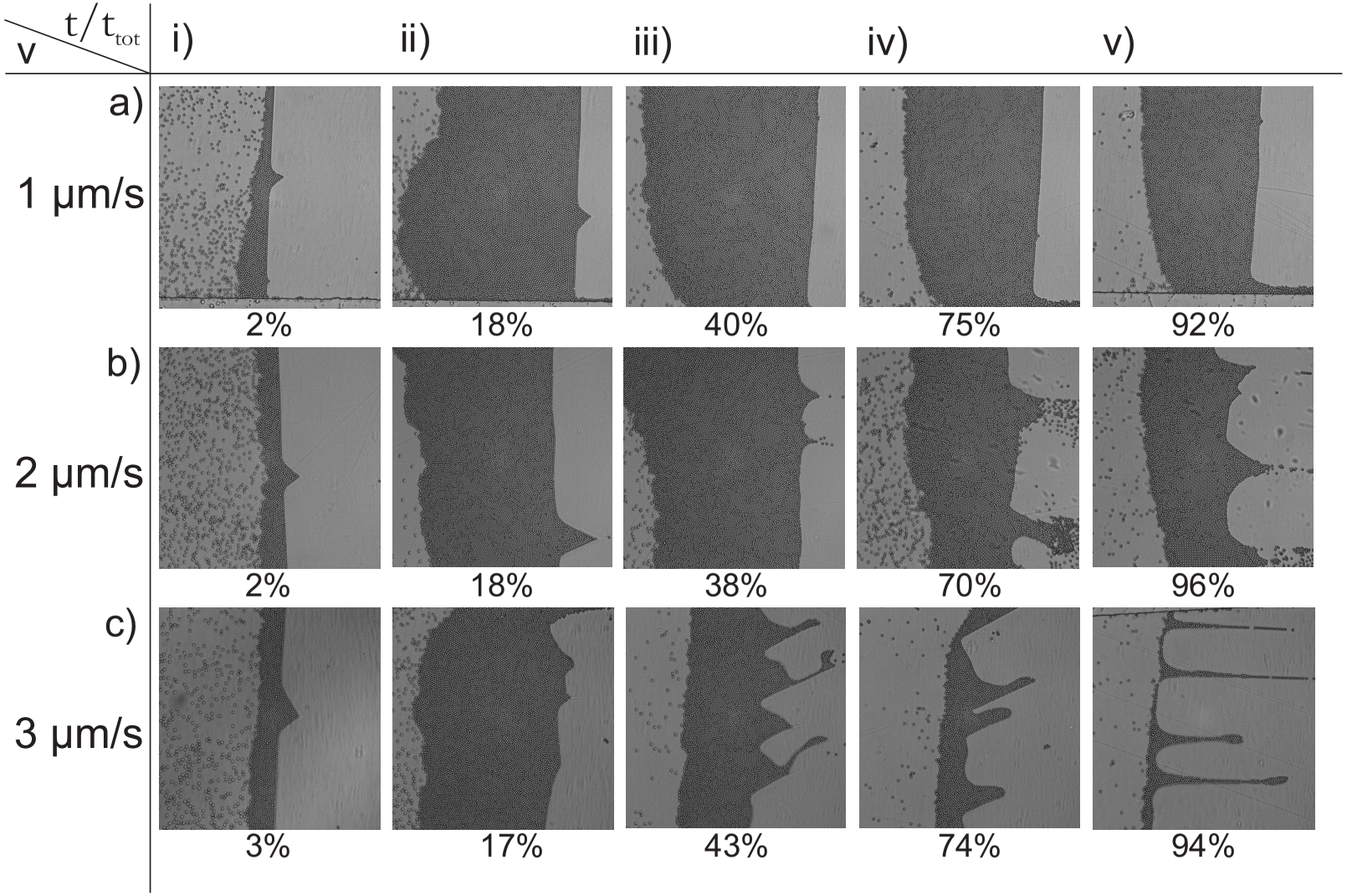


Figure 4.4: Snapshots from the experiments at different freezing velocity under the temperature gradient of $10\,\mathrm{K\,mm^{-1}}$. For each snapshot, the ice (cold plate) is on the right hand side and the liquid (hot plate) is on the left hand side.

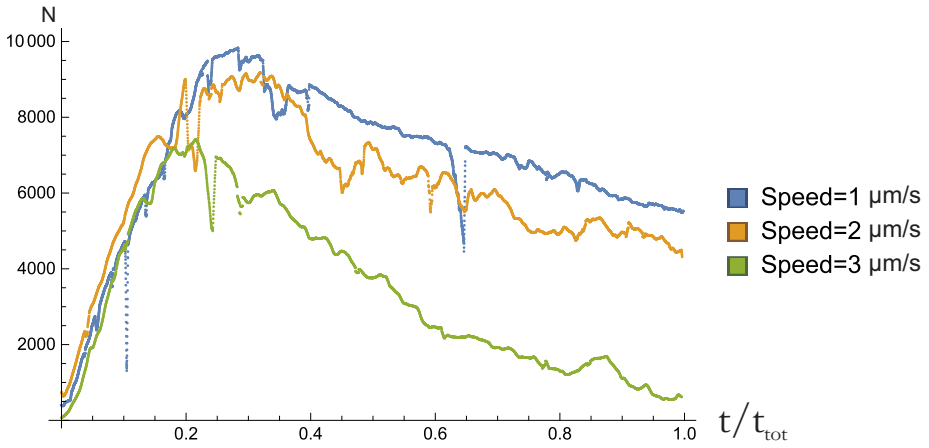


Figure 4.5: Number of particles detected in each frame for all three experiments at different freezing velocity. The x-axis is scaled according to the length of each experimental trial.

Therefore, we have successfully observed the difference when the system was frozen above or below the critical velocity. Here, instead of relating it back to the undercooling caused by the accumulation of particles (as we did in the previous chapter), we refer to the critical velocity and the lubrication force argument (Section 4.2.1). At $V > V_c$, the viscous drag is high and liquid cannot be supplied to the premelted film at a fast enough rate, which leads to the engulfment of the particles. The critical velocity was estimated for a single particle, and we propose that as the building up of the colloidal layers further impedes the replenishment rate of water (as it now needs to flow through an effectively porous material), the true critical velocity in bulk will be even smaller than the one estimated using Equation 4.7.

Another interesting phenomenon we have observed is that for higher freezing velocities where breakthrough events can happen, despite the fact that the number of particles decreases with the formation of ice fingers (Figure 4.5), the ice fingers do not break up to allow the system to relax back to the more stable planar interface. For the slowest freezing velocity, no breakthrough event occurs and the planar interface is retained throughout the freezing process. A similar process occurs as the number of particles in front of the interface is constantly decreasing. We hypothesise that this is due to the placement of the particles. Once the particles have established themselves in between ice fingers or between ice and glass wall, it is difficult to remove them in order to form the stable interface again.

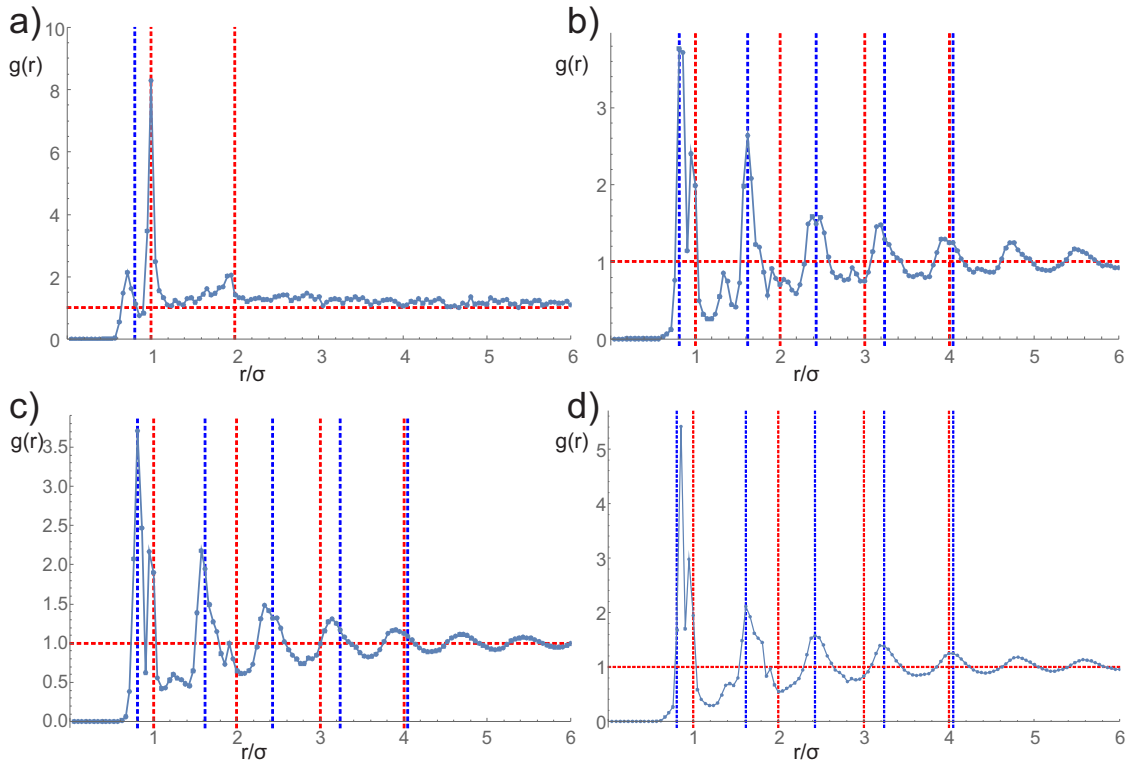


Figure 4.6: The radial distribution function $g(r)$ for the experimental systems. (a) Shows the $g(r)$ of an unfrozen sample; (b) The $g(r)$ of a sample frozen at V $=1\,\mu\mathrm{m\,s^{-1}}$; (c) The $g(r)$ of the sample frozen at V $=2\,\mu\mathrm{m\,s^{-1}}$; (d) The $g(r)$ of the sample frozen at V $=3\,\mu\mathrm{m\,s^{-1}}$. The red dashed lines show multiples r/σ, with σ being the true particle diameter, the blue lines show multiples of σ^*/σ, where σ^* is the projected particle diameter found experimentally. Note that we have only averaged the data over 150 frames instead of 2000 in (a).

4.4.2 Radial distribution function

This radial distribution function analysis was conducted to probe local order in the system for different freezing velocities as summarized in Figure 4.6. We first checked the radial distribution functions of particles in solution (Figure 4.6 (a)). It shows an initial sharp peak at approximately r/σ, where σ is the particle diameter, followed by a decay in peak height which tends to unity at large distances. This means there is no long range order in the system.

This measurement is then repeated for the three freezing experiments (Figure 4.6 (b - d)). Similarly, we observe a peak at r/σ, however, a much higher peak occurs at $r < \sigma$. This means particles can be found within a particle diameter range. By carefully analysing the experimental snapshots, we find this is out-of-plane buckling caused by the high osmotic pressure pushing the particle clusters against the ice-water interface, leading to the peak at $r < \sigma$. In other words, because the particles have a diameter of $2.7\,\mu\mathrm{m}$ and the sample cell has a thickness around

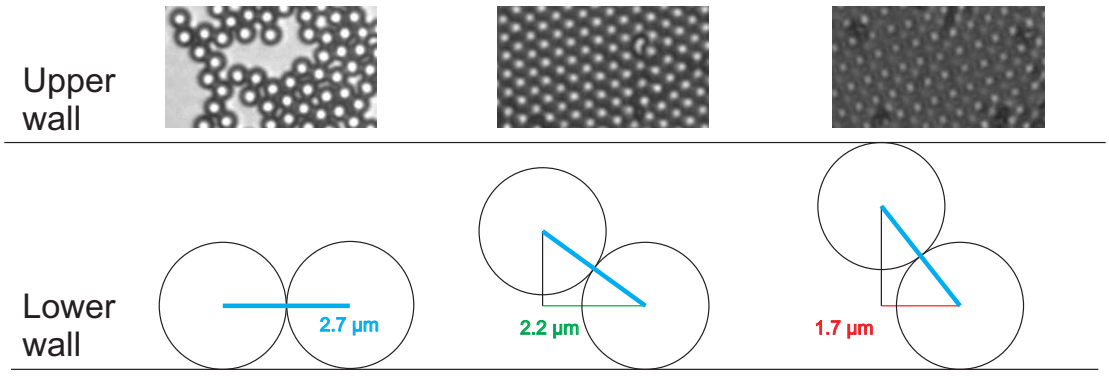


Figure 4.7: The buckling resulting from osmotic pressure. The left figure shows the particles in solution, without a strong osmotic pressure. The middle figure is the environment where most of the particles in the experiment feel some out-of-plane buckling resulting from the osmotic pressure. The right figure is the extreme case where the osmotic pressure pushes some particles towards the upper cover slip of the experimental cell.

4.7 µm, the osmotic pressure can force the system to adapt a new geometric configuration and push them upwards. This is shown in Figure 4.7. Here we have snapshots of three different configurations particles can take in our experimental system. The left figure represents the particles in solution (no freezing), without a strong osmotic pressure thus forming a 2D system. The middle figure represents the configuration most of the particles in the experiment adopt. There is some out-of-plane buckling due to the high osmotic pressure, resulting in the effective particle diameter of 2.2 µm. By using this σ^* of 2.2 µm and plot σ^*/σ in Figure 4.6, we see that this σ^* and its multiple corresponds to peaks from the frozen system much better. The rightmost figure in Figure 4.7 is the extreme case where the osmotic pressure pushes some particles against the upper cover slip of the experimental cell, as we can clearly observe with the square symmetry. This extreme case rarely happens in our system, we only find it at the edge of the cell. Therefore, in some of the later analysis we deliberately leave the edge out to avoid this bias.

4.4.3 Voronoi areas and local density analysis

As described in Section 4.3.2, we have divided each frame into individual Voronoi cells according to the particles' position, and the local density is calculated according to Equation 4.9. The corresponding snapshots coloured by the area fraction are shown in Figure 4.8.

A 2D hard sphere system undergoes a fluid-hexatic first order phase transition at around $\phi = 0.7$, and then a hexatic-crystal transition at $\phi = 0.73$ [33]. The local density reaches a maximum

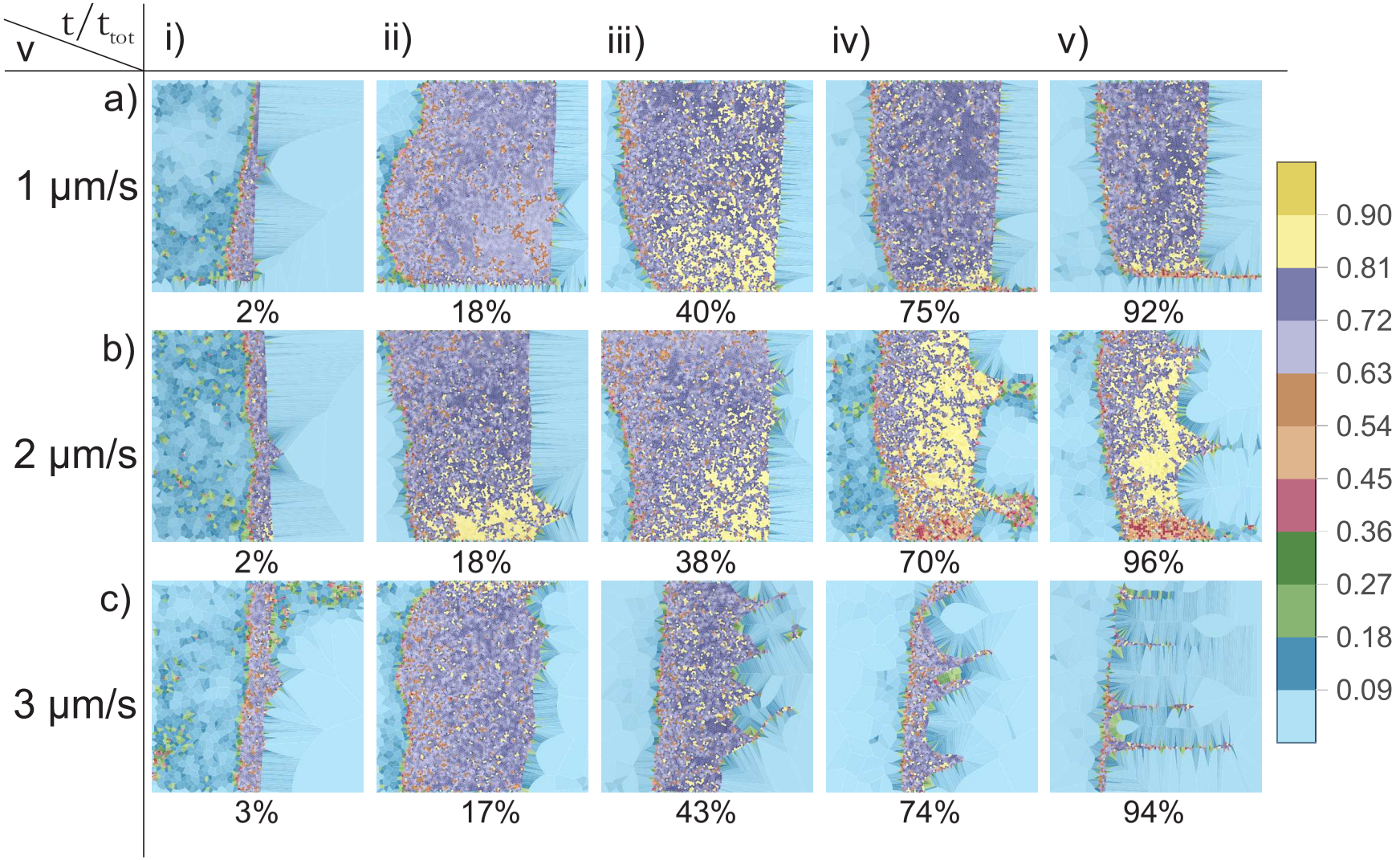


Figure 4.8: The same experimental snapshots as in Figure 4.4, coloured with their local density in their voronoi cells calculated using Equation 4.9.

packing fraction of $\phi = 0.907$ in a perfect crystal phase [33]. In our system, most of the particles are brought close together by the osmotic pressure, thus the particles in bulk have a local density ranging from 0.63 to 0.81 (Figure 4.8). There are areas with a relatively low area fraction, most of them located at the edge of the particle cluster. For some areas, the Voronoi density is less than 45% (Figure 4.8 (b,iii)), by comparing these with the original snapshot, we can see they are artefacts due to the out-of-plane particles, specifically the square symmetry arrangement of the particles at the edge of the channel.

4.4.4 Bond-orientational order analysis

As described in Section 4.3.2, we can quantify the degree to which the neighbouring particles adopt a regular hexagonal position by taking the modulus of bond-orientational order ($\psi_6(\vec{r_j}, t)$). We have coloured the experimental snapshots (Figure 4.4) according to their modulus of the local bond-orientational order ($|\psi_6(\vec{r_j}, t)|$) in Figure 4.9. We have also calculated the local orientation of each particle using Equation 4.11. Figure 4.10 shows the smoothed orientation field $\tilde{\theta_6}(\vec{r_j}, t)$ coloured onto experimental snapshots, where the colour of the particles corresponds to the local orientation of the crystallite defined by Equation 4.11.

From here, the interface between ordered and disordered grains can be easily located. The existence of a large single grained crystal was only observed in the early stages, at the slowest freezing velocity. Comparing this to the Voronoi tessellation in Figure 4.8 (a), we see that this grain has an area fraction of less than 81%. This relatively low local density gives the particles space to rearrange into a single crystal grain.

To see the overall crystallinity in each frame, we have taken the averaged argument of the local bond-orientational order, $\langle|\psi_6(\vec{r_j}, t)|\rangle$, and plotted it as a function of t/t_{tot} for the experiments at different freezing velocities as shown in Figure 4.11. As mentioned in Section 4.3.2, for perfect crystals, $|\psi_6(\vec{r_j}, t)|$ will equal to 1, for a dense colloid fluid, $|\psi_6(\vec{r_j}, t)|$ is around 0.4 and empirically we defined the particle having $|\psi_6(\vec{r_j}, t)| > 0.7$ to be a colloidal crystal [120, 121]. For all three freezing velocities, we see an initial growth in crystallinity, before it decreases and oscillates at a value lower than 0.7. Specifically, 0.65, 0.5, 0.6 for $v = 1\,\mu\mathrm{m\,s^{-1}}$, $2\,\mu\mathrm{m\,s^{-1}}$ and $3\,\mu\mathrm{m\,s^{-1}}$ respectively. These values indicate that the system has taken up a less ordered structure compare to a colloidal crystal, but is more structured compared to a dense colloid

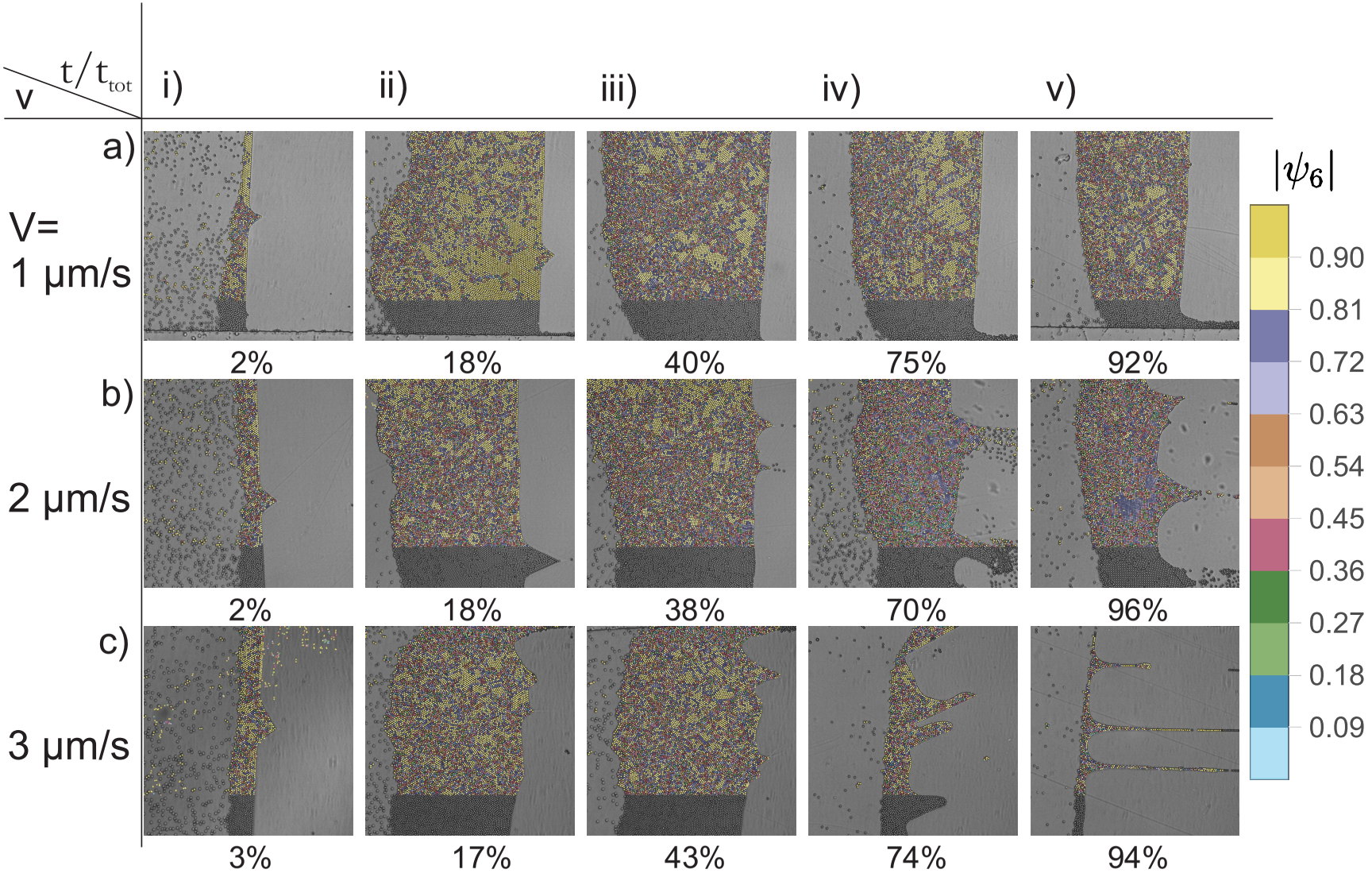


Figure 4.9: The same experimental snapshots as in Figure 4.4, coloured with the modulus of the corresponding $\psi_6(\vec{r_j}, t)$ value. The bottom of the original snapshot is left uncoloured.

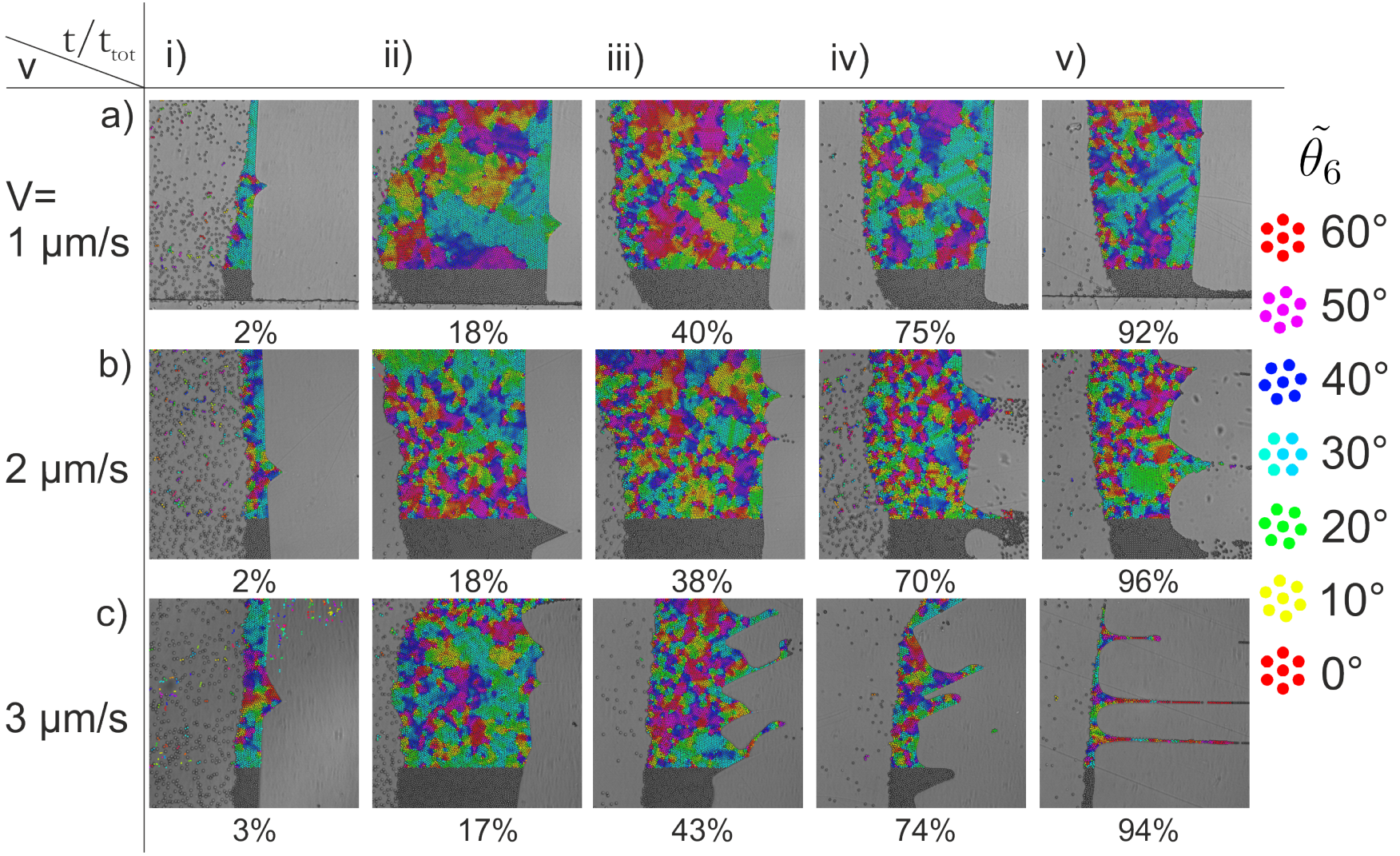


Figure 4.10: The same experimental snapshots as in Figure 4.4, coloured with the smoothed particle orientation. The bottom of the original snapshot is left uncoloured.

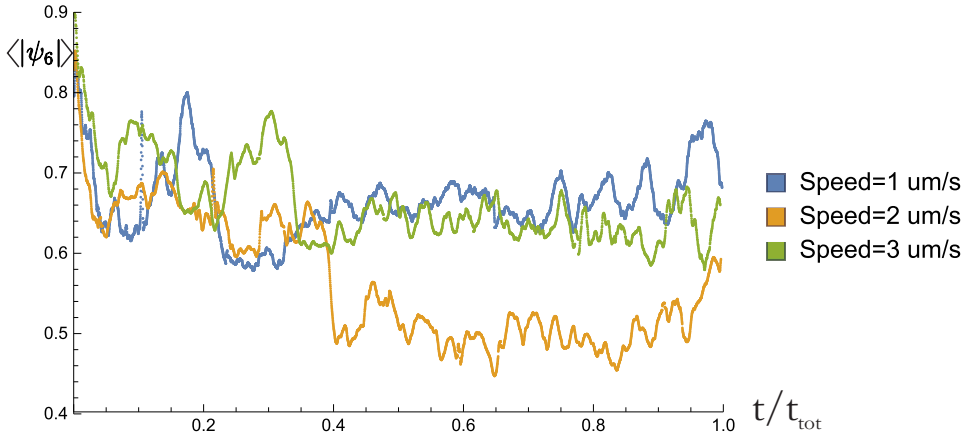


Figure 4.11: The smoothed modulus of the local bond-orientational order averaged for each frame, for all three experiments at different freezing velocity. The x-axis is scaled according to the length of each experimental trial.

fluid. Together with the plot of the number of particles in each frame (Figure 4.5), we can see that the breakdown of crystallinity does not necessarily correspond to the exact point where the system reaches the maximum number of particles (the highest osmotic pressure). We speculate this is related to the fact that the system constantly undergoes a dynamic rearranging process, and some time is needed for the system to adapt to the new environment.

Another initially surprising result from Figure 4.11 is that at $2\,\mu\mathrm{m\,s^{-1}}$, $\langle|\psi_6(\vec{r_j},t)|\rangle$ is lower compared to the structures resulting from the other two velocities. More experiments using freezing velocities around $2\,\mu\mathrm{m\,s^{-1}}$, and with different initial particle concentrations will be needed to fully understand this phenomenon. Currently, one possible explanation is related to the local density analysis. We can see that for $v = 2\,\mu\mathrm{m\,s^{-1}}$, there exist areas with a higher local density than 0.81 (marked in yellow in the Figure 4.8) that tend to have a lower local $|\psi_6(\vec{r_j},t)|$ (Figure 4.9), while such high density regions does not exist at other velocities. This might be due to the fact that for $v = 1\,\mu\mathrm{m\,s^{-1}}$, the freezing velocity is low enough that the particles have enough time to order themselves in each cluster. For $v = 3\,\mu\mathrm{m\,s^{-1}}$, the system is relaxed through the early onset of fully developed instabilities.

4.5 Conclusion and outlook

In this chapter we studied the behaviour of the particles in a quasi-2D sample cell frozen at a constant freezing velocity. The particles first build-up against the interface. Once the osmotic pressure is sufficiently large, the system will start to reduce the number of the particles in one

of the two different ways, according to the freezing velocity: the particles will either be expelled at the edge of the channel while retaining a linear ice-water interface, or a breakthrough event will happen as the interface breaks into the suspension's interstitial pores, and the number of the particles reduces as they are engulfed by the ice. This choice is dependent on the freezing speed of the system. We have shown that the critical velocity estimated for a single particle using Equation 4.7 can be used as an indication to predict whether a breakthrough event will happen at this velocity or not.

As mentioned in the introduction, one might expect this gradual increase in the particle density and compression of the colloidal fluid might result in similar results to that of a sedimented layer [33]. However, our findings are in agreement with MD simulations and X-ray scattering results [109,110], where they have also observed that the packing of silica nanoparticles induced by freezing was different from that obtained in liquid water. Spannuth *et al.* suggested the strong forcing of the particles by the growing ice may be responsible for the failure of applying standard structure factors [109].

Acknowledgments

Jenny Kuo is thanked for preliminary experiments. François Lavergne and Michael Mordan are thanked for psi-6 related discussions and coding. Josh Abbott and Joe Hutchinson are thanked for proof reading.

Chapter 5

Thermal Regelation of a Single Particle

ABSTRACT

In this chapter we study the movement of a single particle within ice at the temperature close to the melting temperature, in a well defined temperature gradient, at single particle level. We specifically look at how the engulfed particle moves in the ice, a process termed regelation. We experimentally extract the physical parameters that determine the interactions between ice and the silica particle during the thermal regelation process, and then calculate the thickness of the thin premelted layer around the particle. Finally, we look at the relationship between the particle size and the premelted layer thickness.

5.1 Introduction

Generally, an advancing ice front interacts with foreign particles in the liquid water according to two scenarios: particles are engulfed or rejected by the ice. However, an engulfed particle is not necessarily static within the ice. For example, dust particles that are trapped in the polar ice sheets are viewed as indicators of past climate conditions [122], but this is not always an accurate indicator, as the particles can migrate into ice of a different age from their deposition due to thermal regelation [46, 123]. A similar and closely related problem is pressure-induced regelation, wherein a weighted wire is pulled through a block of ice [113].

Both thermal and pressure-induced regelation can be explained in terms of premelting [113], where a liquid film disjoins a solid surface from the ice surface, at temperatures below the bulk freezing point, as a result of the competition between a reduction of interfacial free energy and the expense of maintaining a layer of undercooled liquid [21]. The premelted layer is the thin layer of water that exists between the ice and another solid surface (here a particle), at a temperature lower than the bulk temperature. This solid surface can also be another ice grain, which explains the stickiness of snow, specifically, the joining and subsequent freezing of the premelted layers surrounding different ice grains [124]. This thin premelted film is also attributed to the preferential wetting of the solid material by water, rather than ice. Similar liquidity can be found in many other phenomena such as thundercloud electrification [50] and debris entrainment by cold-based glaciers [125].

The thickness of the premelted layer is dependent on temperature: it gets larger as the temperature is increased [113]. Therefore, if a temperature gradient exists in the system, there will be difference in the premelted layers thickness. Consequently a pressure gradient is also present, and water must flow along the layer from warm to cold. This has been proven by an elegant experiment by Wilen and Dash, who showed how water can flow along a temperature gradient in the premelted layer between ice and a flexible membrane [126]. Because of the existence of the premelted layer, water flowed in between the ice and the membrane. The fresh water continuously froze onto the ice, while the premelted layer remained at its equilibrium thickness. The membrane changed shape because of this constant input of water. Similarly, in order to reject a particle from the ice, water must be able to freeze onto the ice-water interface between the particle and the ice. This is fulfilled by the existence of the premelted layer.

In this chapter we are interested in this thermal regelation process, where trapped particles in

ice migrate along the temperature gradient [127]. Colloidal particles are particularly suited as the model system for thermal regelation, as their size makes them observable and trackable in real time using optical microscopy [26]. Previously, experimentalists were more interested in the phenomenon of the particle engulfment rather than the regelation event [30]. Additionally, polydisperse colloidal particles were typically used in these systems, making analysis more difficult [127]. Meanwhile, theoreticians have mainly focused on the forces on the particle in front of the ice-water interface [46, 60, 62], rather than predicting the movement of particles after they are engulfed in ice. Here, we carry out our experiments at single particle resolution, which made observing and tracking individual particles and therefore their behaviour in the ice possible.
We begin this chapter by outlining the theory of premelting and how it is relevant to the ice-particle interactions in Section 5.2. Then the experimental work carried out is described in Section 5.3, before the results are given in Section 5.4 and discussed with reference to the related theories. This chapter finishes with a brief conclusion of our findings in Section 5.5.

5.2 Theory

In this chapter we outline and explain the underlying theories behind regelation. Here, the theory is established for the ideal case of a planar ice-water interface interacting with a particle in a suspension, away from any walls. In other words it is the interaction of a particle with ice, close to the bulk melting temperature, under a temperature gradient. We start by revisiting the concept of premelting in our system (Section 5.2.1). We then present an explanation of the thermal regelation of particles out of ice grains under a temperature gradient and discuss its relationship to the premelting (Section 5.2.2).

5.2.1 Premelting

As discussed in Section 2.1.2, there are three different effects that will induce premelting: curvature induced premelting (Gibbs-Thomson effect), interfacial premelting and impurity induced premelting. For our experimental set-up, premelting mainly arises from the effect of interfacial premelting, as the other two effects are minimised in the following ways:
Curvature induced premelting is minimised by using a colloidal dispersion at very low parti-

cle concentration. This eliminates the interstitial pores formed at high particle concentrations, which contributes most to the Gibbs-Thomson effect given the pores' small radius. Impurity induced premelting was minimised by using colloidal particles which were washed thoroughly before redispersing them in deionised water in a very low concentration. The resulting colloidal suspension is very pure, as the undercooling for this solution persists until $-40\,^{\circ}\mathrm{C}$.

A repulsive intermolecular force acts between the ice and the particle, resulting in interfacial premelting. Premelted water exists at temperatures below the bulk melting temperature, T_m. This shift in the freezing temperature is known as the interfacial undercooling ΔT_{int} [113]:

$$\Delta T_{int} = \frac{T_m}{L_m \rho_i} P_T(d), \tag{5.1}$$

where L_m is the latent heat of water, ρ_i is the density of ice, P_T is the 'disjoining pressure', the intermolecular interaction per unit area, with which the solid and the substrate repel each other. It is also known as the 'thermomolecular pressure'. The dependence of P_T on the film thickness d is determined by the type of intermolecular interactions of the system [46].

Here we consider the Van der Waals forces. Recall that for two molecules in free space, separated by a distance r, the interaction is:

$$U = -\frac{C}{r^6}, \tag{5.2}$$

where C is a constant and proportional to the polarizabilities and ionization potentials of the two molecules. Now considering two surfaces, where each surface is a semi-infinite solid, the interaction between all the molecules in a slice of slab 1 (with density ρ_1) at a distance D from slab 2 (with density ρ_2) is [128],

$$U = -\int_D^\infty \frac{\pi C \rho_1 \rho_2}{6x^3} A dx = -\frac{\pi C \rho_1 \rho_2 A}{12 D^2}. \tag{5.3}$$

Here, $\rho_1 A dx$ is the number of molecules found in a slice of thickness dx of slab 1, at a distance x from slab 2, and D is the distance of the vacuum between the two slabs. We then introduce the Hamaker constant, A_{12}, and obtain the interaction energy per unit area, defined as:

$$U = -\frac{A_{12}}{12\pi D^2}, \tag{5.4}$$

such that $A_{12} = \pi^2 C \rho_1 \rho_2$. A negative value for the Hamaker constant corresponds to a repulsive disjoining pressure.

We now reconsider the force between the ice and particle surfaces, separated by a premelted layer of thickness d. The driving force repelling the particle from the solid phase is commonly related to the non-retarded van der Waals forces when the distance between particle and solid phase is small compared to the particle radius [129]. Thus the pressure is given by [113]:

$$P_T = -\frac{A_{iwp}}{6\pi d^3}. \tag{5.5}$$

The relevant Hamaker constant, A_{iwp}, for ice interacting with a particle in the medium of water, is defined as $A_{iwp} \equiv A_{ip} + A_{ww} - A_{iw} - A_{pw}$, where i denotes ice, p denotes particle, and w denotes water. From here, we can see that as long as A_{iwp} is negative, there is a repulsive disjoining pressure between the particle and the ice, which gives rise to a stable liquid film, i.e. interfacial premelting [113, 130]. Note that changing the conditions in the system may lead to other intermolecular forces, and therefore different types of disjoining pressures. For example, dissolved ionic impurities would cause double layer repulsions [58,130], although these are typically not considered.

By combining Equations 5.1 and Equations 5.5, the premelted layer thickness becomes,

$$d = \left(-\frac{T_m}{L_m \rho_i}\frac{A_{iwp}}{6\pi}\right)^{\frac{1}{3}} (\Delta T_{int})^{-\frac{1}{3}} = \lambda \left(\frac{T_m - T}{T_m}\right)^{-\frac{1}{3}}, \tag{5.6}$$

where $\lambda^3 = -A_{iwp}/6\pi\rho_i L_m$. Interfacial premelting is highly relevant in the interaction of particles with an advancing ice front, as illustrated in Figure 5.1. Equation 5.6 indicates that the layer thickness decreases as the temperature is reduced, shown schematically as $d_1 > d_2$ in Figure 5.1. This has important consequences for particles immersed in ice as this results in a pressure difference in the premelted film via Equation 5.5, which causes the flow of water within the film, and thus movement of the particle. In the following section we will discuss how the premelted film can cause movement of a particle through ice along a temperature gradient, known as thermal regelation.

Equation 5.6 can be generalised for premelting resulted from other forces to the following equation:

$$d = \lambda \left(\frac{\Delta T_{int}}{T_m}\right)^{(-1/\nu)}, \tag{5.7}$$

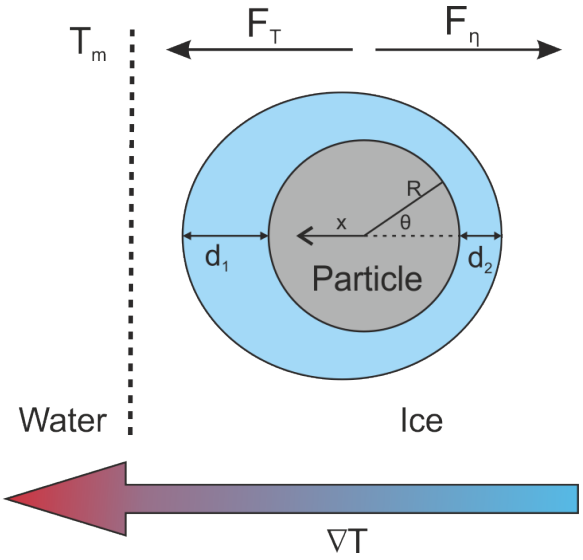


Figure 5.1: Schematic for a particle being engulfed by ice. The direction of the temperature gradient from cold to warm, ∇T , is indicated, as well as the directions of the thermomolecular and viscous forces, F_T and F_η, and the position of the bulk melting temperature, T_m (dotted line). Regions where premelted water is present are coloured blue, and the thickness of the premelted layers are labelled as d_1 and d_2.

where the constants λ and ν are physical parameters determined by the type and range of interactions between the particle and the ice [54].

5.2.2 Thermal regelation of particles in ice

The intermolecular forces that cause premelting also exist as a repulsive force between the solid and a foreign substrate. In the previous chapter we have demonstrated the effect of the thermomolecular force on a particle when the particle is in water and close to the interface (Section 4.2.1). Similarly, when the particle is fully engulfed in ice, the thermomolecular force on the particle can still be calculated by integrating the disjoining pressure over the whole particle surface. Here we follow the approach of Worster and Wettlaufer [113].

Figure 5.1 is a schematic diagram showing a particle of radius R surrounded by ice. We assume that the thermal conductivities of the particle, ice and water are equal, and the latent heat released and absorbed as the sphere migrates is negligible [113]. The temperature is then given everywhere by:

$$T = T_0 + \nabla T x = T_0 - \nabla T R \cos\theta, \tag{5.8}$$

where T_0 is the temperature at the centre of the sphere, x is measured from the centre towards the hot side, and θ is the polar angle measured from the horizontal. Therefore, if the dominant intermolecular interactions are van der Waals ($\nu = 3$), the thickness of the premelted film within this temperature field can be calculated from Equation 5.6 and 5.8 as:

$$d = \lambda T_m^{1/3}(T_m - T_0 + \nabla T R\cos\theta)^{-1/3}. \tag{5.9}$$

Together with Equation 5.5, the thermomolecular pressure within this film is

$$P_T = \frac{\rho_i L_m}{T_m}(T_m - T_0 + \nabla T R\cos\theta). \tag{5.10}$$

This gives a net thermomolecular force, acting in the direction of the temperature gradient, from cold to warm:

$$F_T = \frac{4\pi R^3}{3}\frac{\rho_i L_m}{T_m}\nabla T. \tag{5.11}$$

With the particle being pushed out of the ice by the thermomolecular force, there is a lubrication force acting in the opposite direction as the particle moving through the thin premelted film around it. Worster and Wettlaufer have concluded that the lubrication force is given by [113]:

$$F_\eta = -\frac{4\pi R^3}{3}\frac{6\eta R|V|}{\lambda^3}\frac{\Delta T_{int}}{T_m}. \tag{5.12}$$

Here $|V|$ is the flow velocity, which is numerically equal to the velocity of the particle which migrates along the temperature gradient, ∇T, and η is the viscosity of water. The rate at which the particle is able to move depends on this viscous flow in the premelted film, which itself depends on the thickness and geometry of the premelted film.

As we assume there is no external force on the particle, the net thermomolecular force must be balanced solely by the lubrication forces, thus $F_T + F_\eta = 0$. From this, the regelation velocity can be calculated:

$$|V| = \frac{L_m\rho_i}{6\eta R}d^3\frac{\nabla T}{T_m}. \tag{5.13}$$

Using Equation 5.7 and $\nu = 3$, this can be generalised into the following form

$$|V| = \frac{L_m \rho_i}{6\eta R} \lambda^3 \left(\frac{\nabla T}{T_m} \right)^{1-3/\nu} \Delta x^{-3/\nu}. \tag{5.14}$$

Hence, we find an expression for $|V|$ as a function of d. As the particle approaches the interface (moves up ∇T), ΔT decreases, which leads to an increase in d (Equation 5.7). Here, in Equation 5.13, we also see the relationship where $|V|$ is proportional to d^3, thus this increase of the premelted film thickness causes the particle to accelerate out of the ice.

In our experiment we can separately track the position of a particle and the interface, thus we can calculate $|V|$ and ΔT accordingly. This provides a method to determine the type of the interaction, and to measure the premelted film thickness using Equation 5.7. Wettlaufer *et al.* developed a theory covering premelting dynamics for all power law forces, suggesting that for $\nu = 3, \lambda \approx 1.4$ Å, and for $\nu = 2, \lambda \approx 0.2$ Å [54]. More recently, Peppin *et al.* [131] have analysed the regelation data of glass beads from Romkens and Miller [127], and found ν and λ to be 2 and 3.6 Å respectively, indicating the force is a long range electrostatic interaction.

5.3 Experimental methods

5.3.1 Particle engulfment

In order to investigate regelation events, we first need to have the particles engulfed by the ice. Rempel and Worster predicted that above the critical velocity V_c, the total displacement of the particle is only a fraction of a particle radius, suggesting that a particle must be engulfed immediately at the critical velocity [60]. As such, we initially tried to achieve particle engulfment by moving the particles at a speed V slightly above the critical velocity V_c, calculated using Equation 4.7. This freezing velocity is kept as close to the V_c as possible, so that once the particles are engulfed and we stop the translational motor, the interface will decelerate to its equilibrium position within a short distance, which secures the particles' starting point for regelation remains in the field of view. However, Lipp and Korber suggested that the engulfment process does not necessarily happen instantaneously. Based on their statistical analysis of the distribution of pushing times, they found that 50% of particles were pushed for 30-40 s at critical

velocity before they were engulfed. In other words, the critical velocity for the engulfment to occur is difficult to define because particles are engulfed over a range of V instead of at a single velocity V_c [29, 30, 129]. In our set-up, we observe a similar hysteresis.

We can use a much higher freezing velocity to ensure the engulfment of the particles, however this requires a larger distance for the system to decelerate, making it more difficult to position the particles at a good distance away to allow for the observation of the regelation events. Furthermore, using this method, the V_c will change even within one set of experiments. This is because as the freezing process continues within the sample cell, impurities such as salt build up at the front of the ice-water interface, strengthening the solute effect and the premelting of the interface, making engulfment easier in later experiments. This also makes it harder to reproduce the engulfment event from one experiment to another. Therefore, we have developed a new method (Figure 5.2) where we untangle the regelation without involving the critical velocity.

Here we use the TPM particles at three different diameters: 1.8 µm, 2.5 µm and 3.2 µm, synthesized as described in Chapter 2.2.4. As shown in Figure 5.2 (a), from a solution of particles, we first nucleate the ice by lowering the cold plate to −40 °C. After we have confirmed the formation of ice through bright-field images, the cold plate was heated to achieve a ∇T of $10\,\mathrm{K\,mm^{-1}}$ (which corresponds to −10 °C as the hot plate is set constantly at 10 °C). At the same time, the sample was moved towards the cold plate at a low translational velocity ($1\,\mu\mathrm{m\,s^{-1}}$) for 5 minutes to obtain a stable, flat interface (Figure 5.2 (b)). This step not only helps us to locate the position of the interface in the field of view at the same temperature gradient, but also collects multiple particles at the interface to improve the statistics. After this, the cold plate is rapidly lowered to a temperature of −20 °C at a rate of $30\,^{\circ}\mathrm{C\,min^{-1}}$. This high temperature gradient ensures rapid freezing, and additionally the ice-water interface follows the new temperature gradient, thus shifts to the left of the field of view, creating a space where regelation events can occur. The growth of ice pushes particles for a distance, before engulfing the particles (Figure 5.2 (c)). This step also introduces stochasticity into the system, as it moves the particles to different distances away from the interface, i.e. different starting positions for the regelation. The size of the regelation zone and the starting position of the particles are adjusted by translating the system slowly at $1\,\mu\mathrm{m\,s^{-1}}$ towards the cold plate (Figure 5.2 (d)).

Then the temperature of the cold plate was adjusted to reestablish $\nabla T = 10\,\mathrm{K\,mm^{-1}}$, and the interface slowly moved back towards its equilibrium position at this temperature gradient. Measurements begun just before the interface arrives in its original position to allow the whole

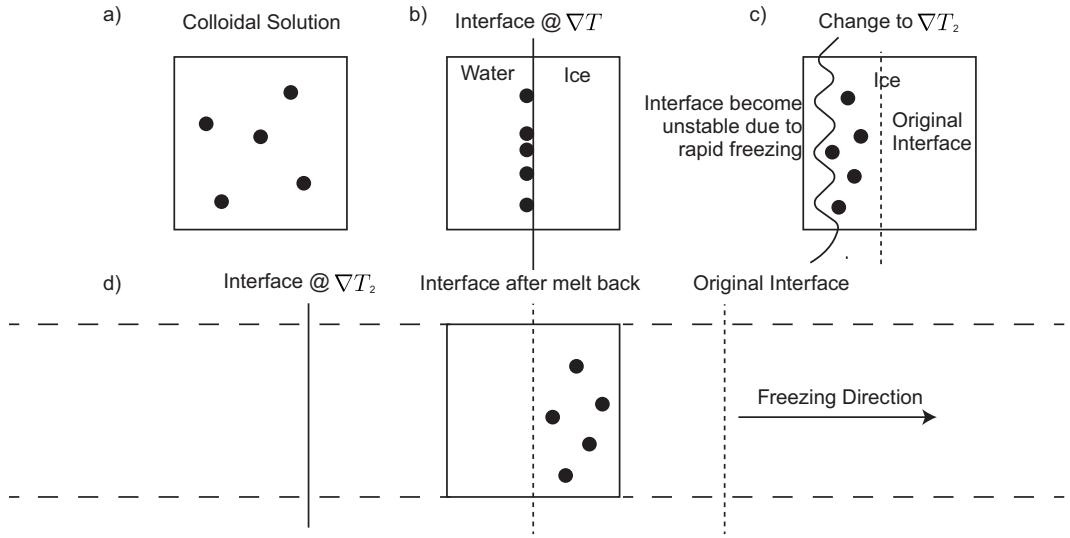


Figure 5.2: (a) Unfrozen sample; (b) After initial nucleation and stabilisation, a planar interface was obtained at a $\nabla T = 10\,\mathrm{K\,mm^{-1}}$; (c) Upon rapid freezing, the interface became unstable, and pushed the particles forward for a distance before engulfing them; (d) As the field of view was unchanged, when ∇T was adjusted back to $10\,\mathrm{K\,mm^{-1}}$, the ice-water interface reappeared at the same position in (b) relative to the camera. The sample was translated towards the cold plate such that an ideal distance between the particles and the interface was achieved, before ∇T was adjusted and measurements began.

regelation events to be recorded. After all the regelation events in the field of view had been recorded, we simply translated the sample slowly to move the interface until we achieve a new blank slate for the next experiment.

5.3.2 Image analysis

The location of the particle and the interface are identified separately for each time frame. All the related image analysis was achieved with Mathematica.

Particle tracking

Particle detection was accomplished using the method described in Section 2.2.6. In short, for a typical image of colloidal particles where the particles have a central bright spot and a dark outer ring, a binary image was created by replacing all values above a globally determined threshold with 1 and others with 0, thus only leaving the dark ring in the image. Then the foreground image components were selected according to their sizes and elongation, ruling out potential noise from the binary image. This also gives particle locations as pixel coordinates in x and y.

After the particle positions in each frame were determined, a tracking program based on the nearest locations was used. A threshold maximum distance, up to which a particle could move from its position in the previous frame, was set. A trajectory required a minimum number of steps to be considered a valid particle. Particles that fit this criteria were given an ID, and an individual particle's trajectory $((x_p, y_p), t)$ could be plotted, where the time, t, is the frame number multiplied by the time interval per frame.

Interface identification

In optical microscopy, ice and water have nearly identical appearances because the refractive indices of ice and water are close in value. However, this difference, despite being small, still results in the scattering of light, which makes the interface easy to identify. The steps taken to find the position of the interface are shown in Figure 5.3. From the original image, a binary image was again created, but using a different threshold (usually higher than the threshold used for identifying the particle), to retain as much information about the interface as possible. This resulted in a binarised image in which the interface is black and background is white (Figure 5.3 (b)). From this, a negative image was created (Figure 5.3 (c)), making the foreground 'objects' white, thus suitable for the built-in 'SelectComponents' function in Mathematica. After this, the foreground image components were selected according to their 'sizes', 'elongation' and 'orientation'. The resultant detected interface is shown in Figure 5.3 (d). Information about the interface might be lost during the processing, and the raw detected interface is potentially noisy. Therefore a straight line was fitted to the detected interface (Figure 5.3 (e)), and this line function was used for calculations.

5.4 Results and discussion

Here we present and discuss the results of our experiments. This section is divided into a qualitative description of the rejection phenomenon (Section 5.4.1 and Section 5.4.2) and the quantitative results of the thermal regelation of particles in ice (Section 5.4.3).

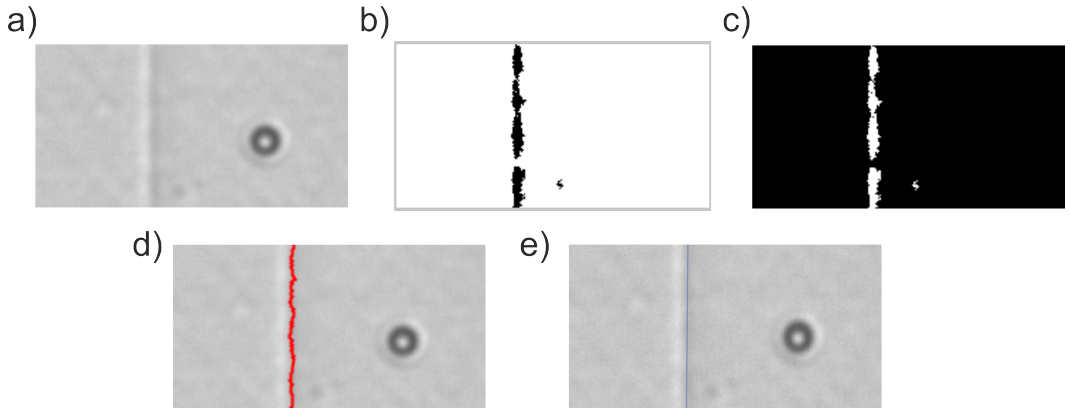


Figure 5.3: (a) Original image; (b) Binarised image, a grey outline was added at the back to help visualisation; (c) Negative image of (b); (d) Detected interface; (e) Interface fitted with a straight line.

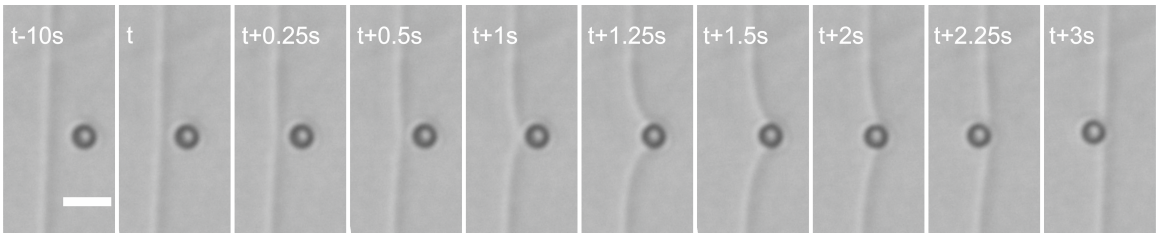


Figure 5.4: Typical snapshots from a regelation experiment (with R = 2.5 µm and ∇T = 10 K mm^{-1}). Here we only selected the snapshots around the time t where the particle crosses the interface. The scale bar corresponds to 5 µm.

5.4.1 Qualitative observations of regelation

Figure 5.4 shows 9 sequential snapshots taken from a typical regelation experiment with one particle exiting the ice-water interface. The first thing one can observe is that the interface is curved toward the particle when they are sufficiently close to each other. Rempel and Worster have predicted that when the particle is more insulating than the environment, the temperature field is distorted near the particle and the bulk melting temperature isotherm will curve towards the particle [60]. In our system, as TPM is a silica based particle, we assume it has a similar thermal conductivity to silica (1.2 W m^{-1} K^{-1}), while for bulk ice, the thermal conductivity is about 2 W m^{-1} K^{-1}. The prediction based on the difference in thermal conductivities is thus consistent with our observation.

Particles in our system are also observed to accelerate out of the ice along the temperature gradient. The event of exiting itself happened within 3 seconds, during which the particle moves about 4 µm. In contrast, in the 10 seconds before the exiting event, the particle moved less than 1 µm. We can visualise this acceleration process clearly by plotting the difference between the

position of the particle and the interface, which we will discuss in the next section.

5.4.2 Motion of particles relative to the ice-water interface

The particle trajectory is recorded using the particle tracking method described in Section 5.3.2 and is plotted on an experimental snapshot in Figure 5.5 (a). Here we can clearly see that the particle only moves in the x-direction (perpendicular to the interface) during the regelation process due to the unidirectional thermomolecular force. Once the particle has crossed the interface and entered the water phase, it starts to move in the y-direction as well, as it starts to undergo Brownian motion. The characteristic unidirectional movement within ice enables us to simplify our velocity analysis of regelation by only considering the position difference in the x-direction, $\Delta x = x_p - \bar{x_i}$, where x_p is the x-position of the particle, and $\bar{x_i}$ is the averaged position of the interface throughout the whole experiment.

Here we use the averaged position of the interface because the interface fluctuates in the x-direction throughout the experiment. We plot the x-position of the interface in Figure 5.5 (b), where we can see the interface first approaches its thermodynamically preferred equilibrium position quickly in response to the change of the temperature gradient, and then starts fluctuating around this equilibrium position. These fluctuations make the later calculations based on Δx more complicated. If we use the instantaneous position of the interface, the whole trajectory of the particle movement in x-direction become very noisy as shown in Figure 5.5 (c). Here, we choose to use the average position of the interface ($\bar{x_i}$) to calculate the Δx. The positions of the interface used to calculate the average position are shown in red in Figure 5.5 (b). We do not have a set of rules to choose the exact position of the start-point and endpoint as the choice does not drastically affect the final outcome. Any choice is valid as long as the start-point is after the interface has reached equilibrium and the end-point is after the particle has exited the ice. The resulting Δx vs t data is plotted in Figure 5.5 (d).

Taking a closer look at Figure 5.5 (d), the first point to note is that the curvature of the line corroborates the theory detailed in Section 5.2.2, which predicts that the particle velocity will increase as the particle moves up the temperature gradient towards lower undercooling. Secondly, when the particle passes into the water phase, it starts to exhibit Brownian motion, which is reflected by the fluctuations in Δx. Note that according to our definition, particles leave the ice only when Δx become less than zero. Looking at Figure 5.4, $\Delta x < 0$ corresponds to the

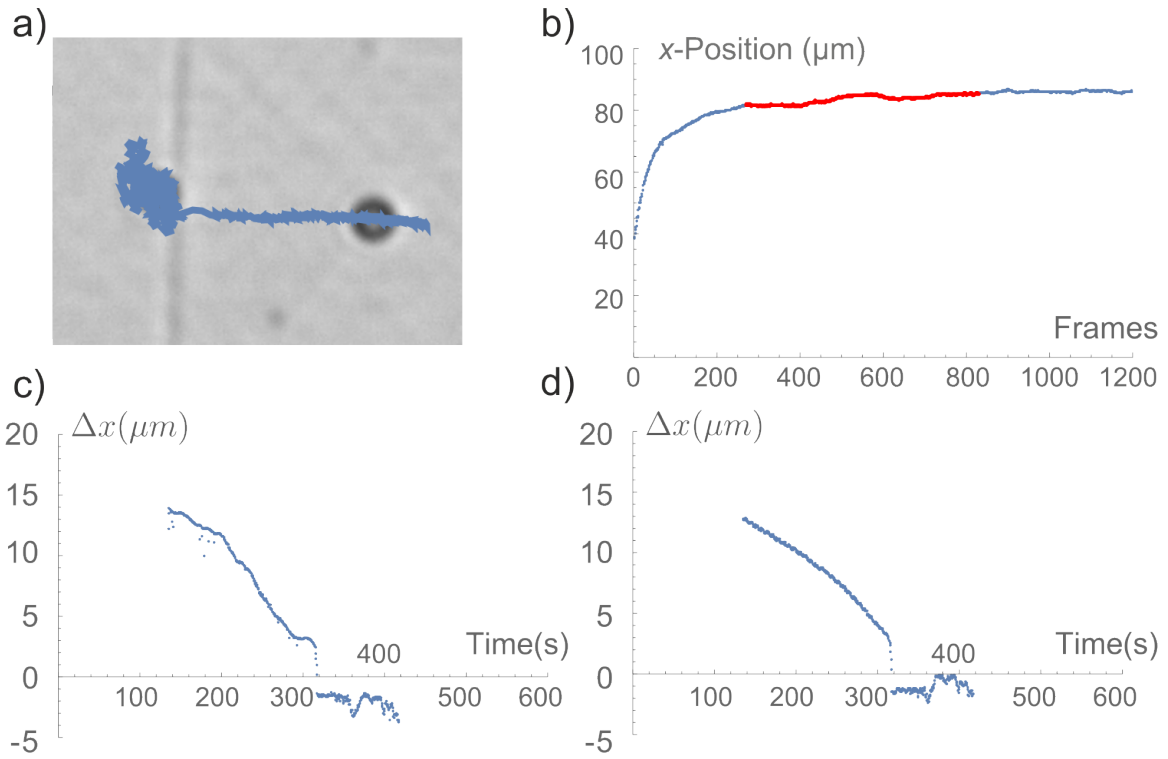


Figure 5.5: (a) Particle trajectory plotted on top of an experimental snapshot. The particle starts moving in y-direction after it enters the water phase and starts Brownian motion; (b) Plot of the fluctuation of the ice-water interface, it is clear in the first 50 seconds the interface quickly moved; (c) The distance between the particle and the interface against time, calculated using the instantaneous interface position; (d) The distance between the particle and the interface against time, calculated using the averaged interface position.

point where the particle leaves the ice completely and the interface flattens. Consequently, according to different definitions, one might claim that the particle has already left the ice when the interface is still curved.

5.4.3 Quantitative analysis of regelation

An expression for the velocity as a function of the undercooling is found by inserting Equation 5.7 (with undercooling $\nabla T = \Delta T/\Delta x$) into Equation 5.13:

$$|V| = K\Delta x^n, \tag{5.15}$$

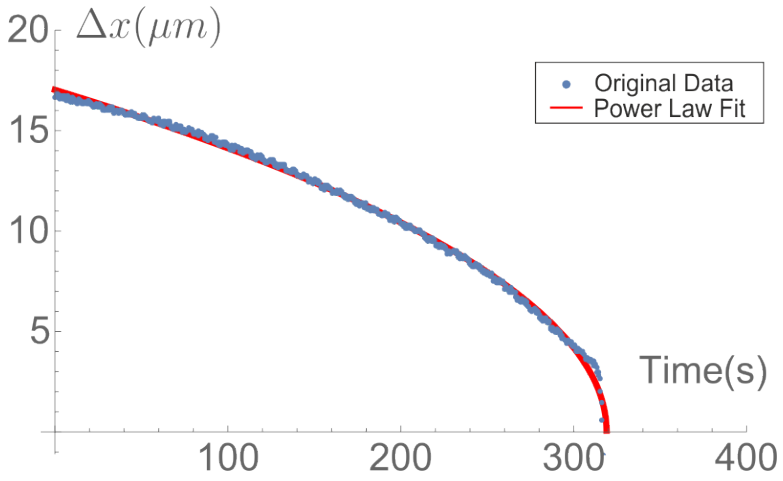


Figure 5.6: The Δx vs t plot taken until the point at which the particle leaves the ice, fitted with the best power law.

where

$$K = \frac{L_m \rho_i}{6\eta R} \lambda^3 \left(\frac{\nabla T}{T_m} \right)^{1-(3/\nu)}, \tag{5.16}$$

and

$$n = -\frac{3}{\nu}. \tag{5.17}$$

Upon integration, Equation 5.15 becomes:

$$\Delta x = [K(1-n)(t_e - t)]^{1/(1-n)}. \tag{5.18}$$

This suggests that it could be fitted with a power law,

$$\Delta x = [a(t_e - t)]^b, \tag{5.19}$$

where t_e is the fitting parameter for the time at which the particle exits the ice, $a = K(1-n)$ and $b = 1/(1-n)$. By fitting this exponential equation with our experimental data, we first determine the fitting parameters a and b, from which we obtain K and n and are able to calculate the physical constants ν, which determines which type of force is acting between the particle and the ice, and λ, the lengthscale that relates with ν, A_{iwp} and L_m.

We set the fitting parameter t_e around the time where Δx changes from positive to negative. Together with the free fitting parameters a and b, a best fit was found and plotted with the orig-

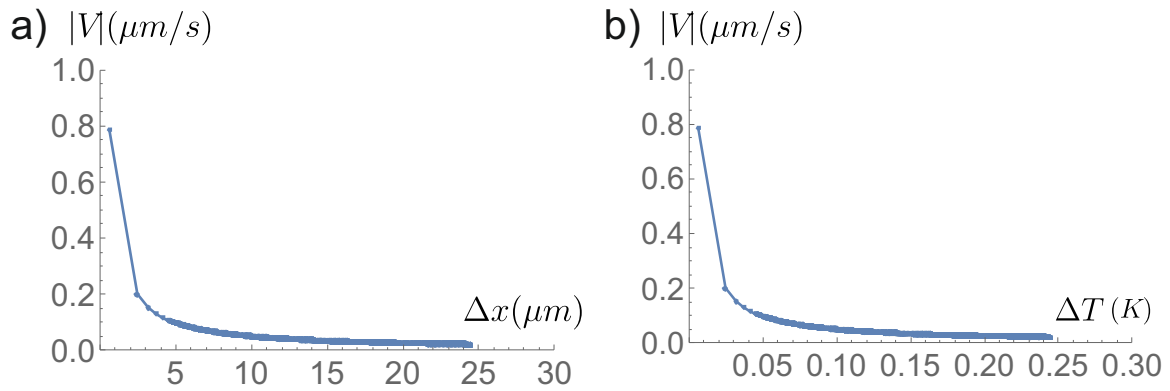


Figure 5.7: (a) The $|V|$ vs Δx plot and (b) the $|V|$ vs ΔT plot for R = 1.8 µm and ∇T = 10 K mm^{-1}.

inal data points in Figure 5.6, which shows excellent agreement, except for the few points right before the exiting event (for example the small kink at the end in Figure 5.6). This is due to the exponential nature, as we have fewer data points around this area, making this region seem more noisy. Furthermore, the exit point happens at an exact time which could be influenced by the noise in the interface position.

Using the value of a and b we have determined from the fit, we obtain the values of K and n, which are then used to calculate the velocity as the particle approaching the interface using Equation 5.15. Here we first plot $|V|$ as a function of Δx in Figure 5.7 (a). To help visualise the freezing environment, the x-axis can be replaced by undercooling using $\Delta T = \Delta x \times \nabla T$, shown in Figure 5.7 (b). From this plot, we can see that far from the interface, at low undercooling, the 1.8 µm spheres are only moving at approximately 0.03 µm s^{-1}. As they approach the interface, they accelerate up to velocities close to 0.8 µm s^{-1}.

5.4.4 The premelted layer and the related physical parameters

Finally, λ and ν can be calculated from the K and n values using Equations 5.16 and Equations 5.17. Then the premelted layer thickness, d, can be calculated as a function of the undercooling, ΔT via Equation 5.7. The result is shown in Figure 5.8 (a). In this plot, we see the expected increase in the premelted film thickness as undercooling decreases (as the particle moves towards warmer temperatures). The values obtained for the thickness are at tens of Ångstroms in scale, which agrees with our expectation. Combining Figure 5.7 (a) and Figure 5.8 (a), we have also plotted the premelted layer thickness against the regelation velocity

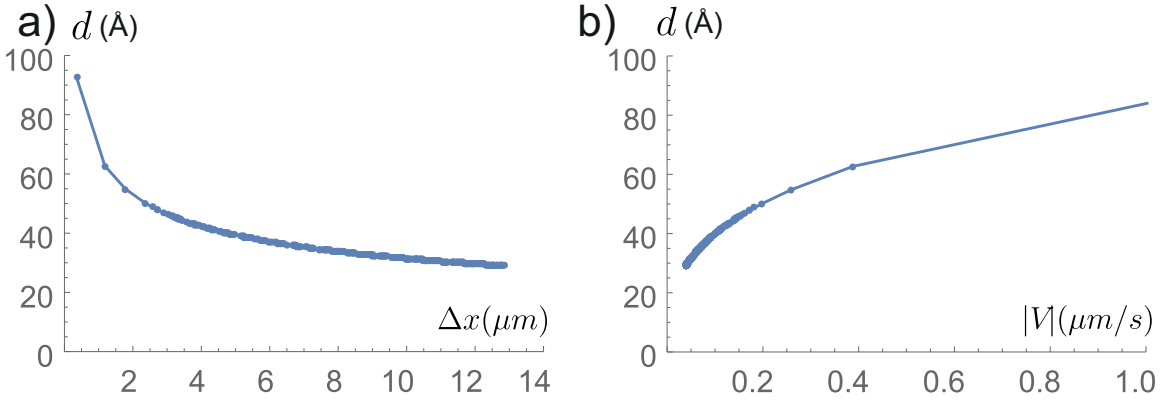


Figure 5.8: (a) The d vs ΔT plot and (b) the d vs $|V|$ plot for R = 1.8 µm and $\nabla T = 10\,\mathrm{K\,mm^{-1}}$.

Table 5.1: Conditions for regelation experiments presented in Figure 5.9. Here, λ and ν are averaged over a number of fits (N) for each particle size. 'S.D.' stands for Standard Deviation.

Particle diameter (μm)	N	ν	S.D. (ν)	λ (Å)	S.D. (λ)
1.8	19	3.05	0.16	2.55	0.35
2.5	14	3.02	0.11	2.78	0.39
3.2	13	2.93	0.17	3.11	0.77

in Figure 5.8 (b). If we cube the premelted layer thickness, we can find a linear relationship between $|V|$ and d^3, which is expected as from Equation 5.13.

The analysis was repeated for 46 particles across all 3 sizes, 1.8 µm, 2.5 µm and 3.2 µm. The results are summarized in Table 5.1 with averages and standard deviations of λ and ν. From the table we see that ν is around 3 for all sizes. According to previous literature, the ν value for short and long range electrostatic, non-retarded, and retarded van der Waals interaction are 3/2, 2, 3 and 4 respectively [54]. Hence our result indicates the main force responsible for premelting are non-retarded van der Waals interactions, instead of the electrostatic force as has been previously suggested for glass beads [131]. As for λ, similarly the value is also only determined by the type of the interaction, therefore should not change for particles with different sizes. From the mean values of λ one can observe a positive correlation between the λ and the particle diameter. This could be a result of experimental error, or it could be a sign suggesting we might want to take in account the curvature induced premelting when calculating λ in the future studies.

The regelation velocities as a function of Δx are calculated for each particle size using the averaged λ and ν, and are plotted in Figure 5.9 (a) The result for d vs Δx is plotted in Figure 5.9 (b). Here we observed that particles of all sizes move at speeds typically on the order of $0.01\,\mathrm{\mu m\,s^{-1}}$

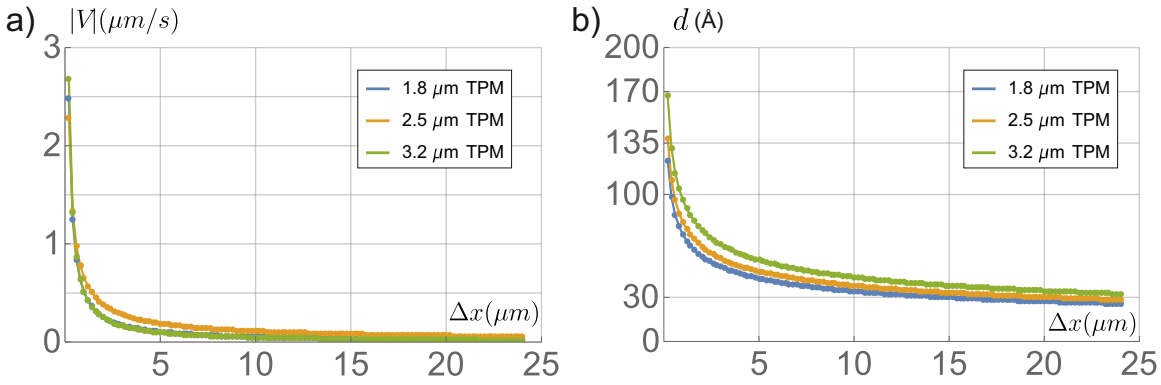


Figure 5.9: (a) The $|V|$ vs Δx plot and (b) the d vs Δx plot for all three particle sizes using the averaged value of the parameters.

when far from the interface, with a sharp increase around 5 µm (2-3 particle diameters). The bigger the particle, the greater this acceleration. The premelted layer thickness when the particle is far from the interface is about 30 Å, then as it accelerates in approaching the interface, the thickness of the premelted layer increases accordingly, up to the order of 100 Å. The premelted layer thickness is similar across all three sizes, which is expected as it is purely determined by the interaction (λ and ν) between the particle surface and ice.

5.5 Conclusions and outlook

We have observed thermal regelation of colloidal spheres out of ice at the particle scale, and experimentally measured the motion of a particle with respect to the position of the bulk ice-water interface. We fitted the interfacial premelting theory with our experimental data to gain an indication of the origin of the thermal regelation behaviour for the silica particles. Here we found the value ν was typically around 3 for all particle sizes, which corresponds to non-retarded van der Waals interactions, instead of the electrostatic force ($\nu = 2$), which was predicted previously. We were then able to calculate the premelted layer thickness and regelation velocity as a function of the undercooling. They are on the order of 30 Å and 0.01 µm s^{-1} respectively when far away from the interface, and subsequently experience an exponential growth as the particle approaches the interface. We have also confirmed that the particle radius has little effect on the premelted layer thickness.

Acknowledgments

Julia Schollick is thanked for preliminary experiments. Joe Hutchinson is thanked for proof reading.

Chapter 6

The Ice-Water Interface in the Vicinity of a Wall

ABSTRACT

We use confocal microscopy to record the shape of the ice-water meniscus between two parallel walls. We have recorded and reconstructed the interface in 3D using confocal laser scanning microscopy (CLSM). We have observed a curved interface, in the direction perpendicular to the top and bottom walls. We interpreted this curved interface as an analogue to the water-air interface rising between two parallel plates. Therefore we introduced a thermal capillary length, analogue to the capillary length for a water-air interface. However, the thermal capillary length measured from our experiment is an order of magnitude different compared to the theoretical value. By varying the experimental conditions, we found that in particular the thermal conductivity of the sample cell might have an important role in the interface shape, and as such a new theory is required to account for them.

6.1 Introduction

To date, the 3D shape of the ice-water interface has been overlooked in the literature. It is partially due to the fact that most research on the ice-water interface uses optical microscopy [100, 132], which only provides the 2D information of the interface. We have strong indications that the shape of the ice-water interface near the wall is non-linear in the direction perpendicular to the temperature gradient (along z in Figure 6.1). We believe this non-linearity plays an important role in determining the behaviour of the engulfed particles, for example within our group, we have previously observed that it helps to pin the particles towards the glass substrate [51].

To visualise the system in 3D, we need a method which can probe the interface inside the sample cell along the height z. X-ray imaging can be used to obtain 3D reconstruction of the crystals [133, 134], but so far researchers have only used it to study the freezing dynamics and ice morphology, instead of the equilibrium shape of the interface. Furthermore, artefacts induced by the beam are still problematic [135]. In this chapter, we will address this shape of the interface experimentally in 3D using confocal laser scanning microscopy (CLSM), and then use this data to elucidate the theory behind this problem with a thermodynamic approach. The confocal microscopy scans each $x - y$ focal plane to detect fluorescent dye. These focal planes are sub-micrometer apart from each other, which provides a good resolution along z and enables the reconstruction of the three-dimensional picture of the ice-water interface [31]. Similar to the control of particle engulfment discussed previously, we can control the freezing velocity so that the dye is fully expelled from the growing ice. Therefore we can easily discriminate between the water and the ice in the images.

This chapter is organised as follows: we first propose a thermodynamic description behind the curvature of the ice-water interface (Section 6.2). This is followed by the experimental section explaining the set-up (Section 6.3). The result for the curvature shape for the simple model system, fluorescent dye in deionised water, is presented in Section 6.4, along with the results for other controlled variations including changing the salt concentration, the temperature gradient and the solvent itself. Finally an outlook is presented in Section 6.5 as it turns out that the theory does not correctly describe the experiment we provide.

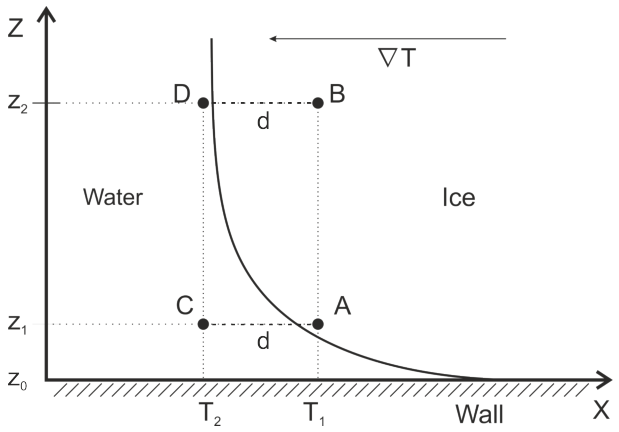


Figure 6.1: A schematic diagram of the curved ice-water interface next to a wall, under a temperature gradient, ∇T. The coordinate frame and points referred to in the derivation are also marked with black dots.

6.2 Theory

In this section we are going to present a model to describe the shape of the ice-water interface in 3D. We first introduce the governing parameter, the thermal capillary length, analogue to the capillary length for a water-air interface (Section 6.2.1). Then we introduce the mathematical solution for a symmetrical interface, the water-air interface between two parallel vertical plates. This will subsequently be used to fit our experimental data, where its validity will be checked.

6.2.1 Thermal capillary length

The following coordinate frame (Figure 6.1) is used to derive the following expressions for the ice-water interface. The glass wall is at the bottom z_0, the system has a temperature gradient imposed along the wall (the x-direction). We assume there is no temperature gradient in the z-direction, and we eliminate the gravity as the sample cell is very thin thus it only has a minor role. For the direction perpendicular to both z- and x-direction (y-direction), we assume the system is translationally invariant. We also assume that the liquid water phase wets the glass completely (θ=0°) [136], this will be checked later in our fit.

We consider a system that has reached mechanical equilibrium, where there is no flow between the points in the same phase and at the same temperature. Therefore, the pressure at point A, P_A, is equal to the pressure at point B, P_B, because they are both in the ice phase and are at

same temperature T_1. Similarly, in the water phase at temperature T_2, P_C and P_D are equal. Points B and D at a height z_2, experience a pressure difference because point D is at the interface, while point B is further in the ice phase. For points A and C, as point A is at the interface while point C is in water, a similar pressure difference exists. In addition, because points A and C are close to the wall, they will experience an additional pressure due to the curvature effect (Laplace pressure). Hence we reach the following equations:

$$P_B = P_D + \Delta P_i, \tag{6.1a}$$

$$P_A = P_C + \Delta P_w + \gamma_{iw}\kappa, \tag{6.1b}$$

where γ_{iw} is the surface tension of the ice-water interface and κ is the curvature of the interface. ΔP_i and ΔP_w are the pressure difference as a result of the different temperature along x in the ice and water phase. The pressure difference (ΔP) can be calculated using the Gibbs-Duhem equation, $nd\mu = -SdT + VdP$, where n is the number of moles, μ is the chemical potential, S is the entropy and V is the volume. As the system is in mechanical equilibrium ($nd\mu = 0$), we obtain the following equation for ice:

$$\Delta P_i = \frac{S_m^i}{V_m^i}\Delta T = S_m^i \rho_i \Delta T, \tag{6.2}$$

where S_m^i and V_m^i are the molar entropy and volume for ice. A similar derivation can be achieved for ΔP_w. We assume that the densities of ice and water are equal, and use the density of ice ρ_i throughout the calculation. By combining 6.1a and 6.1b, we then get:

$$\gamma_{iw}\kappa = \Delta P_i - \Delta P_w = (S_m^i \rho_i - S_m^w \rho_w)\Delta T = (S_m^i - S_m^w)\rho_i \Delta T, \tag{6.3}$$

As $\Delta T = \nabla T \times d$, where ∇T is the temperature gradient and d has been indicated in the Figure 6.1. $\Delta S = S_m^i - S_m^w$ is related to the enthalpy of fusion for water (latent heat) according to $L_m = \Delta S \times T_M$, where T_M is the melting temperature of water. Therefore, by substituting and rearranging, we obtain:

$$\frac{d}{\kappa} = \frac{T_M \gamma_{iw}}{\rho_i L_m \nabla T}. \tag{6.4}$$

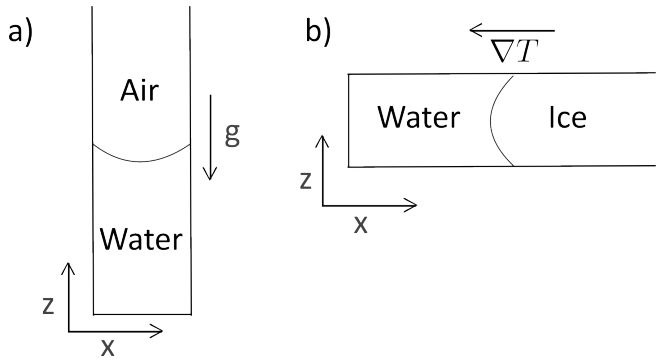


Figure 6.2: (a) The set-up in Landau and Lifschitz's mathematical derivation; (b) The set-up in our experiment.

In hydrostatics, we can extract a characteristic length scale, the capillary length ($L_{cap} = \sqrt{\gamma/\Delta\rho g}$), for an interface under gravity. Here, analogously to this capillary length for the liquid-air interface, we can extract a length scale for the ice-water interface from Equation 6.4, with the temperature gradient ∇T acting as the gravitational field:

$$L_T = \sqrt{\frac{T_m \gamma_{iw}}{\rho_i L_m \nabla T}}. \tag{6.5}$$

Therefore, using $T_m = 273$ K, $\rho_i = 0.9167\,\mathrm{g/cm^3}$, $L_m = 334\,\mathrm{J/g}$ and a literature value of $\gamma_{iw} = 29.1\,\mathrm{mJ/m^2}$ [96], the theoretical L_T can be calculated for a given ∇T. For $\nabla T = 10\,\mathrm{K\,mm^{-1}}$, the temperature gradient used in most of our experiments later, we find that $L_T = 1.61\,\mu\mathrm{m}$.

6.2.2 Shape of the interface

Landau and Lifschitz gave a theoretical description of the shape of a fluid interface between two parallel vertical plates [137]. The geometry is similar to our ice-water meniscus set-up, with the temperature gradient ∇T acting as the gravitational field (Figure 6.2). For a symmetrical interface, we can simplify the problem by only focusing on half of the ice-water meniscus, with the correct boundary condition. Landau and Lifschitz demonstrated that the shape of the half interface can be described using the following equation [137]:

$$z = \int_{x_0}^{x_1} \frac{c - x^2/L_T^2}{\sqrt{1 - (c - x^2/L_T^2)^2}} dx, \tag{6.6}$$

where c is a constant depending on the contact angle, θ, between the ice-water interface and the wall, x_0 and x_1 represent the lowest and highest position of the meniscus respectively, and L_T is the thermal capillary length. The constant c is found from the condition when $x = x_1$ for $z = \frac{1}{2}h$, or

$$\frac{h}{L_T} = \int_0^{\frac{\pi}{2}-\theta} \frac{\cos\xi}{\sqrt{c - \cos\xi}} d\xi, \tag{6.7}$$

where the new variable ξ follows from $x = L_T\sqrt{c - \cos\xi}$.

6.3 Experimental

6.3.1 Materials and equipments

Alexa Fluor® 488 NHS Ester (Succinimidyl Ester) (Alexa dye) was purchased from ThermoFisher. A stock solution was prepared at a concentration of 768 µM in deionised water, and subsequently diluted to the desired concentration according to each experiment. Rhodamine B isothiocyanate mixed isomers (RITC) and *tert*-Butanol were purchased from Sigma. Stock solution of RITC in *tert*-Butanol was prepared at a concentration of 1 µM, and subsequently diluted to 0.25 µM.

To determine the exact three dimensional shape of the ice-water interface inside the glass walled sample cell, confocal microscopy was used. The confocal images were taken using a custom Thorlab-Olympus confocal set-up described in Section 2.2.3, where a Thorlabs confocal scan head and laser source were installed onto an Olympus IX73 microscope, and a Olympus Long Working Distance M-Plan Fluorite 50x objective was used. For Alexa dye, the excitation maximum is at 490 nm and the emission is at 525 nm, therefore the 488 nm laser light and a dichroic cube with a 495 nm longpass dichroic filter was used. For RITC, the excitation is at 543 nm and the emission is at 580 nm, the 532 nm laser light and a dichroic cube with a 538 nm longpass dichroic filter was used. This cube was also equipped with a 582/78 nm filter to sharpen the resulting image. In both scenarios the dichroic cube is placed so that there is a channel dedicated for the backscattered light, which was used to detect the position of the glass boundaries. This utilises the refractive index mismatch of glass and water, which scatters the original laser light. This scattered light can be directed so that it goes directly to the imaging photomultiplier tube

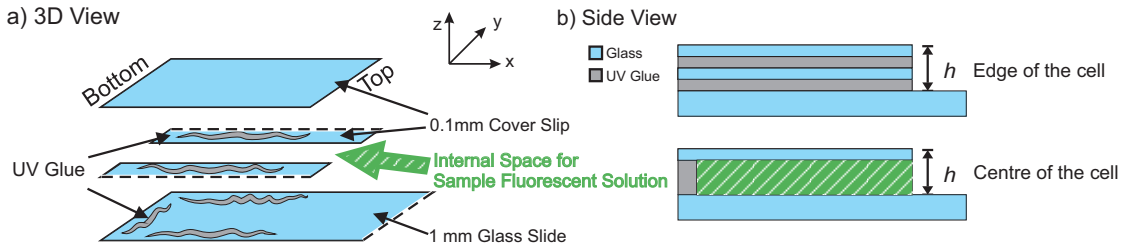


Figure 6.3: (a) Diagram of the methods for making sample cells (not to scale), dashed lines represent cut glass edges; (b) The side view of the filled sample cell, for a cross section at the edge and at the centre.

(PMT) without going through the dichroic filter. All images were taken using the ThorImage^{TM} software and were processed in ImageJ and Mathematica.

Conventional glass cells with parallel walls were used in these experiments (Figure 6.3). The advantage of the conventional glass set-up over the micro-lithography used previously is its well defined optical and thermal properties. Microscope slides (76 mm x 26 mm x 1 mm) and cover slips (22 mm x 50 mm x 0.1 mm) were purchased from vwr UK. UV glue (NOA 81) was purchased from Norland Products to glue the slides together and to create the boundary for the cells. The internal height, h, is 0.1 mm, unless otherwise stated. For each experiment with the 0.1 mm cell, 100 µL fluorescent solution was inserted from the unsealed end, which was left open and placed on the cold plate to reduce evaporation during the experiment process. In later experiments one side of the glass cell was replaced by aluminium or was coated with SU-8 2035, an epoxy-based photoresist which has different thermal properties compared to glass. The SU-8 was purchased from MicroChem. We have followed the procedure described in Section 2.2.5 to achieve a coating thickness of approximately 100 µm.

6.3.2 Experimental methods

The schematic diagram for the optical set-up (with the cooling stage) is shown in Figure 6.4. The sample glass cell filled with 100 µL fluorescent solution was placed on the cooling stage, with the open end on the cold plate to minimise evaporation. As the fluorescent solution was made with deionised water, the cold plate was initially cooled to -20 ℃ rapidly to overcome supercooling and ensure the nucleation of the ice. The formation of ice was confirmed through bright-field microscopy, and then the temperature of the two plates were then set to meet the desired temperature gradient. Unless otherwise stated, the cold plate (T_C) was set to -10 ℃ and the hot plate (T_H) was set to 10 ℃ to reach a temperature difference of 20 K. As the gap

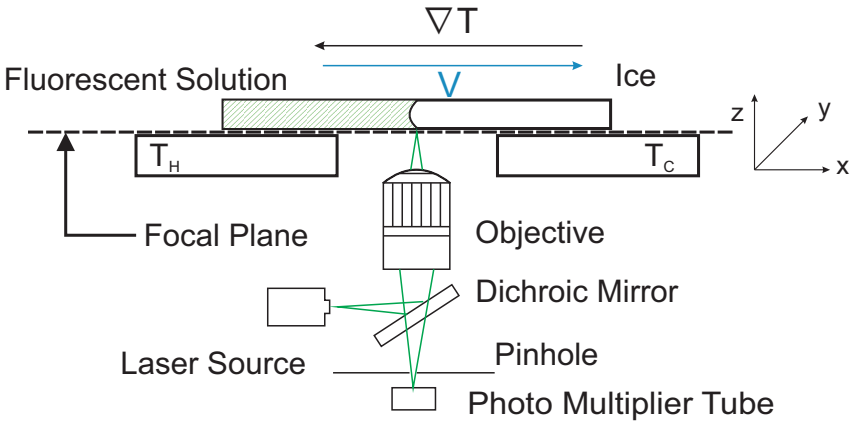


Figure 6.4: Diagram of the confocal microscope set-up (not to scale). The sample cell sits on hot and cold plates with temperatures T_H and T_C, and thus form a temperature gradient, ∇T, from cold to warm.

between the two plates is 2 mm wide, the temperature gradient ∇T is thus equal to $10\,\mathrm{K\,mm^{-1}}$. To obtain a sharp interface, a cell filled with fluorescent solution was moved at a small velocity ($\mathrm{V} = 1\,\mu\mathrm{m\,s^{-1}}$) through the fixed temperature gradient into the cold plate. This is related to the critical velocity we have discussed in Section 4.2.1: if the sample is frozen at low freezing velocity, all the fluorescent dye is rejected from the ice phase thus fluorescent dye-free ice are formed. This ensures a distinct difference between the water and ice phases can be achieved when excited by a laser. After an hour of this directional freezing, the interface was stabilised for another hour to reach mechanical equilibrium before we started recoding the 3D structure of the meniscus. A series of images in the $x-y$ plane were taken, $0.5\,\mu\mathrm{m}$ apart from each other in the z-direction, and the 3D image of the ice-water interface was then reconstructed using ImageJ and Mathematica.

6.3.3 Reconstruction of the ice-water interface

An example of the reconstructed 3D image using ImageJ is shown in Figure 6.5 (a). Here the sample interface is formed by freezing $100\,\mu\mathrm{L}$ of $768\,\mu\mathrm{M}$ Alexa solution in a sample cell with a thickness of 0.12 mm at the temperature gradient of $10\,\mathrm{K\,mm^{-1}}$. By using Mathematica, we can view the 2D cross section about the $z-x$ plane at an arbitrary value of y (Figure 6.5 (b)). The interface is represented by the sharp transition from bright to dark, therefore for each z value, the pixel profile along x can be fitted with a hyperbolic tangent function $y_i = a + b\tanh[(x_i - c)/d]$, where y_i is the intensity of the pixel, x_i is the pixel along x, and

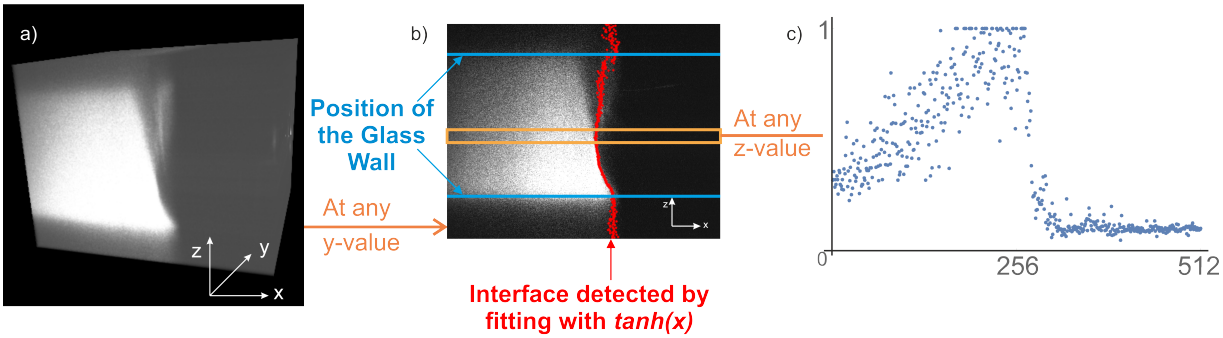


Figure 6.5: (a) Reconstruction of the interface in 3D; (b) A x-z slice at y=50 µm. The red line in the figure represent the position of the interface, the blue lines represent the positions of the glass slides; (c) A plot of pixel values against x values at z=100 µm.

a, b, c, d are free fitting parameters (Figure 6.5 (c)). Repeating this for all z values in one 2D slice thus gives the profile of the interface (plotted in (Figure 6.5 (b)) in red).

Because there is no fluorescent dye beyond the glass wall, all the bright pixels detected at these positions are noise and reflections. Therefore we need to cut out this noise. To do so, we first find the boundary of the glass slide wall, which is achieved by using the backscattering channel. This is because the scattering intensity reaches its maximum at the edge of the glass, and decays with distance in a Gaussian style. Therefore the position of the wall can be extracted by fitting the pixel information with the Gaussian function $y_i = m \times e^{\frac{-(x_i-n)^2}{2p^2}} + q$ using Mathematica, where m, n, p, q are free fitting parameters.

The experimental z value was then compared to the theoretical z value to determine the best theoretical fit with the θ and L_T values for each experiment. To do so, first, a series of c and θ values were generated (Figure 6.6 (a)), then the capillary length and x_0 was calculated using Equation 6.7 and $x_0 = L_T\sqrt{c-1}$ for each set of c and θ. Using this L_T and x_0, the theoretical z value can be calculated for each experimental x value by integrating Equation 6.6 from the corresponding x_0 to x_1, where x_1 corresponds to the experimental x value. We then take the square of the difference between the theoretical value and experimental value, the set of the c and θ values that gave the lowest difference is thus determined as the best fit. This procedure is graphically illustrated in Figure 6.6 (a), which shows there is a clear minimum in the variance as a function of the fit parameters θ and c. Improvements in tracking the interface would reduce noise in the resulting interface, and thus a smaller variance, but the actual fitted value are expected to change only marginally. The corresponding L_T is then calculated and plotted with the original data in Figure 6.6 (b).

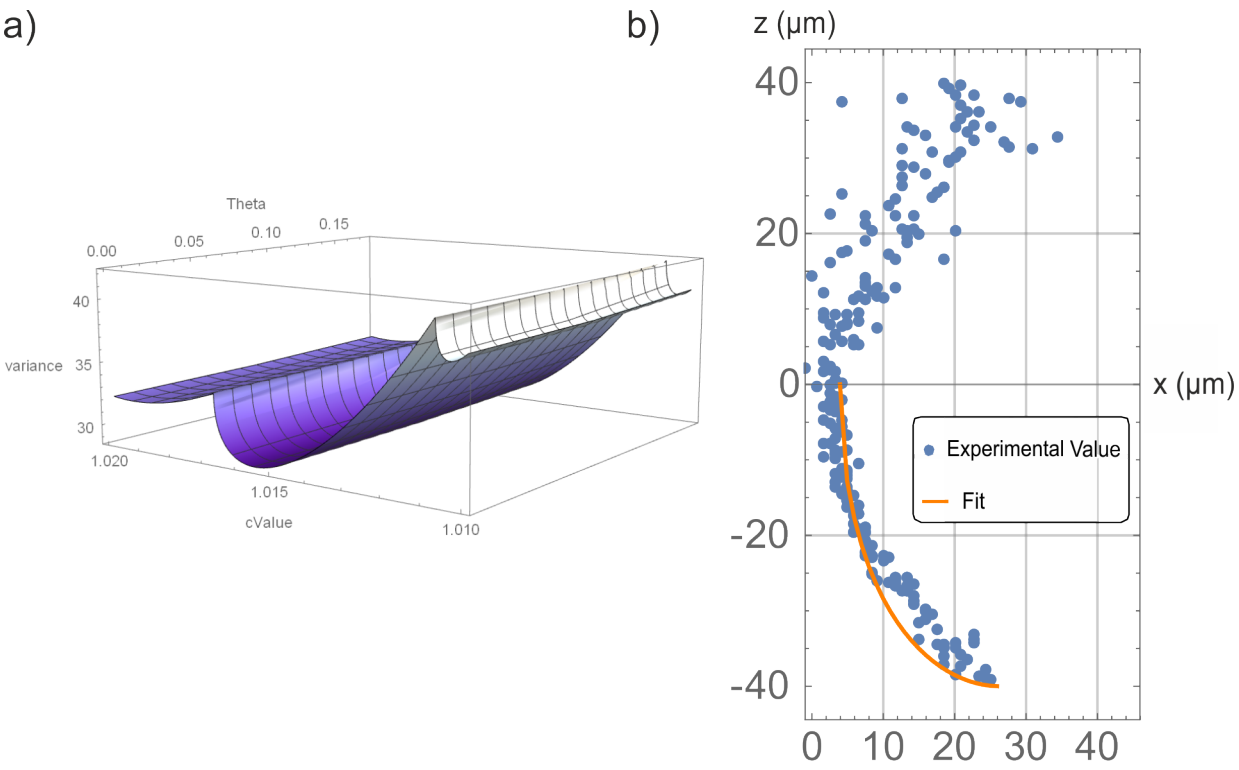


Figure 6.6: (a) The 3D plot of the variance (square of the difference between the theoretical value and experimental value) for different c and θ values; (b) A plot of the detected experimental interface in x-z, plotted with the fit using Equation 6.6 in the lower half of the interface.

6.4 Results and discussion

In this section we present the results of the interfaces depending on various conditions (different dye concentration, salt concentration, cell thickness, temperature gradient, different solvent system or different sample cells). We fit them to the theoretical expression (Equation 6.7) and interpret the resulting L_T.

6.4.1 Fluorescent dye concentration

As we have shown in Chapter 3, the concentration of the impurities affects the degree of premelting and may cause an interface instability. It also changes the surface tension [138], which is involved in our calculation of L_T in Equation 6.5. Therefore, firstly we need to characterise the effect of different amount of fluorescent dye used in our system. We tested four different concentrations (768 µM, 384 µM, 192 µM, 7.68 µM) of Alexa dye. The resulting interfaces are

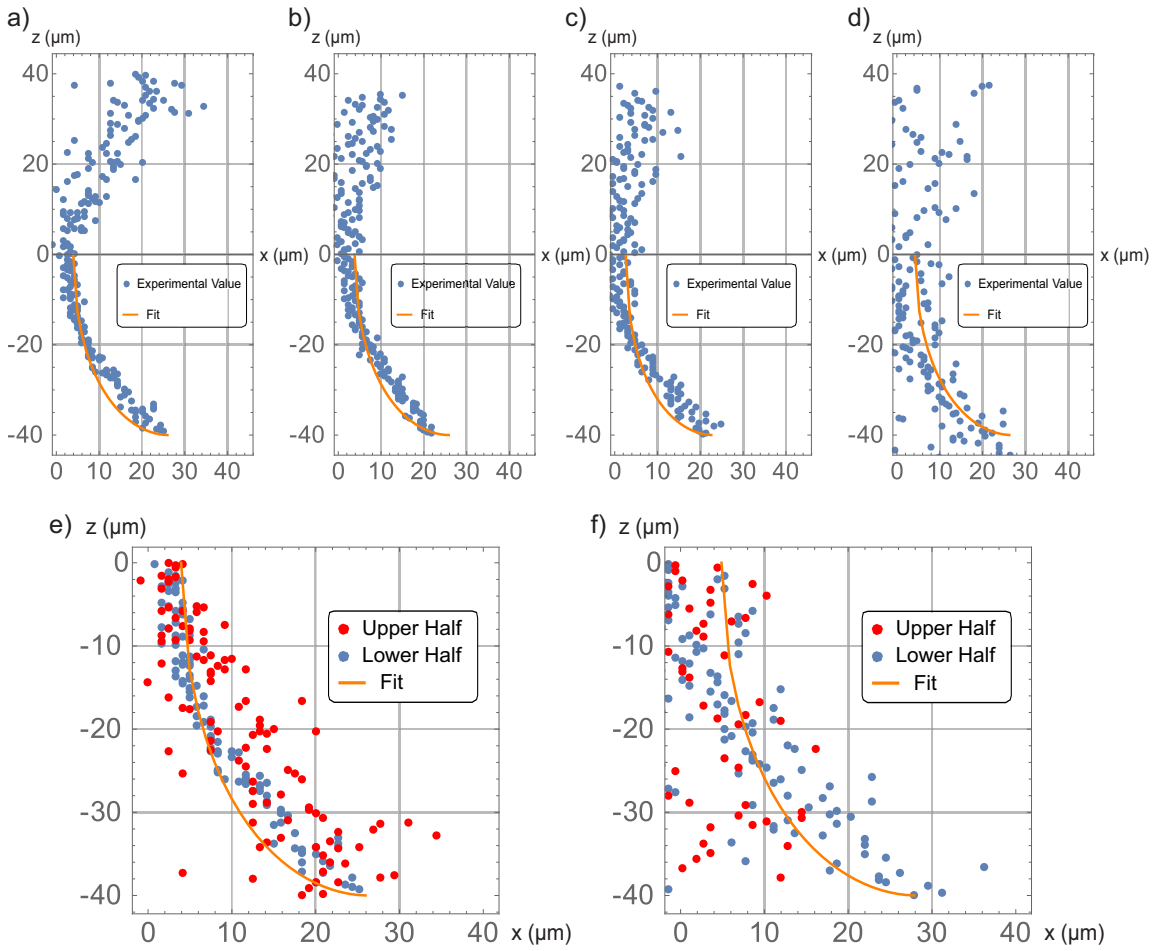


Figure 6.7: (a - d) Extracted ice-water interface information, plotted with the fit using Equation 6.6, for concentration of 768 µM, 384 µM, 192 µM and 7.68 µM; (e) The interface from a concentration of 768 µM was flipped with regarding to the mid-plane to check the symmetry; (f) The symmetry was also confirmed for the interface from a concentration of 7.68 µM.

shown in Figure 6.7.

As shown in Figure 6.7 (a - d), the overall shape of the resulting interfaces are very similar, thus we can conclude that the concentration of the fluorescent dye itself does not have a strong impact on the shape of the interface. This similarity is further confirmed from our fitting result (shown as the solid orange line), which we will discuss shortly. Besides, at the highest dye concentration, shown in Figure 6.7 (a), we can see the symmetry of the resulting interface, despite the optical distortion caused by the meniscus which makes the upper half more noisy. With the decrease of the concentration, the information of the upper part of the interface is increasingly lost, with Figure 6.7 (d) being the interface from the lowest dye concentration. To confirm the symmetry of the interface, we flip the upper part of the data points with respect to the mid-plane to see if it overlaps with the lower half. The flipped result is shown in Figure 6.7 (e&f), where the

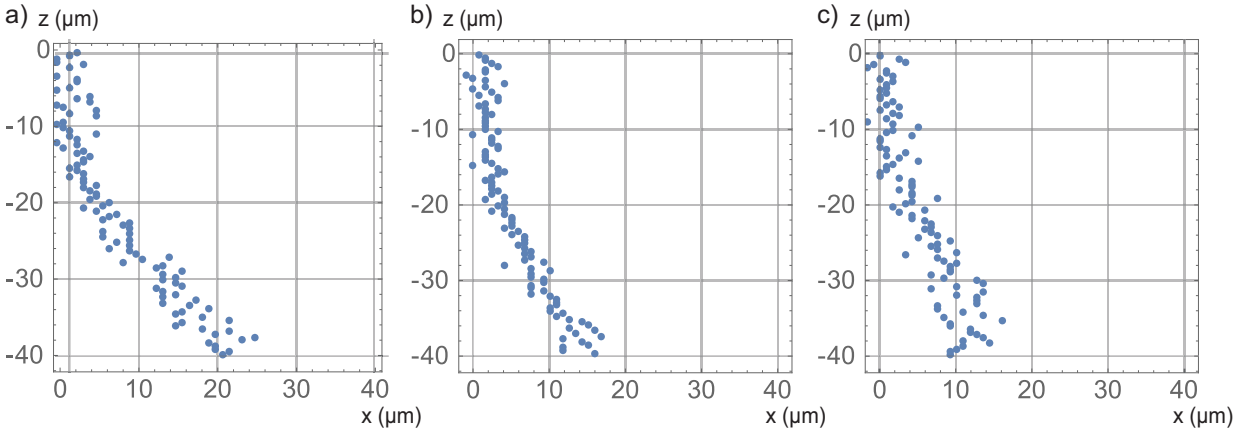


Figure 6.8: (a) The interface resulted from 192 µM Alexa dye with no salt; (b) The interface resulted from 192 µM Alexa dye with 1.5 w/w % KCl; (c) The interface resulted from 192 µM Alexa dye with 3 w/w % KCl.

upper interface overlaps with the lower part for both the highest and lowest dye concentration, therefore the symmetry is confirmed.

On that follows, we will compare the interface shapes at different concentrations by focusing on the lower half. We fitted the lower half of the experimental data using Equation 6.6 to extract the contact angle θ and L_T experimentally. The results obtained for θ is 0° for all concentrations, as we expected, while we obtained $L_T = 24\,\mu m$ for 768 µM dye, $L_T = 25\,\mu m$ for 384 µM dye, L_T =23 µm for 192 µM dye, $L_T = 28\,\mu m$ for 7.68 µM dye. These numbers are fairly consistent, however they are about an order of magnitude different from our predicted values. According to our theory (Equation 6.5), we have found $L_T = 1.61\,\mu m$ for $\nabla T = 10\,K\,mm^{-1}$.

6.4.2 Higher salt concentration

The concentration of dye does not significantly change the interfacial behaviour. However the typical salt concentration used in studies of directional growth [139,140] are much higher, therefore to further elucidate the effects of salts, we added KCl to the 192 µM fluorescent solutions, to reach 1.5 w/w % KCl (0.201 M) and 3 w/w % KCl (0.402 M). The results for these different salt concentration are summarised in Figure 6.8.

Following our earlier verification of the symmetry with regarding to the mid-plane, only the lower half of the interface has been shown here for comparison. We can see that with the increase of the salt concentration, the interface is less spread out in the x-direction, although the effect is not drastic.

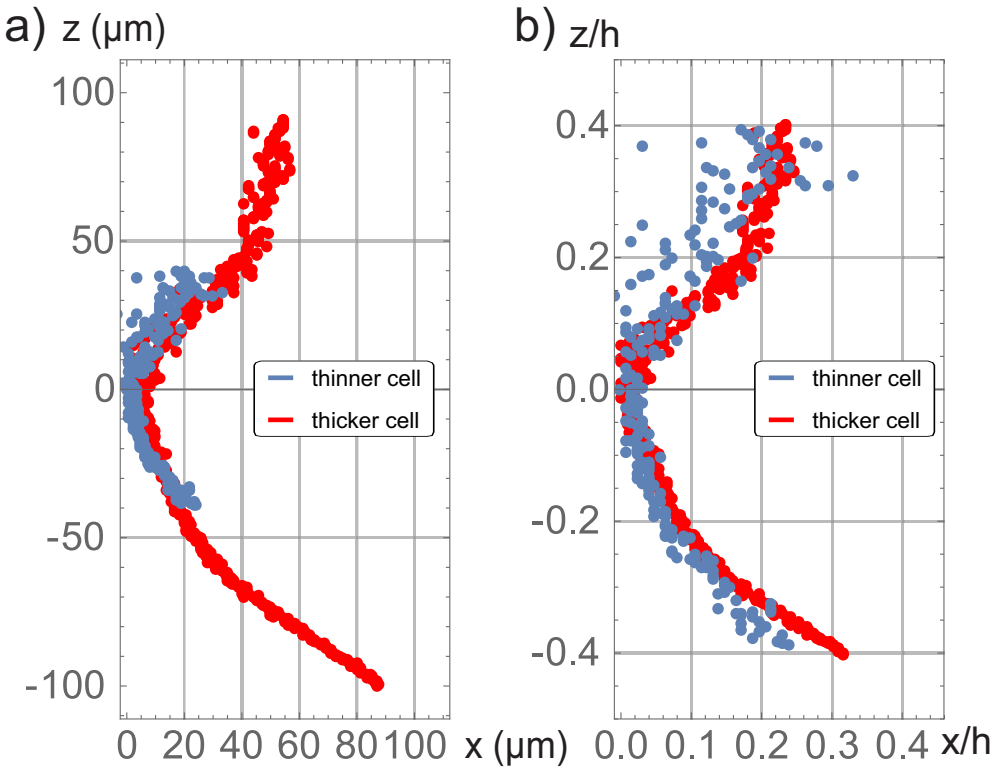


Figure 6.9: Interface resulted from two different cell thickness. (a) Direct plot of the two interfaces; (b) Scaled plot (x,z value divided by the corresponding cell thickness h) of the two interfaces.

6.4.3 Cell thickness

As described in Section 6.3.1, the default thickness h for the sample cell was set to 100 µm. According to Equation 6.7, this thickness h scales the shape of the interface. To verify the role of the cell thickness, glass cells with a larger internal height were made, with two cover slips in the middle as steppers to achieve $h = 220$ µm.

We have directly plotted the two interfaces together in Figure 6.9 (a), where the interface resulted from $h = 100$ µm is plotted in blue and the interface resulted from $h = 220$ µm is plotted in red. Because the two interfaces are totally different in their scales, we scaled the interface by their corresponding h, and plot the scaled plots together in Figure 6.9 (b). Here we can see that the two interfaces overlap, indicating that h only scales the whole meniscus.

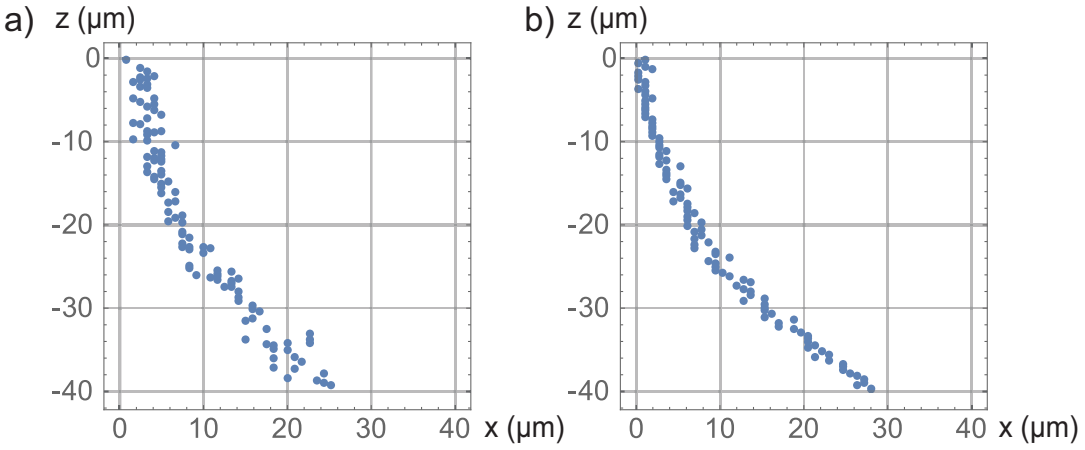


Figure 6.10: The lower half of the interface resulted from two different temperature gradients: (a) $\nabla T = 10\,\mathrm{K\,mm^{-1}}$ and (b) $\nabla T = 30\,\mathrm{K\,mm^{-1}}$.

6.4.4 Temperature gradient

The thermal capillary length is predicted to be inversely proportional to the temperature gradient according to Equation 6.5. Therefore, we anticipate a bigger temperature gradient will lead to a smaller L_T, thus changing the shape of the interface curvature. To test it experimentally, here we compare the resulting interface from $10\,\mathrm{K\,mm^{-1}}$ to a interface formed at a temperature gradient of $30\,\mathrm{K\,mm^{-1}}$.

As shown in Figure 6.10, the resulting interface structures from the two temperature gradients are very similar. From our fitting, we obtained a L_T value of 28 µm, for temperature gradient of $30\,\mathrm{K\,mm^{-1}}$. This value is comparable with the L_T for the lower temperature gradient (which was $23\,\mathrm{K\,mm^{-1}}$), while according to our theory Equation 6.5, the L_T should decrease with increasing ∇T, thus the ratio of L_T^{10}/L_T^{30} should be around 1.7. This mismatch again indicates there are some key factors we are missing in our theory.

6.4.5 Organic solvent

In freeze casting industry, organic solvents such as *tert*-butyl alcohol (TBA) are also widely used to achieve different morphological characteristics such as ice prisms after freezing [141]. To record the solid-liquid interface for *tert*-butyl alcohol, RITC was used instead of Alexa, due to the poor solubility of Alexa in organic solvents. All sample treatments, freezing conditions and

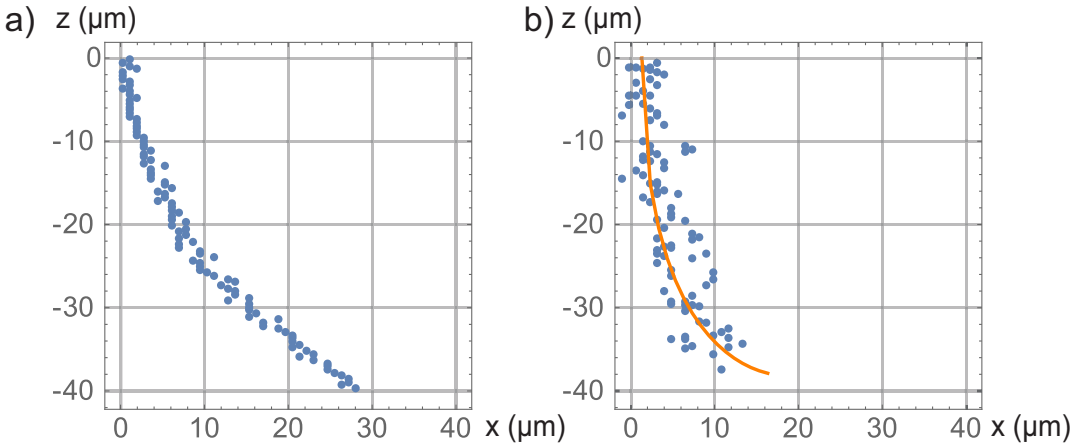


Figure 6.11: Comparison of the interface resulted from (a) Alexa in water and (b) RITC in *tert*-butyl alcohol under a temperature gradient of $\nabla T = 30\,\mathrm{K\,mm^{-1}}$. The fitting using Equation 6.6 was also plotted for (b).

confocal microscopy are kept the same, except that a 532 nm laser light together with a 560 nm longpass dichroic filter were used.

As the melting temperature of *tert*-butyl alcohol is 25.7 ℃, to achieve a temperature gradient of $10\,\mathrm{K\,mm^{-1}}$, the cold plate was set to 15.7 ℃ and the hot plate was set to 35.7 ℃ after nucleation was confirmed. However, this low temperature gradient could not provide a sharp image, therefore the larger temperature gradient, $\nabla T = 30\,\mathrm{K\,mm^{-1}}$, was used instead.

The *tert*-butyl alcohol solid-liquid interface was plotted with the interface of water in Figure 6.11, both are at temperature gradient of $30\,\mathrm{K\,mm^{-1}}$. It is clear that the interface for *tert*-butyl alcohol is flatter than the interface for water, as their physical properties including surface tension and wetting of the glass boundary are very different. Naturally the value of L_T is very different. As anticipated, the fitting using Equation 6.7 works well for *tert*-butyl alcohol as well. Furthermore from our fitting, we obtained a contact angle of 10° for TBA, while for water it showed complete wetting ($\theta = 0°$).

6.4.6 Thermal conductivity

The L_T we extracted from the experiment is a order of a magnitude different from what we expect from theory. One possibility is that the thermal property of the sample cell plays a role, especially the thermal conductivity of the materials should be included. To verify this, we have coated the top glass cell with SU-8, an epoxy-based photoresist which has a lower thermal con-

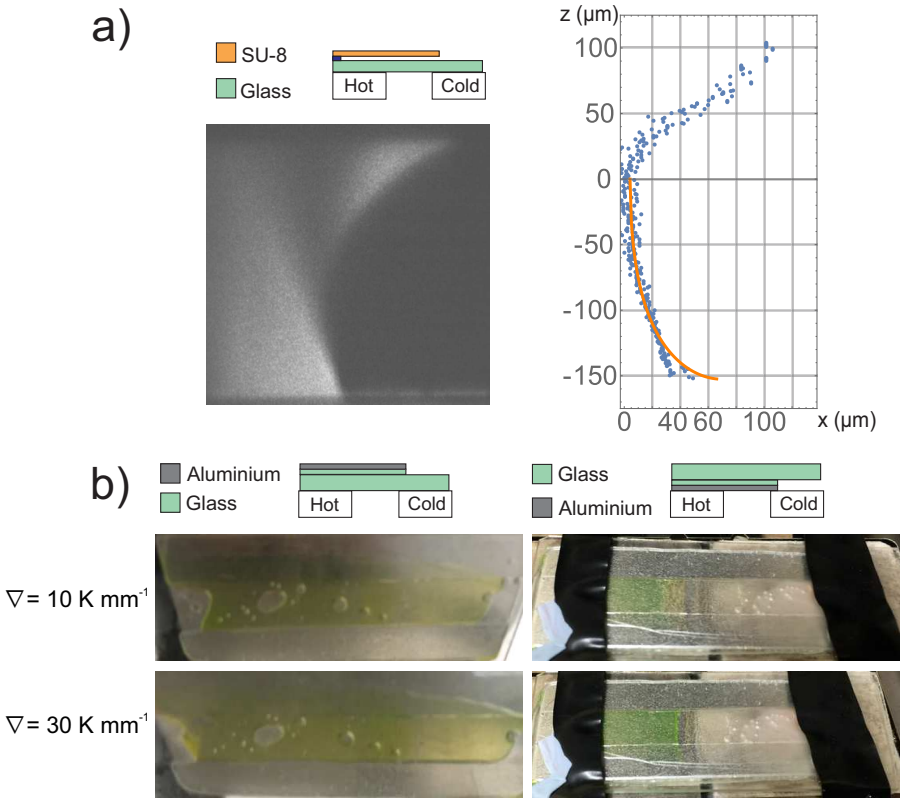


Figure 6.12: (a) The interface resulted from the sample cell made from the top glass coated with SU8, it is clear that the symmetry of the interface has been broken; (b) The experimental results from using the sample cell made from one aluminium wall and one glass wall. When the aluminium wall is placed at the top, no ice was formed; when the aluminium wall is placed at the bottom, the interface was formed as usual.

ductivity than glass (Figure 6.12 (a)). The interface resulted from this thermally asymmetrical cell is indeed asymmetrical as well. Here, the smaller heat conductivity resulted in a longer spread out of the curvature in the x-direction. Note that we could use our theory to fit to the interface formed at the glass side, while we can not fit it with the interface formed at the SU-8 side, indicating a new theory is needed to in cooperate the thermal conductivity.

We have also replaced the upper boundary with aluminium. Interestingly, if we place the glass side at the bottom touching the freezing stage, no ice was formed (Figure 6.12 (b)). If we turn the sample cell around and place the aluminium side at the bottom, an interface was formed. However due to the inverted microscope set-up, the interface cannot be imaged using confocal microscopy. Altogether, this indicates the thermal conductivity of the cell is having an important role in the interface morphology.

6.5 Conclusions and outlook

Confocal microscopy has successfully been employed to measure the shape of the ice-water meniscus in a glass walled sample cell; we have clearly observed the curvature of the interface. We have demonstrated that the interface morphology can be fitted by adopting the approach first developed by Landau and Lifschitz for the fluid surface rising between two parallel vertical float plates (Equation 6.6). We have also characterised the effect of different experimental conditions (cell thickness, temperature gradient or different solutions) on the curvature. Unfortunately, these experimental thermal capillary length (L_T) is a magnitude out comparing to our theoretical value. We think this might due to the lack of some key parameters such as thermal conductivity in our theory, which will be included in the future studies.

Acknowledgments

Rob Style is thanked for many useful discussions about the theory. Julia Schollick and Arran Curran are thanked for providing assistance with the confocal microscope. Julia Schollick and Adam Stones are thanked for discussions regarding fitting using Mathematica. Josh Abbott is thanked for proof reading.

Summary

In this thesis we studied the ice-water interface and its interaction with colloidal particles. Our approach was to use a freezing stage which provides a well-defined temperature gradient and precisely controlled freezing velocity, in combination with light microscopy. Two different microscopy techniques were used, namely bright-field and confocal microscopy. We have synthesized TPM particles as our model system, which gave us advantages such as precise size control and known physical properties.

In Chapter 3 we focused on the instability at the ice-water interface and its relationship to the freezing environment. We first studied the influence of freezing velocity on the formation of perturbations and instabilities of the supernatant from the colloids (salt solutions), and compared the experimental observations to the predictions calculated according to the Mullins-Sekerka instability. Then we introduced particles to the same salt environment, to distinguish the roles of the particles in forming the instabilities. Previously it has been reported that the salt ions have a bigger role in causing supercooling compared to the presence of the particles. Because supercooling causes a local reversion of thermal fields which leads to instabilities, one might expect the salts are more important than the particles in causing the instabilities as well. However, our experiments showed a clear impact purely from the presence of the particles.

In Chapter 4 we focused on the structures formed by the colloidal particles accumulating in front of the ice-water interface during the directional freezing. Different image analysis methods were applied to characterise the crystallinity of the cluster structures. We found that despite the slow freezing velocity, the increase of the particle concentration is still too quick for a crystal structure to form in front of the interface. Meanwhile, once the particles have been entrapped by the ice, they will form fine, linear or zig-zag structures between the ice fingers.

In Chapter 5 we moved on to investigating how a single particle interacts with ice close to the melting temperature, after it has been engulfed by the ice. We focused on the event of 'thermal

regelation', the movement of the particles in ice towards the ice-water interface. We tracked the position of the particle and the interface, the resulting trajectory clearly showed that the particle accelerates out of the ice. We fitted our experiential data with the theory to determine the physical parameters that represents the interaction between the ice and the particle. From our calculation, the interaction between the silica particle and the ice is the non-retarded van der Waals interactions. We were then able to calculate the thickness of the premelted layer, and to see how it grows during the regelation event. Furthermore, we have also tested and found that there is no influence of the particle size on the physical parameters thus the premelted thickness, which is as expected since these parameters are only determined the type of the interactions.

In Chapter 6, we studied the shape of the ice-water interface in 3D using confocal microscopy, which has been overlooked in literature so far. We observed a curved interface in the direction perpendicular to the temperature gradient (top and bottom walls). We first interpreted this curved interface as an analogue to the water-air interface rising between two parallel plates and introduced a thermal capillary length term, analogues to the capillary length for a water-air interface. However, the thermal capillary length measured from our experiment is an order of magnitude different compared to the theoretical value. By varying the properties of the experimental system (for example the internal height of the sample cell, the properties of the solvents), we suspect the difference in the thermal capillary length might be due to the fact that we did not include the thermal conductivity of the sample cells.

Each chapter addresses its own fundamental question on the behaviour of the ice-water interface in a colloidal suspension. They are also strongly interconnected: Chapter 3 and 4 report on the Mullins-Sekerka instability in systems without and with colloidal particles, where it can be seen that the build-up of the colloids at the interface plays a role in the development of the instability. Moreover, under certain conditions the instability can lead to the engulfment of particles, of which the subsequent regelation happens, and is described in Chapter 5. The underlying physics describing engulfment and regelation have similar concepts. In all these experiments, special care was taken to reduce the possible influence of the curvature of the interface, i.e. all particles experience the same curvature at the interface, by strongly confining the system. Chapter 6 specifically looks into the 3D shapre of the interface and the interplay between curvature, confinement and interfacial tension.

This thesis shines light on some fundamental thermodynamics in the ice-water systems. Based on the experiments and results presented in this thesis, several suggestions for future work can

be made:

1. In Chapter 3 we have predicted the preferred instability wavelength for the salt system. However due to the limitation posed by our experimental conditions, we were only able to see stable perturbations, not the fully developed instabilities. It will be interesting to design and make longer microfluidics channels, in couple with higher salt concentrations, to ensure the perturbations can fully develop instabilities. Besides, towards the end of the chapter we mentioned a power law relationship between the instability wavelength and freezing velocity has been detectable for small particles ($\sim 100\,\mathrm{nm}$). Once we have more fully developed instabilities, it will enable us to examine whether this power law still valid for big particles.

2. In Chapter 4 we investigated how particles form clusters in front of the ice-water interface. A special case was observed at the freezing velocity $2\,\mu\mathrm{m\,s^{-1}}$. More experiments at different freezing velocities close to $2\,\mu\mathrm{m\,s^{-1}}$, together with varying the particle concentration, will help to understand its unique behaviour. Besides, we can introduce particles with different surface chemistry (different charges) to the system. It will be especially interesting to see if the positively charged particles act differently, compare to the negatively charged TPM particles used here.

3. In Chapter 5 we investigated the thermal regelation of individual colloidal spheres. In our experiments we have only used spherical particles, while in reality there are rarely perfect spherical particles in the nature. This would allow for a much deeper understanding of the regelation behaviours if we can use particle of different shape and to see how they behave.

4. For the 3D shape of the interface, experimentally we have identified the curvature of the interface, and now we have strong indications that the thermal conductivity of the sample cells plays a role here, which should be included in a new theory.

Bibliography

[1] M.I. Budyko. The effect of solar radiation variations on the climate of the earth. *Tellus*, 21(5):611–619, 1969.

[2] K.Y. Vinnikov, A. Robock, R.J. Stouffer, J.E. Walsh, Claire L. Parkinson, D.J. Cavalieri, J.F.B. Mitchell, D. Garrett, and V.F. Zakharov. Global warming and northern hemisphere sea ice extent. *Science*, 286(5446):1934–1937, 1999.

[3] M. Bender, T. Sowers, and E. Brook. Gases in ice cores. *Proceedings of the National Academy of Sciences*, 94(16):8343–8349, 1997.

[4] J.R. Petit, L. Mourner, J. Jouzel, Y.S. Korotkevich, V.I. Kotlyakov, and C. Lorius. Palaeoclimatological and chronological implications of the vostok core dust record. *Nature*, 343(6253):56, 1990.

[5] B. Delmonte, J. Petit, and V. Maggi. Glacial to holocene implications of the new 27000-year dust record from the epica dome c (east antarctica) ice core. *Climate Dynamics*, 18(8):647–660, 2002.

[6] U. Ruth, D. Wagenbach, J.P. Steffensen, and M. Bigler. Continuous record of microparticle concentration and size distribution in the central greenland ngrip ice core during the last glacial period. *Journal of Geophysical Research: Atmospheres*, 108(D3), 2003.

[7] F. Lambert, B. Delmonte, J.R. Petit, M. Bigler, P.R. Kaufmann, M.A. Hutterli, T.F. Stocker, U. Ruth, J.P. Steffensen, and V. Maggi. Dust-climate couplings over the past 800,000 years from the epica dome c ice core. *Nature*, 452(7187):616, 2008.

[8] E. Hood, T.J. Battin, J. Fellman, S. O'neel, and R.G.M. Spencer. Storage and release of organic carbon from glaciers and ice sheets. *Nature geoscience*, 8(2):91, 2015.

[9] V. Miteva, K. Rinehold, T. Sowers, A. Sebastian, and J. Brenchley. Abundance, viability and diversity of the indigenous microbial populations at different depths of the neem greenland ice core. *Polar Research*, 34(1):25057, 2015.

[10] A.W. Rempel, E.D. Waddington, J.S. Wettlaufer, and M.G. Worster. Possible displacement of the climate signal in ancient ice by premelting and anomalous diffusion. *Nature*, 411(6837):568, 2001.

[11] NEEM community members. Eemian interglacial reconstructed from a greenland folded ice core. *Nature*, 493(7433):489, 2013.

[12] J.M.H. Schollick, R.W. Style, A. Curran, J.S. Wettlaufer, E.R. Dufresne, P.B. Warren, K.P. Velikov, R.P.A. Dullens, and D.G.A.L. Aarts. Segregated ice growth in a suspension of colloidal particles. *The Journal of Physical Chemistry B*, 120(16):3941–3949, 2016.

[13] S.S.L. Peppin and R.W. Style. The physics of frost heave and ice-lens growth. *Vadose Zone Journal*, 12(1), 2013.

[14] DH Everett. The thermodynamics of frost damage to porous solids. *Transactions of the Faraday society*, 57:1541–1551, 1961.

[15] S.M. Miller, X. Xiao, and K.T. Faber. Freeze-cast alumina pore networks: Effects of freezing conditions and dispersion medium. *Journal of the European Ceramic Society*, 35(13):3595–3605, 2015.

[16] S. Deville. Freeze-casting of porous ceramics: a review of current achievements and issues. *Advanced Engineering Materials*, 10(3):155–169, 2008.

[17] J.O.M. Karlsson and M. Toner. Long-term storage of tissues by cryopreservation: critical issues. *Biomaterials*, 17(3):243–256, 1996.

[18] K.L. Scott, J. Lecak, and J.P. Acker. Biopreservation of red blood cells: past, present, and future. *Transfusion medicine reviews*, 19(2):127–142, 2005.

[19] D.E. Pegg. Long-term preservation of cells and tissues: a review. *Journal of clinical pathology*, 29(4):271, 1976.

[20] A.F. Davidson, C. Glasscock, D.R. McClanahan, J.D. Benson, and A.Z. Higgins. Toxicity minimized cryoprotectant addition and removal procedures for adherent endothelial cells. *PloS one*, 10(11):e0142828, 2015.

[21] J.G. Dash, H. Fu, and J.S. Wettlaufer. The premelting of ice and its environmental consequences. *Reports on Progress in Physics*, 58(1):115, 1995.

[22] T. Graham. X. liquid diffusion applied to analysis. *Philosophical transactions of the Royal Society of London*, 151:183–224, 1861.

[23] M.D. Haw. Colloidal suspensions, brownian motion, molecular reality: a short history. *Journal of physics: condensed matter*, 14(33):7769, 2002.

[24] R. Dullens. *Structure and dynamics of colloidal hard spheres in real-space*. PhD thesis, Utrecht University, 2005.

[25] D.G.A.L. Aarts, M. Schmidt, and H.N.W. Lekkerkerker. Direct visual observation of thermal capillary waves. *Science*, 304(5672):847–850, 2004.

[26] M.S. Elliot and W.C.K. Poon. Conventional optical microscopy of colloidal suspensions. *Advances in Colloid and Interface Science*, 92(1-3):133–194, 2001.

[27] J.C. Crocker and D.G. Grier. Methods of digital video microscopy for colloidal studies. *Journal of colloid and interface science*, 179(1):298–310, 1996.

[28] M.A. Azouni, W. Kalita, and M. Yemmou. On the particle behaviour in front of advancing liquid-ice interface. *Journal of crystal growth*, 99(1-4):201–205, 1990.

[29] G. Lipp, C. Körber, and G. Rau. Critical growth rates of advancing ice-water interfaces for particle encapsulation. *Journal of crystal growth*, 99(1-4):206–210, 1990.

[30] C. Körber, G. Rau, M.D. Cosman, and E.G. Cravalho. Interaction of particles and a moving ice-liquid interface. *Journal of Crystal Growth*, 72(3):649–662, 1985.

[31] V. Prasad, D. Semwogerere, and E.R. Weeks. Confocal microscopy of colloids. *Journal of Physics: Condensed Matter*, 19(11):113102, 2007.

[32] R. Piazza, T. Bellini, and V. Degiorgio. Equilibrium sedimentation profiles of screened charged colloids: A test of the hard-sphere equation of state. *Physical review letters*, 71(25):4267, 1993.

[33] A.L. Thorneywork, J.L. Abbott, D.G.A.L. Aarts, and R.P.A. Dullens. Two-dimensional melting of colloidal hard spheres. *Physical review letters*, 118(15):158001, 2017.

[34] Y. Wu, Y. Li, L. Qin, F. Yang, and D. Wu. Monodispersed or narrow-dispersed melamine–formaldehyde resin polymer colloidal spheres: preparation, size-control, modification, bioconjugation and particle formation mechanism. *Journal of materials chemistry B*, 1(2):204–212, 2013.

[35] B. Peng, E. van der Wee, A. Imhof, and A. van Blaaderen. Synthesis of monodisperse, highly cross-linked, fluorescent pmma particles by dispersion polymerization. *Langmuir*, 28(17):6776–6785, 2012.

[36] W. Stöber, A. Fink, and E. Bohn. Controlled growth of monodisperse silica spheres in the micron size range. *Journal of colloid and interface science*, 26(1):62–69, 1968.

[37] T. Sugimoto, M.M. Khan, and A. Muramatsu. Preparation of monodisperse peanut-type α-fe2o3 particles from condensed ferric hydroxide gel. *Colloids and Surfaces A: Physicochemical and Engineering Aspects*, 70(2):167–169, 1993.

[38] R.P.A. Dullens, E.M. Claesson, and W.K. Kegel. Preparation and properties of cross-linked fluorescent poly (methyl methacrylate) latex colloids. *Langmuir*, 20(3):658–664, 2004.

[39] H. Löwen. Colloidal dispersions in external fields: recent developments. *Journal of Physics: Condensed Matter*, 20(40):404201, 2008.

[40] S.C. Glotzer and M.J. Solomon. Anisotropy of building blocks and their assembly into complex structures. *Nature materials*, 6(8):557, 2007.

[41] M. Matsumoto, S. Saito, and I. Ohmine. Molecular dynamics simulation of the ice nucleation and growth process leading to water freezing. *Nature*, 416(6879):409, 2002.

[42] C.A. Angell. Supercooled water. *Annual Review of Physical Chemistry*, 34(1):593–630, 1983.

[43] C.A. Stan, G.F. Schneider, S.S. Shevkoplyas, M. Hashimoto, M. Ibanescu, B.J. Wiley, and G.M. Whitesides. A microfluidic apparatus for the study of ice nucleation in supercooled water drops. *Lab on a Chip*, 9(16):2293–2305, 2009.

[44] A.A. Shibkov, Y.I. Golovin, M.A. Zheltov, A.A. Korolev, and A.A. Leonov. Morphology diagram of nonequilibrium patterns of ice crystals growing in supercooled water. *Physica A: Statistical Mechanics and its Applications*, 319:65–79, 2003.

[45] N.J. Balmforth and J. Wettlaufer. 2006 program of studies: ice. Technical report, Woods Hole Oceanographic Institution, 2007.

[46] A.W. Rempel, J.S. Wettlaufer, and M.G. Worster. Interfacial premelting and the thermomolecular force: thermodynamic buoyancy. *Physical review letters*, 87(8):088501, 2001.

[47] S. Engemann, H. Reichert, H. Dosch, J. Bilgram, V. Honkimäki, and A Snigirev. Interfacial melting of ice in contact with sio 2. *Physical review letters*, 92(20):205701, 2004.

[48] S. Schöder, H. Reichert, H. Schröder, M. Mezger, J.S. Okasinski, V. Honkimäki, J. Bilgram, and H. Dosch. Radiation-induced premelting of ice at silica interfaces. *Physical review letters*, 103(9):095502, 2009.

[49] E.S. Thomson, J.S. Wettlaufer, and L.A. Wilen. A direct optical method for the study of grain boundary melting. *Review of Scientific Instruments*, 80(10):103903, 2009.

[50] J.G. Dash, A.W. Rempel, and J.S. Wettlaufer. The physics of premelted ice and its geophysical consequences. *Reviews of modern physics*, 78(3):695, 2006.

[51] J.M.H Schollick. Single particle engulfment and regelation. In *Real space study of pattern formation in freezing colloidal suspensions*. The University of Oxford, 2015.

[52] L. Benatov and J.S. Wettlaufer. Abrupt grain boundary melting in ice. *Physical Review E*, 70(6):061606, 2004.

[53] J.S. Wettlaufer and M.G. Worster. Premelting dynamics. *Annu. Rev. Fluid Mech.*, 38:427–452, 2006.

[54] J.S. Wettlaufer, M.G. Worster, L.A. Wilen, and J.G. Dash. A theory of premelting dynamics for all power law forces. *Physical review letters*, 76(19):3602, 1996.

[55] N. Balmforth, J.S. Wettlaufer, and M.G. Worster. 2006 program of study : Ice, technical report, 2007.

[56] P. Atkins, J. De Paula, and J. Keeler. *Atkins' physical chemistry*. Oxford university press, 2010.

[57] H. Hansen-Goos and J.S. Wettlaufer. Theory of ice premelting in porous media. *Physical Review E*, 81(3):031604, 2010.

[58] J.S. Wettlaufer. Impurity effects in the premelting of ice. *Physical Review Letters*, 82(12):2516, 1999.

[59] Y.M. Youssef, R.J. Dashwood, and P.D. Lee. Effect of clustering on particle pushing and solidification behaviour in tib2 reinforced aluminium pmmcs. *Composites Part A: Applied Science and Manufacturing*, 36(6):747–763, 2005.

[60] A.W. Rempel and M.G. Worster. The interaction between a particle and an advancing solidification front. *Journal of Crystal Growth*, 205(3):427–440, 1999.

[61] D.R. Uhlmann, B. Chalmers, and K.A. Jackson. Interaction between particles and a solid-liquid interface. *Journal of Applied Physics*, 35(10):2986–2993, 1964.

[62] G.F. Bolling and J. Cisse. A theory for the interaction of particles with a solidifying front. *Journal of Crystal Growth*, 10(1):56–66, 1971.

[63] S.N. Omenyi and A.W. Neumann. Thermodynamic aspects of particle engulfment by solidifying melts. *Journal of Applied Physics*, 47(9):3956–3962, 1976.

[64] D. Shangguan, S. Ahuja, and D.M. Stefanescu. An analytical model for the interaction between an insoluble particle and an advancing solid/liquid interface. *Metallurgical Transactions A*, 23(2):669–680, 1992.

[65] A.A. Chernov, D.E. Temkin, and A.M. MelNikova. Theory of the capture of solid inclusions during the growth of crystals from the melt. *Sov. Phys. Crystallogr*, 21(4):369–373, 1976.

[66] A.A. Chernov, D.E. Temkin, and A.M. Melnikova. Concerning influence of thermal-conductivity of a macroparticle on its capture by a crystal growing from a melt. *Kristallografiya*, 22(6):1152–1156, 1977.

[67] J. Pötschke and V. Rogge. On the behaviour of foreign particles at an advancing solid-liquid interface. *Journal of Crystal Growth*, 94(3):726–738, 1989.

[68] S. Sen, B.K. Dhindaw, D.M. Stefanescu, A. Catalina, and P.A. Curreri. Melt convection effects on the critical velocity of particle engulfment. *Journal of crystal growth*, 173(3-4):574–584, 1997.

[69] S.S.L. Peppin, H.E. Huppert, and M.G. Worster. Steady-state solidification of aqueous ammonium chloride. *Journal of Fluid Mechanics*, 599:465–476, 2008.

[70] Y. Liu. Colloidal tpm particles for three-dimensional confocal microscopy. In *Colloidal particles for confocal microscopy and optical tweezing*. The University of Oxford, 2017.

[71] Y. Liu, K.V. Edmond, A. Curran, C. Bryant, B. Peng, D.G.A.L. Aarts, S. Sacanna, and R.P.A. Dullens. Core–shell particles for simultaneous 3d imaging and optical tweezing in dense colloidal materials. *Advanced Materials*, 28(36):8001–8006, 2016.

[72] T.J. Barnes and C.A. Prestidge. Peo- ppo- peo block copolymers at the emulsion droplet-water interface. *Langmuir*, 16(9):4116–4121, 2000.

[73] M.D. Rodrigo and J.M. Marc. *SU-8 Photolithography and Its Impact on Microfluidics*, volume 2, chapter 8. CRC Press, 2011.

[74] MicroChem Corp. *SU-8 2000 Permanent Epoxy Negative Photoresist Processing Guidelines for: SU-8 2000.5, SU-8 2002, SU-8 2005, SU-8 2007, SU-8 2010 and SU-8 2015.* Technical report.

[75] W.J. Kang, E. Rabe, S. Kopetz, and A. Neyer. Novel exposure methods based on reflection and refraction effects in the field of su-8 lithography. *Journal of Micromechanics and Microengineering*, 16(4):821, 2006.

[76] A. Rice and R. Fischer. Calibration of optical tweezers. *Materials Science Institute*, 1997.

[77] J.S. Langer. Instabilities and pattern formation in crystal growth. *Reviews of Modern Physics*, 52(1):1, 1980.

[78] M. Uemura and H. Ishiguro. Freezing behavior of adherent neuron-like cells and morphological change and viability of post-thaw cells. *Cryobiology*, 70(2):122–135, 2015.

[79] B.R. Pamplin. *Crystal growth*, volume 16. Pergamon, 1980.

[80] S.H. Davis. *Theory of solidification*. Cambridge University Press, 2001.

[81] W.W. Mullins and R.F. Sekerka. Morphological stability of a particle growing by diffusion or heat flow. *Journal of applied physics*, 34(2):323–329, 1963.

[82] L. Qian and H. Zhang. Controlled freezing and freeze drying: a versatile route for porous and micro-/nano-structured materials. *Journal of Chemical Technology & Biotechnology*, 86(2):172–184, 2011.

[83] J.A. Sekhar and R. Trivedi. Solidification microstructure evolution in the presence of inert particles. *Materials Science and Engineering: A*, 147(1):9–21, 1991.

[84] W.W. Mullins and R.F. Sekerka. Stability of a planar interface during solidification of a dilute binary alloy. In *Dynamics of Curved Fronts*, pages 345–352. Elsevier, 1988.

[85] H. Zhang, I. Hussain, M. Brust, M.F. Butler, S.P. Rannard, and A.I. Cooper. Aligned two- and three-dimensional structures by directional freezing of polymers and nanoparticles. *Nature Materials*, 4(10):787, 2005.

[86] M.F. Butler. Instability formation and directional dendritic growth of ice studied by optical interferometry. *Crystal Growth & Design*, 1(3):213–223, 2001.

[87] S. Deville, E. Saiz, and A.P. Tomsia. Ice-templated porous alumina structures. *Acta Materialia*, 55(6):1965–1974, 2007.

[88] W.A. Tiller, K.A. Jackson, J.W. Rutter, and B. Chalmers. The redistribution of solute atoms during the solidification of metals. *Acta metallurgica*, 1(4):428–437, 1953.

[89] M.F. Butler. Freeze concentration of solutes at the ice/solution interface studied by optical interferometry. *Crystal growth & design*, 2(6):541–548, 2002.

[90] A.W. Rempel, J.S. Wettlaufer, and M.G. Worster. Premelting dynamics in a continuum model of frost heave. *Journal of Fluid Mechanics*, 498:227–244, 2004.

[91] S.S.L. Peppin, M.G. Worster, and J.S. Wettlaufer. Morphological instability in freezing colloidal suspensions. In *Proceedings of the Royal Society of London A: Mathematical, Physical and Engineering Sciences*, volume 463, pages 723–733. The Royal Society, 2007.

[92] J. You, L. Wang, Z. Wang, J. Li, J. Wang, X. Lin, and W. Huang. Interfacial undercooling in solidification of colloidal suspensions: analyses with quantitative measurements. *Scientific reports*, 6:28434, 2016.

[93] W. Kurz and D.J. Fisher. Dendrite growth at the limit of stability: tip radius and spacing. *Acta Metallurgica*, 29(1):11–20, 1981.

[94] D.J. Fisher and W. Kurz. A theory of branching limited growth of irregular eutectics. *Acta Metallurgica*, 28(6):777–794, 1980.

[95] D.M. Zhu, O.E. Vilches, J.G. Dash, B. Sing, and J.S. Wettlaufer. Frost heave in argon. *Physical Review Letters*, 85(23):4908, 2000.

[96] S.C. Hardy. A grain boundary groove measurement of the surface tension between ice and water. *Philosophical Magazine*, 35(2):471–484, 1977.

[97] M.F Butler. Growth of solutal ice dendrites studied by optical interferometry. *Crystal growth & design*, 2(1):59–66, 2002.

[98] N.O. Shanti, K. Araki, and J.W. Halloran. Particle redistribution during dendritic solidification of particle suspensions. *Journal of the American Ceramic Society*, 89(8):2444–2447, 2006.

[99] C. Clarke. *The science of ice cream*. Royal Society of Chemistry, 2015.

[100] C. Körber. Phenomena at the advancing ice–liquid interface: solutes, particles and biological cells. *Quarterly reviews of biophysics*, 21(2):229–298, 1988.

[101] S.S.L. Peppin, J.S. Wettlaufer, and M.G. Worster. Experimental verification of morphological instability in freezing aqueous colloidal suspensions. *Physical review letters*, 100(23):238301, 2008.

[102] D.M. Stefanescu, F.R. Juretzko, A. Catalina, B.K. Dhindaw, S. Sen, and P.A. Curreri. Particle engulfment and pushing by solidifying interfaces: Part ii. microgravity experiments and theoretical analysis. *Metallurgical and Materials Transactions A*, 29(6):1697–1706, 1998.

[103] D. Dedovets and S. Deville. Multiphase imaging of freezing particle suspensions by confocal microscopy. *arXiv preprint arXiv:1712.07707*, 2017.

[104] J.W. Kim, K. Tazumi, R. Okaji, and M. Ohshima. Honeycomb monolith-structured silica with highly ordered, three-dimensionally interconnected macroporous walls. *Chemistry of Materials*, 21(15):3476–3478, 2009.

[105] C. Allain and L. Limat. Regular patterns of cracks formed by directional drying of a collodial suspension. *Physical review letters*, 74(15):2981, 1995.

[106] D.M. Smith, G.W. Scherer, and J.M. Anderson. Shrinkage during drying of silica gel. *Journal of Non-Crystalline Solids*, 188(3):191–206, 1995.

[107] M.D. Haw. Jamming, two-fluid behavior, and self-filtration in concentrated particulate suspensions. *Physical review letters*, 92(18):185506, 2004.

[108] F. Bouville, E. Maire, and S. Deville. Self-assembly of faceted particles triggered by a moving ice front. *Langmuir*, 30(29):8656–8663, 2014.

[109] M. Spannuth, S.G.J. Mochrie, S.S.L. Peppin, and J.S. Wettlaufer. Particle-scale structure in frozen colloidal suspensions from small-angle x-ray scattering. *Physical Review E*, 83(2):021402, 2011.

[110] S.A. Barr and E. Luijten. Structural properties of materials created through freeze casting. *Acta materialia*, 58(2):709–715, 2010.

[111] S. Deville, E. Maire, G. Bernard-Granger, A. Lasalle, A. Bogner, C. Gauthier, J. Leloup, and C. Guizard. Metastable and unstable cellular solidification of colloidal suspensions. *Nature materials*, 8(12):966, 2009.

[112] A.A. Chernov. Capture of inclusions in crystal growth. *Current Topics in Materials Science.*, 2:3–77, 1977.

[113] M.G. Worster, J.S. Wettlaufer, W. Shyy, and R. Naranyanan. The fluid mechanics of premelted liquid films. *Fluid dynamics at interfaces*, pages 339–351, 1999.

[114] J.J. Guo and J.A. Lewis. Aggregation effects on the compressive flow properties and drying behavior of colloidal silica suspensions. *Journal of the American Ceramic Society*, 82(9):2345–2358, 1999.

[115] N.F. Carnahan and K.E. Starling. Equation of state for nonattracting rigid spheres. *The Journal of Chemical Physics*, 51(2):635–636, 1969.

[116] T. Pradell, R. Fernandes, G. Molina, A.D. Smith, J. Molera, A. Climent-Font, and M.S. Tite. Technology of production of syrian lustre (11th to 13th century). *Journal of the European Ceramic Society*, 38(7):2716–2727, 2018.

[117] A. L. Thorneywork, R. Roth, D.G.A.L. Aarts, and R.P.A. Dullens. Communication: Radial distribution functions in a two-dimensional binary colloidal hard sphere system, 2014.

[118] J. P. Hansen and I. R. Mcdonald. *Theory of Simple Liquids*. Academic Press, 3 edition, 2006.

[119] H. Hertz. Journal fur die rein und angewandte mathematik (crelle's journal). *Ueber die Beruhrung fester elastischer Korper*, 92:156–171, 1882.

[120] R.P.A. Dullens. Kinetic broadening of the crystal-fluid interface of colloidal hard spheres. In *Structure and dynamics of colloidal hard spheres in real-space*. Universiteit Utrecht, 2005.

[121] R.P.A. Dullens, D.G.A.L. Aarts, and W.K. Kegel. Dynamic broadening of the crystal-fluid interface of colloidal hard spheres. *Physical review letters*, 97(22):228301, 2006.

[122] L.G. Thompson and E. Mosley-Thompson. Microparticle concentration variations linked with climatic change: evidence from polar ice cores. *Science*, 212(4496):812–815, 1981.

[123] G.A. Zielinski and G.R. Mershon. Paleoenvironmental implications of the insoluble microparticle record in the gisp2 (greenland) ice core during the rapidly changing climate of the pleistocene–holocene transition. *Geological Society of America Bulletin*, 109(5):547–559, 1997.

[124] D. Kuroiwa. A study of ice sintering. *Tellus*, 13(2):252–259, 1961.

[125] K.M. Cuffey, H. Conway, A.M. Gades, B. Hallet, R. Lorrain, J.P. Severinghaus, E.J. Steig, B. Vaughn, and J.W.C. White. Entrainment at cold glacier beds. *Geology*, 28(4):351–354, 2000.

[126] L.A. Wilen and J.G. Dash. Frost heave dynamics at a single crystal interface. *Physical Review Letters*, 74(25):5076, 1995.

[127] M.J.M. Römkens and R.D. Miller. Migration of mineral particles in ice with a temperature gradient. *Journal of Colloid and Interface Science*, 42(1):103–111, 1973.

[128] J.N. Israelachvili and H. Wennerstroem. Entropic forces between amphiphilic surfaces in liquids. *The Journal of Physical Chemistry*, 96(2):520–531, 1992.

[129] G. Lipp and C. Körber. On the engulfment of spherical particles by a moving ice-liquid interface. *Journal of crystal growth*, 130(3-4):475–489, 1993.

[130] L.A. Wilen, J.S. Wettlaufer, M. Elbaum, and M. Schick. Dispersion-force effects in interfacial premelting of ice. *Physical Review B*, 52(16):12426, 1995.

[131] S.S.L. Peppin, M.J. Spannuth, and J.S. Wettlaufer. Onsager reciprocity in premelting solids. *Journal of Statistical Physics*, 134(4):701–708, 2009.

[132] B. Saint-Michel, M. Georgelin, S. Deville, and A. Pocheau. Interaction of multiple particles with a solidification front: from compacted particle layer to particle trapping. *Langmuir*, 33(23):5617–5627, 2017.

[133] S. Deville, E. Maire, A. Lasalle, A. Bogner, C. Gauthier, J. Leloup, and C. Guizard. In situ x-ray radiography and tomography observations of the solidification of aqueous alumina particle suspensionspart i: Initial instants. *Journal of the American Ceramic Society*, 92(11):2489–2496, 2009.

[134] B. Delattre, H. Bai, R.O. Ritchie, J. De Coninck, and A.P. Tomsia. Unidirectional freezing of ceramic suspensions: In situ x-ray investigation of the effects of additives. *ACS applied materials & interfaces*, 6(1):159–166, 2013.

[135] S. Deville, J. Adrien, E. Maire, M. Scheel, and M. Di Michiel. Time-lapse, three-dimensional in situ imaging of ice crystal growth in a colloidal silica suspension. *Acta Materialia*, 61(6):2077–2086, 2013.

[136] G. Sazaki, S. Zepeda, S. Nakatsubo, E. Yokoyama, and Y. Furukawa. Elementary steps at the surface of ice crystals visualized by advanced optical microscopy. *Proceedings of the National Academy of Sciences*, 107(46):19702–19707, 2010.

[137] L.D. Landau and E.M. Lifshitz. *Fluid Mechanics 2nd Edition*. Pergamon Press, 1987.

[138] C. Zhang and P. Carloni. Salt effects on water/hydrophobic liquid interfaces: a molecular dynamics study. *Journal of Physics: Condensed Matter*, 24(12):124109, 2012.

[139] K. Nagashima and Y. Furukawa. Nonequilibrium effect of anisotropic interface kinetics on the directional growth of ice crystals. *Journal of Crystal growth*, 171(3):577–585, 1997.

[140] K. Nagashima and Y. Furukawa. Solute distribution in front of an ice/water interface during directional growth of ice crystals and its relationship to interfacial patterns. *The Journal of Physical Chemistry B*, 101(32):6174–6176, 1997.

[141] R. Chen, C.A. Wang, Y. Huang, L. Ma, and W. Lin. Ceramics with special porous structures fabricated by freeze-gelcasting: Using tert-butyl alcohol as a template. *Journal of the American Ceramic Society*, 90(11):3478–3484, 2007.

List of publications

To date the following publications based upon work in this thesis are in preparation:

Siyu Chen, Jenny Kuo, Roel P. A. Dullens and Dirk G. A. L. Aarts, *Morphological instability of colloidal suspension* (chapter 3).

Siyu Chen, Jenny Kuo, Roel P. A. Dullens and Dirk G. A. L. Aarts, *Single particle scale structure properties in frozen colloidal suspensions* (chapter 4).

Siyu Chen, Julia M. H. Schollick, Roel P. A. Dullens and Dirk G. A. L. Aarts, *Regelating particles viewed in real space* (chapter 5).

Siyu Chen, Julia M. H. Schollick, Robert W. Style, Roel P. A. Dullens and Dirk G. A. L. Aarts, *The ice-water meniscus in 3D* (chapter 6).

Acknowledgments

First of all, I would like to thank Dirk and Roel. Dirk, thank you for all the guidance and support, for your sense of humour, and for the nespresso machine. Roel, thank you for your ideas, comments and suggestions, regarding this thesis and the synthesis projects, and for the summer barbecues. I feel extremely fortunate to be part of the colloid group, my time in the group was extremely fun and memorable.

Following on, I would like to thank Rob and Julia. Thank you both for helping me getting on with the project, during my transition period. Thank Bo for all the helps, discussions and advices regarding the synthesis projects. I must also thank my excellent Part II students, Jenny and Caitlin, as my thesis would not have been complete without you. I also need to thank all the members in the group. In particular, Louis, it has been a pleasure to share the office, and countless bottles of wine with you. Josh, thank you for all the helps from my day one, and your legacy of Pub Friday and Group Lunch. Joe, thank you for all the proofreading and enthusiasm in beers. Adam, thank you for all the scientific and non-scientific chats we have had, weekdays and weekends. I also need to thank Ivo and Taiki for advices and beers. Chinese Scholarship Council and St Cross College are thanked for providing financial aids. Special thanks also goes to Jack, Piotr, Sarah and other Brown's group members for being good lunch companions.

I also want to address a huge thank you to St Cross College. I need to thanks the senior staffs, including but not limited to, Mrs. Carole Souter, Miss Jocelyn Larsen, Mr. Kenny Cox, Miss Lara Summerhill and Ms. Sheila Allcock for all your trusts and lovely conversations. I also need to thank Thomas, John, Peter, Irini, Jelena and the other Wellington Square people, Alex and the rest of the 2017 SRC team and many others for the wonderful college life.

Last but not least, I want to say a massive thank you to my family, for their unfailing support, emotionally and financially, in my life choices. I know I will always owe a great deal to them. THANK YOU!!